



**This electronic thesis or dissertation has been
downloaded from Explore Bristol Research,
<http://research-information.bristol.ac.uk>**

Author:
Courtier, Mark

Title:
Guided Wave Structural Health Monitoring of Complex Aerospace Components

General rights

Access to the thesis is subject to the Creative Commons Attribution - NonCommercial-No Derivatives 4.0 International Public License. A copy of this may be found at <https://creativecommons.org/licenses/by-nc-nd/4.0/legalcode>. This license sets out your rights and the restrictions that apply to your access to the thesis so it is important you read this before proceeding.

Take down policy

Some pages of this thesis may have been removed for copyright restrictions prior to having it been deposited in Explore Bristol Research. However, if you have discovered material within the thesis that you consider to be unlawful e.g. breaches of copyright (either yours or that of a third party) or any other law, including but not limited to those relating to patent, trademark, confidentiality, data protection, obscenity, defamation, libel, then please contact collections-metadata@bristol.ac.uk and include the following information in your message:

- Your contact details
- Bibliographic details for the item, including a URL
- An outline nature of the complaint

Your claim will be investigated and, where appropriate, the item in question will be removed from public view as soon as possible.



Guided Wave Structural Health Monitoring of Complex Aerospace Components

Mark Raymond Courtier

A dissertation submitted to the University of Bristol in accordance with the requirements for award of the degree of Doctor of Engineering in the Faculty of Engineering.

October 2018

Word Count: 40 097

Abstract

The main focus in this work has been to improve the understanding of how the monitored structure affects the performance of guided wave acoustic emission systems. This was to address poor performance of an Airbus acoustic emission system when it was used to monitor a complex section of an aircraft wing during a fatigue test.

To do this the whole acoustic emission system was modelled. The focus of the modelling effort was in two parts. The first was to define a suitable source for a fatigue crack in aluminium to use as an input to the model. This was found from the literature and compared with results from Airbus tests. The second part was to develop an approach to model the guided wave propagation in large structures. This led to the development of empirical transmission models that could be created with reduced effort compared to other transmission modelling techniques. These transmission models were deliberately conservative in their prediction of amplitude to ensure they could safely be used to determine which transducers would detect acoustic emission events at different locations. The whole system model could then be used to determine acoustic emission system performance for different scenarios. By varying the structure in the model its influence on system outputs such as detection and location of acoustic emission events could be demonstrated. Therefore a tool has been created to aid the future development and deployment of acoustic emission systems.

There are two other major achievements in this thesis. The first is the development of an efficient method to collect guided wave data over large areas using a design of experiments based technique. The second is an analysis of results from a long term active guided wave structural health monitoring experiment. Understanding this behaviour is necessary for the further deployment of these systems.

Acknowledgements

My most important thanks go to my academic and industrial supervisors Anthony Croxford and Kathryn Atherton. Without their guidance, encouragement and help I would not have been able to do this. I would like to thank Christophe Paget for his role in setting up this Engineering Doctorate, for his help whilst I was at Airbus in Filton and for our many useful discussions. I would like to thank everyone involved with the EPSRC Centre for Doctoral Training in Quantitative NDE, especially Chris Scruby and Keith Newton. Through this I have met many other Engineering Doctorate students, a number of whom have become good friends.

During this process I have worked alongside many colleagues in the Ultrasonics and NDT group at the University of Bristol and the Structural Health Monitoring group at Airbus Ltd. I would like to thank them all for their regular help and enjoyable company. I would particularly like to thank Agata Lovrecich for finding the key documents that enabled much of chapter 2.

I would also like to thank the unique University of Bristol Pantomime Society for providing necessary diversions. And finally I would like to thank my wonderful friends and family whom I am very lucky to have. They have helped me through the highs and lows of this experience and I will always appreciate them.

Mark Courtier was enrolled in the Engineering Doctorate Programme in NDE at the University of Bristol. He was funded by the Engineering and Physical Sciences Research Council (EPSRC) through the Centre for Doctoral Training in Quantitative NDE and by Airbus Operations Ltd.

Author's declaration

I declare that the work in this dissertation was carried out in accordance with the requirements of the University's Regulations and Code of Practice for Research Degree Programmes and that it has not been submitted for any other academic award. Except where indicated by specific reference in the text, the work is the candidate's own work. Work done in collaboration with, or with the assistance of, others, is indicated as such. Any views expressed in the dissertation are those of the author.

SIGNED: DATE:

Contents

1	Introduction	1
1.1	Mitigating damage in aircraft structures	1
1.2	The potential for structural health monitoring in aerospace ap- plications	2
1.3	Active and passive guided wave structural health monitoring . .	4
1.3.1	Active guided wave structural health monitoring	6
1.3.2	Acoustic emission	6
1.4	Challenges in applying guided wave structural health monitoring	7
1.4.1	Dispersion	7
1.4.2	Environmental and operating conditions	7
1.5	Operation of an acoustic emission system	8
1.5.1	Guided wave transducers	9
1.5.2	Determining arrival times	10
1.5.3	Locating acoustic emission events	11
1.5.4	Classifying acoustic emission events	12
1.6	Acoustic emission testing at Airbus	12
1.6.1	BALRUE data processing	13
1.6.2	Limitations of current testing	15
1.7	Aims and outline of this thesis	18
1.8	Novel contributions of this thesis	19
2	Acoustic Emission Sources	21
2.1	Introduction	21
2.2	The linear time-shift invariant systems modelling approach . . .	21
2.3	Literature on acoustic emission sources in aluminium	23
2.3.1	Estimating the amplitude of acoustic emission events from a fatigue crack in aluminium	25
2.4	Obtaining acoustic emission amplitudes from a structural test . .	31
2.4.1	Matching acoustic emission and pencil lead break events .	32
2.4.2	Comments on the dataset	43

2.4.3	Obtaining an estimate of amplitude from the Airbus dataset	48
2.5	Conclusions	52
3	Guided Wave Propagation Across Features	54
3.1	Modelling of guided wave propagation across features in the literature	55
3.2	Experimental measurement of transmission across features typical of aircraft structure	57
3.2.1	Transmission across a box section	58
3.2.2	Transmission across a row of holes and a bolted L-section	62
3.3	Selection of empirical models	71
3.4	Experimental measurement of time delay	73
3.5	Conclusions	75
4	Validation of Empirical Transmission Models	76
4.1	The model to be validated	76
4.2	Validation on a plate with 2 bonded box sections	77
4.3	Validation on a plate with 2 bolted L-sections	84
4.4	Validation on a section of A320 wing skin	90
4.5	Conclusions	94
5	Example Uses of Modelling	96
5.1	Modelling details	96
5.2	Predicting the triggered transducers	98
5.3	The influence of number of transducers on location accuracy	101
5.4	Comparing location algorithm performance	106
5.5	Using the A_0 mode	113
5.6	Conclusions	117
6	A Design of Experiments Based Data Collection Approach	119
6.1	Background information	120
6.2	Algorithm operation	121
6.2.1	Algorithm implementation	122
6.3	Example on simulated data	124
6.3.1	Convergence of model difference	126
6.3.2	Threshold as a stop criterion	128
6.4	Example on experimental data	128
6.5	Conclusions	131

7	The Long Term Performance of Guided Wave Systems	133
7.1	Baseline subtraction and temperature compensation techniques .	134
7.2	Experimental description	136
7.3	Changes in signal parameters	138
7.4	Performance of baseline subtraction techniques	144
7.4.1	Defined baseline set	147
7.4.2	Continuous baseline growth algorithm	148
7.4.3	Discussion on baseline subtraction performance	148
7.5	Conclusions	148
8	Conclusions	151
8.1	Understanding the effect of the structure on acoustic emission system performance	151
8.2	Other key achievements	155
8.2.1	A design of experiments data collection approach	155
8.2.2	Long term system performance	156
8.3	Recommendations for Airbus	157
8.4	Future work	159
	Appendix A Acoustic Emission Source Calculations from the A340- 600 EF2 Test	161
	Appendix B Publications List	164
	Bibliography	165
	Acronyms	173

List of Tables

1.1	SHM technologies.	3
2.1	The maximum amplitude of the first arrival for each mode from a fatigue crack in an aluminium plate.	26
2.2	The values of $D^{250\text{ kHz}}$ for different transducers.	27
2.3	The values of displacement at the transducer position, $M_0^{250\text{ kHz}}$, calculated for different transducer types.	27
2.4	The values of displacement measured 0.3 m from the source, $S^{250\text{ kHz}}$, calculated for different transducer types.	28
2.5	The surface displacement of the signals at 0.3 m from the AE source, $M_{\text{AE}}^{250\text{ kHz}}$, calculated for different transducer types.	29
2.6	The maximum amplitude of the first arrival for each mode from a PLB on an aluminium plate.	29
2.7	The AE to PLB amplitude ratio, $M_{\text{AE}}^{250\text{ kHz}}/M_{\text{PLB}}^{250\text{ kHz}}$, for a fatigue crack in an aluminium plate calculated for different transducer types.	29
2.8	Number and percentage of AE events matched to PLBs at damage for each technique.	36
2.9	Comparison of the mean PLB groupings across the different damage locations for each matching method.	39
3.1	The wavelengths of the S_0 mode in 3 mm aluminium for the frequencies of interest.	71
4.1	The transducer positions for the structure with 2 bonded box sections.	77
4.2	Comparison of mean absolute difference and points above the model for the different transmission models and scaling techniques for the signals collected on the structure with 2 bonded box sections.	82
4.3	The transducer positions for the structure with 2 bolted L-sections.	84

4.4	Comparison of mean absolute difference and points above the model for the different transmission models and scaling techniques for the signals collected on the structure with 2 bolted L-sections.	88
4.5	Comparison of mean absolute difference and points above model for the different transmission models and scaling techniques for the signals collected on the section of A320 wing skin.	93
5.1	The positions of transducers in the modelling examples.	97
5.2	The mean and median values of location error for the 2 location algorithms on the different structures.	112
7.1	The transducer positions on the water tank measured from the bottom left corner.	136

List of Figures

1.1	The dispersion curves for a 3 mm thick aluminium plate.	5
1.2	The threshold processing applied by the BALRUE system on the signals from the first 3 triggered transducers.	14
1.3	A diagram illustrating the proposed solutions to the problems which occurred with the Airbus A380 test.	16
2.1	The filtered waveform received from a growing fatigue crack in an aluminium plate.	26
2.2	Calibrated and filtered waveforms from a PLB source.	28
2.3	The model of an AE source for a fatigue crack in a 3 mm aluminium plate for the A_0 and S_0 mode.	30
2.4	The approximate position of the area of the wing monitored with an AE system during a whole aircraft fatigue test of an A340-600.	31
2.5	An illustrative diagram of collecting PLB signals from locations near damage on the A340-600 test.	33
2.6	Group velocity dispersion curves for aluminium.	34
2.7	A diagram showing the location matching method.	35
2.8	The number of AE events matched to each damage location for each matching technique.	37
2.9	Location plot of the AE data for the A340-600 EF2 test using the Paget algorithm.	40
2.10	Location plot of the AE data for the A340-600 EF2 test using the point method with the first 3 hit transducers.	41
2.11	Location plot of the AE data for the A340-600 EF2 test using the point method with the first 4 hit transducers.	42
2.12	The cumulative rate of occurrence of AE events across the testing period for the A340-600 EF2 test.	43
2.13	The amplitude distribution for the 1st to 3rd triggered transducers for all of the AE events collected during the A340-600 EF2 test that can be matched to identified damage locations.	46

2.14	Example amplitude distributions for different damage locations in the A340-600 EF2 test.	47
2.15	Example amplitude distributions for different damage locations in the A340-600 EF2 test and the estimated distribution of events.	49
2.16	Scatter plots for the first 3 triggered transducers showing the amplitude and distribution in time of AE events for damage C05 over the whole test.	50
2.17	A scatter plot showing the number of matches and the AE to PLB ratio for each damage location.	51
3.1	A plan view of the bonded box section transmission experiment.	59
3.2	The cross section of the bonded box section.	59
3.3	Example 190 kHz collected signals from the box section transmission experiment.	61
3.4	The transmission coefficient across a bonded box section for 190 kHz.	62
3.5	The cross section of the bolted L-section.	63
3.6	A plan view of the bolted L-section transmission experiment.	64
3.7	6 repeated maximum amplitude measurements deconvolved at different frequencies for the plate prior to hole drilling and attachment of the L-section stiffener.	65
3.8	Example 100 kHz collected signals from the row of holes and the L-section experiments for different incident angles.	67
3.9	Example 200 kHz collected signals from the row of holes and the L-section experiments for different incident angles.	68
3.10	Example 300 kHz collected signals from the row of holes and the L-section experiments for different incident angles.	69
3.11	The transmission coefficient across a row of holes with a 25 mm spacing for different frequencies.	70
3.12	The transmission coefficient across a bolted L-section for different frequencies.	70
3.13	The increase in arrival time measured between the clear path signal and the signal that has crossed different features.	74
4.1	Plan view of the structure with 2 bonded box sections.	78
4.2	Comparisons between experimentally measured and modelled first arrival amplitude from an AE source received at different transducers on the structure with 2 bonded box sections.	80
4.3	Diagram showing the 2 bolted L-sections structure.	84

4.4	Comparisons between experimentally measured and modelled first arrival amplitude from an AE source received at transducer 2 on the structure with 2 bolted L-sections.	86
4.5	Comparisons between experimentally measured and modelled first arrival amplitude from an AE source received at transducer 6 on the structure with 2 bolted L-sections.	87
4.6	Picture of the section of A320 wing skin.	89
4.7	Comparisons between experimentally measured and modelled first arrival amplitude from an AE source received at transducer 1 on a section of A320 wing skin.	91
4.8	Comparisons between experimentally measured and modelled first arrival amplitude from an AE source received at transducer 2 on a section of A320 wing skin.	92
5.1	The number of transducers AE events at different positions will trigger with row of holes in between.	99
5.2	The number of transducers AE events at different positions will trigger with a bolted L-section in between.	99
5.3	The number of transducers AE events at different positions will trigger with a bonded box section in between.	100
5.4	The number of transducers AE events at different positions will trigger with a bolted L-section in between. This is the case with 6 transducers.	101
5.5	The location error for the Point Method using 3 transducers. . .	102
5.6	The location error for the Point Method using 3 transducers. The transducers have been rearranged.	104
5.7	The location error for the Point Method using 4 transducers. . .	105
5.8	The location error for the Paget algorithm on the plate with a row of holes in the centre.	108
5.9	The location error for the Point Method on the plate with a row of holes in the centre.	109
5.10	The location error for the Paget algorithm on the plate with a bolted L-section in the centre.	110
5.11	The location error for the Point Method on the plate with a bolted L-section in the centre.	111
5.12	The number of transducers AE events at different positions will trigger for different modes on a structure with Scholey's bolted L-section centrally positioned.	114
5.13	The location error for different threshold values for AE events for a a plate with Scholey's bolted L-section in the centre.	116

5.14	The number of transducers AE events at different positions will trigger on the structure with Scholey's bolted L-section centrally positioned. This is for the S_0 mode with a raised threshold. . . .	117
6.1	Flow chart showing the operation of the data collection algorithm.	122
6.2	Diagram of simulated experiment including the receiver position, source locations and L-section stiffeners.	125
6.3	The amplitude of the first S_0 arrival on the plate with 2 L-section stiffeners after the effect of beam spread has been removed. . . .	125
6.4	How the difference of model to sparse dataset and raster scan to sparse dataset changes as the algorithm progresses for a single simulation.	126
6.5	How the mean difference of model to sparse dataset and raster scan to sparse dataset changes as the algorithm progresses for 924 simulations.	127
6.6	A diagram of the collection region and receiver position on a section of A320 wing skin.	129
6.7	The amplitude of the first S_0 arrival on a section of A320 wing skin after the effect of beam spread has been removed.	129
6.8	How the difference of model to sparse dataset and raster scan to sparse dataset changes as the algorithm progresses for 100 runs on a experimental dataset.	130
7.1	An example of baseline subtraction performed with 2 signals from the same transducer pair from the water tank dataset.	135
7.2	A picture of the water tank.	137
7.3	A diagram of the experimental setup.	137
7.4	The mean and standard deviation of the first arrival time difference for all transducer pairs.	139
7.5	The change in mean and standard deviation of the maximum amplitude for all transducer pairs.	140
7.6	The mean and standard deviation of the centre frequency for all transducer pairs.	141
7.7	The mean and standard deviation of the bandwidth for all transducer pairs.	142
7.8	The mean and standard deviation maximum amplitude across all transducer pairs for different processing methods with a defined baseline set.	145

7.9	How the mean and standard deviation of different parameters change when the CBG algorithm is applied to a subset of the dataset.	146
-----	--	-----

Chapter 1

Introduction

This chapter will give an overview of how aircraft are designed to tolerate the damage that will occur to them whilst in service and discuss where Structural Health Monitoring (SHM) systems could be used to aid the inspection of aircraft. Guided Wave Structural Health Monitoring (GWSHM) systems will then be described with a focus on Acoustic Emission (AE) systems. This will include background to guided waves, the necessary considerations when implementing guided wave based systems and an explanation of the operation of AE systems. In this work the focus will be on aluminium aircraft structures however many of the considerations are more general. How AE systems are used at Airbus Ltd. will then be explained followed by an assessment of the current issues with the systems. This leads to the motivation for the work conducted in this thesis and a summary of the key achievements of this work.

1.1 Mitigating damage in aircraft structures

During the operation of aircraft it is expected that they will undergo some damage. This may be due to collisions that could be major or minor, corrosion due to environmental conditions or fatigue that occurs due to the loading the aircraft is subjected to over its life. Significant effort is invested during the design of aircraft and over multiple aircraft programmes to ensure in service aircraft can tolerate these damages in a safe and economical way [1, 2]. This is achieved by very thorough consideration of different failure modes during the design of all structurally significant components and assemblies. This is reinforced by periodic inspection of the aircraft through its life which check the structure to ensure it is performing as it is expected to and therefore the design assumptions are correct. This also informs the necessary maintenance activities and repairs to mitigate the effects any damage in the structure has on the remaining life of

the aircraft. Repairs aim to restore full life to the structure so the limit of life in an ageing aircraft is not the decrease in the performance of the structure but the increase in cost of keeping it at that level of performance [1].

Gross damage to an aircraft is detected by regular visual inspection of the outside of aircraft and through reporting of major incidents such as ground based collisions or bird strike. Detecting smaller damage is achieved through periodic inspection of the structure both by detailed visual inspection and other Non-Destructive Testing (NDT) techniques. These predominately include ultrasonic and eddy current based techniques [1, 3, 4]. The main type of damage in the structure and the damage these inspections are aiming to detect is fatigue cracks which can potentially occur at many positions in the aircraft [4]. These cracks generally initiate from changes in the geometry of the structure. This can include thickness changes, holes, fasteners and cut outs. Cracks can initiate at locations which are not easily accessible so performing these inspections can take significant amounts of time, labour and effort.

The combination of damage tolerant designs and periodic inspection have led to modern aircraft having an extremely good safety record and very high individual aircraft reliability [1]. However the aerospace market is highly competitive and this has led to constant investigations into alternative methods of doing things which may give the company implementing them a competitive advantage. SHM has the potential to be implemented alongside or in replacement of some of the periodic inspection and give certain advantages which will be discussed in the next section.

1.2 The potential for structural health monitoring in aerospace applications

SHM is the *“process of implementing a damage identification strategy for aerospace, civil or mechanical engineering infrastructure”* [5]. SHM systems typically consist of sensing equipment that is permanently attached to the structure of interest. This either constantly or at regular periods assesses if there is any damage in the structure. SHM systems often also consist of a remote processing unit which interprets the information from the sensors. There are many different candidate technologies for SHM which function over different areas and via different physical effects. Good overviews of the available technologies are presented in [6] and [7]. A list of these technologies and their respective areas of coverage are shown in 1.1. As can be seen in this list, some technologies would be better for monitoring a local area for a specific problem. A good example of this is shown in [8]. Here comparative vacuum monitoring is used to detect

SHM technology	Detectable damage type	Measurement area
Acoustic emission	Impacts, cracks, delaminations	Global
Fibre Bragg grating	Impacts, delaminations, unusual loads	Local
Active guided wave/Acousto-ultrasonic/Lamb wave	Delaminations, cracks	Global
Comparative vacuum monitoring	Cracks, corrosion, debondings	Local
Eddy current foil sensors	Cracks, corrosion	Local
Micro wave	Water ingress	Local
Environmental degradation monitoring sensors	Corrosion	Local
Chemical layers/sensors	Corrosion	Local

Table 1.1: SHM technologies [6, 7].

crack growth on a hard to access location on the wingbox of a Boeing 737. In this example a SHM technique has replaced visual and eddy current NDT inspections but more importantly has removed the need for a laborious and time consuming disassembly to perform the inspection. Other technologies aim to give a more global approach to assessing damage. This means one system can detect damage from multiple locations. This includes the guided wave based techniques; AE and active GWSHM. These will be the technologies focused on in this thesis and the majority of the effort will be focused on AE systems. Some of the work will be applicable to both technologies.

Applying SHM to aircraft structures can potentially offer the following advantages [4, 9]:

Allowing maintenance to be condition based rather than routine based.

Current maintenance schedules are based on conservative assumptions of the damage and damage growth within the structure. This means nearly all inspections will find less damage than the worst case assumptions and therefore few repairs are necessary. Conducting inspections can be costly both in removing an aircraft from service and performing the inspections which have high labour costs [3]. If a SHM system could provide more information about a structure then the period of these inspections could be reduced or they could not be conducted at all. Maintenance and repairs to the aircraft would be conducted when the SHM system dictated they were necessary. This should decrease maintenance time and consequently

reduce direct operating costs and improve aircraft availability.

Improving structural design. Increased knowledge of a structure's health should allow weight saving because less redundancy is required for tolerance of previously unknown damage. For example a wing box may be designed with the assumptions that a certain percentage of the bolts have failed and that this may be unknown for some time because they are not easily accessible to inspect. A SHM system could reduce the unknown factor.

Monitoring fatigue rate. Knowing the rate of fatigue on certain components would allow them to be used to their full life. The information from this could be used to manage maintenance times and maintenance locations and benefit organisation such as informing the ordering of new components.

Gaining insight into existing aircraft designs. Information gained from monitoring a fleet of aircraft to a high level of detail could be a useful design tool as weaknesses in previous designs or over cautious designs would be highlighted.

1.3 Active and passive guided wave structural health monitoring

The two SHM technologies that will be considered in this thesis are both techniques which depend on the propagation of ultrasonic guided waves through the interrogated structure. Guided waves are elastic vibrations that exist in a specific geometry. Therefore there are multiple types depending on the geometry. This includes waves that occur in surfaces, at interfaces or in plates [10]. Aircraft structures predominately consist of plates that are connected together. Therefore the type of wave these SHM techniques utilise are those that occur in plates which were mathematically described for an infinite plate by Lamb [11]. Practically these equations can be applied to finite plates.

Guided Lamb waves exist in multiple modes of vibration which can be split into 2 categories; symmetric and anti-symmetric modes. This is where the 2 faces of the plate vibrate either in symmetry or antisymmetry. As the frequency of vibration increases the number of modes increases for both types. Zero order modes contain no stationary nodes within the thickness of the plate. Increasing order of modes contain the same number of stationary nodes as the order. The velocity these waves travel at changes depending on the mode and the frequency. The velocity is determined by the material properties and the thickness of the

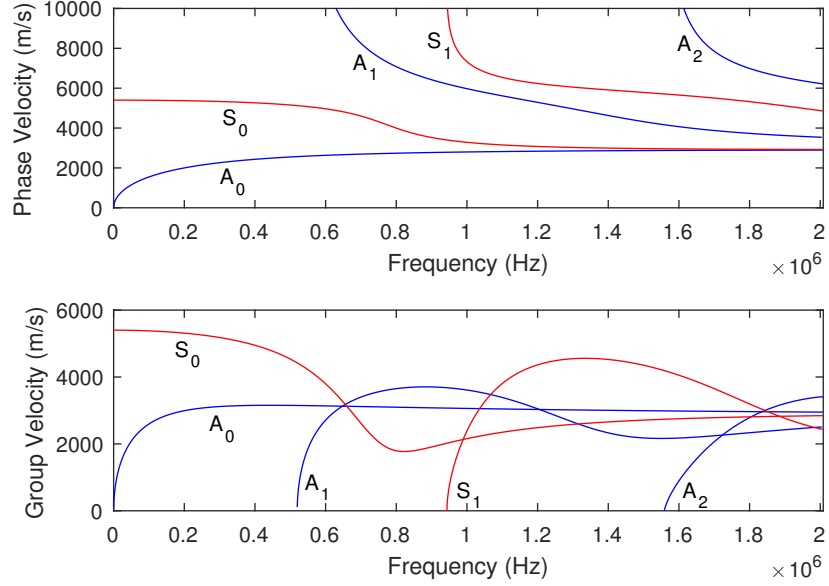


Figure 1.1: The dispersion curves for a 3 mm aluminium plate. The velocities for the symmetric modes (S_0, S_1, \dots) are shown as red lines and antisymmetric modes (A_0, A_1, A_2, \dots) are shown as blue lines.

host plate. The velocities, known as dispersion curves, are shown in figure 1.1 for a 3 mm aluminium plate. Here both phase and group velocity are shown. Phase velocity is the velocity at which the different frequency components in the signal propagate. Group velocity is the velocity the wave packet propagates. Aluminium is an isotropic material which is where the material properties and therefore the guided wave velocities are constant in all directions. In anisotropic materials the material properties and therefore the guided wave velocities vary with angle. An example aerospace anisotropic material would be carbon fibre composite.

Guided Lamb waves have the advantage of propagating over large distances [12]. This enables these waves to be used to interrogate large areas and both AE and active GWSHM utilise this ability. Both types of systems consist of a sparse array of ultrasonic transducers attached to the structure. These transducers are sensitive to the surface vibrations caused by the guided Lamb waves. Depending on the type of the transducer they can also be used to excite guided Lamb waves. The transducers are then connected to processing hardware that interprets the vibrations detected at the transducers. The basic operation of the two guided wave techniques will now be described. Generally the two techniques are used separately but hybrid active and passive AE systems have been shown to

work [13].

1.3.1 Active guided wave structural health monitoring

In an active system the transducers are excited causing ultrasonic guided waves to propagate through the structure to be received by other transducers in the sparse array. This excitation is repeated at a desired time period to monitor the structure over its lifetime. The transducers receive a complex signal which contains reflections from the geometrical features and material changes within the structure. Therefore defects which cause these changes will cause a change in the received signal [12].

The complexity of a received signal from a structure is normally sufficiently great that it cannot be directly interpreted. Therefore to detect defects, changes must be found by comparing signals from different collections.

The most common method to achieve this is baseline subtraction. In its most simple form, a signal is collected when the structure is assumed to be healthy and this is known as the baseline. This is subtracted from all future signals. If no damage has occurred then these signals theoretically will be the same as the baseline so the residual signal will be zero. If damage does occur then this will change the wave propagation within the structure. This will cause the received signal to contain reflections from the defect. Therefore when the baseline is subtracted only the defect reflections will remain in the residual signal and this will allow the defect to be detected.

In practice, even if the structure remains healthy, none of the signals collected will be exactly the same due to changing operational and environmental conditions. This is discussed in detail in chapter 7.

1.3.2 Acoustic emission

An AE system constantly ‘listens’ to the structure for guided waves emitted by defects whilst the structure is loaded. An emission is called an AE event. Any defect which generates mechanical vibration can be detected and these include crack propagation [14] and corrosion [15] for metallic structures and matrix cracking, debonding, fibre pull out, fretting and fibre fracture in fibre based composite structures [16, 17]. These vibrations propagate through the structure as guided waves and are received by the array of transducers. Damage detection is therefore dependant on damage growth or interaction. This means that AE is not a non-destructive technique.

1.4 Challenges in applying guided wave structural health monitoring

There are multiple different facets of guided Lamb wave propagation that need to be considered when using this physical phenomenon for SHM. These are both due to the innate physics of the wave propagation and how the waves interact with the environment.

1.4.1 Dispersion

Guided waves exhibit frequency dependant velocity in a structure. For an active GWSHM system the excitation is typically a tone burst which is relatively short in time. This means it contains a bandwidth of different frequencies. For an AE system the excitation is the vibration caused by crack growth [14] or corrosion [15]. This tends also to be short in time and contain multiple frequencies. The multiple different frequencies in the excitation travel through the structure at their own velocities. If this is in a dispersive region, where the range of velocities is large over a small frequency range, then this will cause the tone burst to lengthen in time over distance. This spreads the energy which decreases the signal amplitude and decreases the temporal resolution. Because GWSHM systems operate over relatively large distances, these two effects can cause significant changes in the shape of the signal envelope, cause nearby arrivals to overlap and reduce the Signal to Noise Ratio (SNR) [18].

In active GWSHM systems regions of low dispersion are typically chosen as the frequency of excitation. In AE systems there is no choice in the excitation frequencies. However the transducer choice can be used to suppress more dispersive modes.

1.4.2 Environmental and operating conditions

An operating aircraft will be subjected to a wide range of environmental and loading conditions and, consequently, so will an attached SHM system. These conditions will not only require robust equipment but will affect the wave propagation within the structure.

Temperature

A major factor affecting the signals is temperature. Only small differences in temperature will cause changes in the received signals so this will affect both in flight and ground-interrogated systems. Temperature affects a materials Young's modulus and causes thermal expansion or contraction in the structure.

This changes the propagation distance, material density and thickness [19] which predominantly has the effect of stretching the signal in time but also distorting the signal's shape [20].

These changes will influence performance in both active GWSHM and AE systems although the former is affected more severely. This is because active systems typically rely on baseline subtraction to obtain useful information from the signals. If the received signal is collected at a different temperature to the baseline then each signal will be subjected to a different stretch. This will mean parts of the signal will be more out of alignment and consequently not subtract to zero which will increase the amplitude of the residual despite no damage existing. Because subtraction is applied to the radio frequency signal [12] a small misalignment can quickly cause a large residual as peaks and troughs overlap.

Temperature effects will similarly change the received signals in an AE system. Here parameters such as the first arrival time are typically used for detection and localisation instead of the whole wave form. Therefore the effects on AE systems performance will be different. A small misalignment in time will not affect event detection as significantly as with baseline subtraction but will cause a localisation error.

Load

For an operational system it is likely that the structure will be under load during the collection of guided wave signals. This is almost certainly the case for an AE system due to the necessity of load to generate AE events. Load will cause the structure to deform and be subject to stress, both of which will cause changes in the wave propagation. This results in different wave velocities [21, 22], signal distortion and amplitude changes [23]. These changes will affect active and AE systems similarly to temperature changes and have the potential to affect performance. However, unlike with temperature, signal processing techniques have not been developed to specifically compensate for these changes.

1.5 Operation of an acoustic emission system

The main focus in this thesis is upon AE systems. This section will describe how this type of system operates. It will consider the components and the processing used to obtain useful information after the guided waves have been received. Therefore prior to this the guided waves have been generated by an AE event, propagated through the structure and reached the transducers.

1.5.1 Guided wave transducers

A guided wave transducer is required to convert the vibration in the plate caused by the guided wave to something that can be interpreted by the data processing hardware. This is normally an analogue electrical signal which is often then digitised by the data processing hardware. There are many different types of guided wave transducer including those based on the piezoelectric effect, Electro-Magnetic Acoustic Transducers (EMATs) and fibre optic transducers.

Piezoelectric transducers contain an active material which exhibits the piezoelectric effect [24]. This is where, when the material is deformed, a voltage is generated and by measuring this voltage the vibration on the surface of the structure can be found. The converse mechanism is possible for most transducers where applying an alternating voltage will cause the transducer to vibrate the structure and generate a guided wave. A wide variety of piezoelectric sensors are available for commercial purchase including those for specialist applications such as airborne applications [25]. Piezoelectric based transducers generally have a high transduction efficiency meaning that a large amount of voltage is generated for comparatively small surface vibrations. For AE applications piezoelectric transducers are bonded to the structure using either permanent or semi-permanent adhesives.

An alternative type of transducer is the EMAT. Within an EMAT is a permanent magnet and an electrical coil. The magnetic field permeates into the surface of the plate it is placed upon. An alternating current is passed through the coil and this generates eddy currents within the surface of the material. This requires the material to be an electrical conductor. These eddy currents interact with the constant magnetic field via the Lorentz force which generates vibration within the material. The converse operation also occurs so EMATs can be used to both detect and generate guided waves [26]. EMATs generally have a lower transduction efficiency than piezoelectric transducers. They do not need to be bonded to the surface to generate waves. This means EMATs are more generally used for active GWSHM applications where only temporary attachment is required [27, 28]. They are not generally used in AE systems but will often be used in this work due to the ease of moving the transducer.

The final type of guided wave transducer used in AE systems is fibre optic based transducers. In this type of transducer an optical fibre is bonded to a small area of the monitored structure. The optical fibre is therefore subjected to any strain in the material including that generated by a guided wave. The strain in the fibre is measured optically either from a moving reflective surface [29] or the effect of strain on a fibre Bragg grating [30]. Fibre optic systems have great potential for integration into structures, especially embedding into composite

structures [31]. Optical fibre based transducers can only detect guided waves. It is not possible to use them to excite vibrations.

1.5.2 Determining arrival times

After the transducers have converted the vibration in the structure to an information carrying signal, normally an electrical signal, this is passed to the data processing components within the AE system. The first step is often some analogue signal processing. This could include a filter to cut out frequencies that are not of interest or an amplifier to increase the voltage the signal. The next major step however is determining what in the received signal is a guided wave generated from an AE event and what is background noise.

For these systems to operate it is normally necessary for the signal generated by the guided wave to be larger in amplitude than the signal generated by the background noise. This places complex requirements on the design of many components within AE systems and the setup they are used in and these will be discussed throughout this thesis. If the guided wave signal is larger than the noise then the simplest method of determining when a AE event has occurred is threshold crossing. A threshold voltage is set and when the amplitude of the signal or, more often, the rectified signal exceeds this value it is determined that an AE event has occurred and the time it has occurred can be recorded. The threshold value is often set with respect to the amplitude of the background noise. A problem with this method is it takes some time for the amplitude of the signal from the AE event to rise to this threshold so there is some inherent error in the arrival time. This has implications on the performance of other components within the system, most notably the location performance. The error in arrival time increases as the SNR decreases.

To reduce this error statistical methods have been attempted to determine a more accurate arrival time. These methods include cross-correlation with an approximated AE source [32] and utilising the Akaike information criterion [33] or the Rayleigh maximum likelihood estimator [34] to determine the difference between background noise and coherent signal. All of these methods show an increase in the accuracy for the arrival time and variously demonstrate how this improves overall AE system performance. The challenge in implementing these methods is they require more complicated processing when compared to the threshold crossing method. They need to be applied to the full waveform from the structure and this requires much more complicated hardware and greater computational power than the threshold crossing method. This is a disadvantage when one data processing unit may need to handle the signals received from a large number of transducers.

1.5.3 Locating acoustic emission events

If the AE event is detected on multiple receiving transducers then the event can be localised. This enables the location of the damage causing the AE event to be identified and this is often the main requirement of the SHM system. Locating the event is typically achieved through time of flight calculations which triangulate the event location. This utilises the arrival times determined by either the threshold method or the other techniques described in the previous section and the velocity profile of the material. This is complicated by guided waves exhibiting multiple modes and frequency dependant velocities. This often leads to choosing transducers which will be sensitive in a defined frequency range and which favour a specific mode.

In an isotropic material and a simple structure the modal velocities can be assumed to be constant in all directions and therefore the location of an AE event can be triangulated. An analytical method of doing this was presented by Tobias in [35]. A refinement of this technique was developed by Paget *et al.* [36] which assumes an elliptical velocity profile suitable for quasi-isotropic materials and unidirectional composites. In anisotropic materials or structures with complex geometry, the velocity profile is not constant and source location becomes challenging. In some cases a unique position cannot be determined. Scholey presents a numerical method for source location in these cases which proves effective but precise knowledge of the structure and material is required [37]. A look up table of arrival time differences is calculated analytically and used to infer the source position. In a related technique, “Delta T Mapping”, these look up tables are experimentally collected by signals from an artificial source in a grid pattern over the area of interest [38, 39]. “Delta T Mapping” can be used on materials or geometries where an analytical or numerical approach would be impractical.

Alternative methods for AE source location exist. One method is triangulating the event from the strain angle detected from the propagating wave. This requires no knowledge of the velocity profile within the structure, but does need a rosette transducer which has a very directional behaviour, and cannot be achieved with typical omnidirectional AE transducers [40, 41]. The angle of the incident wave is calculated by comparing the response of different segments of the rosette. The incident wave angles from multiple transducers are then used to triangulate the source. Another method that does not require prior knowledge of the structure is presented by Ciampa and Meo [42]. Here pairs of closely spaced transducers are used to calculate the group velocity within the structure for each event. This can then be used to triangulate the position of the AE event. This technique can be applied with traditional transducers

but assumes that the group velocity is constant in the direction of reception. The technique therefore works well for anisotropic materials but possibly not for complex geometries.

1.5.4 Classifying acoustic emission events

The final possible task of an AE system is to determine the type of damage that is causing the AE events. This uses information from the received AE signals. Excepting the statistical arrival time methods, it can be seen that most of the additional information contained within the received electrical signals is discarded by typical AE system processing. This can potentially be used for classifying AE events and thereby identifying damage types. A variety of methods for doing this have been presented. This includes classifying defects by received energy [43], frequency [16], wave mode and amplitude [17]. The wide variety of different techniques however makes comparing results difficult, as was noted by Scholey [44]. This is not an area that will particularly be focussed upon in this thesis as there are sufficient challenges performing the previous steps well. However it remains a long term goal in the field to implement this kind of capability in AE systems.

1.6 Acoustic emission testing at Airbus

Airbus has two main use cases for AE; monitoring structural tests and monitoring in service aircraft. Currently AE systems are used to monitor some structural tests but the systems have not yet reached the maturity to be applied to flying aircraft.

During the development of aircraft many test specimens are loaded to test designs, verify modelling of the components and to understand how damage develops. This is a key part of designing and qualifying a safe aircraft. The specimens are loaded in two broad ways; ultimate load tests and fatigue tests. The specimens can vary in size from an individual component to a whole aircraft. During these structural tests the specimen is inspected and monitored by many NDT techniques to increase the understanding of how the component behaves under the load and the mechanisms by which it fails. This information can be used to develop the design of the specimen. AE is one of the techniques which can be used to monitor the specimen. It has the advantage that it can provide close to real time information about the AE events and therefore damage occurring throughout the structure. Most other techniques can only be applied when the specimen is not under load so as not to endanger the practitioner of the technique or only supply information about a small area of the structure. This

real time information can be of particular use if the specimen is not behaving as it was expected to or if the aim of the test is to stop it when the damage is only part formed.

A more hypothetical use of AE systems is to provide a SHM capability which could be applied to in service aircraft. The potential benefits of this were discussed in section 1.2. Currently the experience gained using AE systems on structural tests is enabling development of the equipment and the methodology of applying AE. As the technology matures more possible applications for its use will occur which could lead to its greater deployment.

Airbus has developed, with collaborators, several different AE systems. The system used to monitor structural tests is the British Aerospace Lloyd's Register Ultra Electronics (BALRUE) system. This is a wired AE system that was developed by the Experimental Mechanics Group of Airbus UK, the Technical Investigation Department of Lloyd's Register EMEA and the Ultra Electronics Ltd. [45]. Each BALRUE unit has from 12 to 48 input channels depending on the type of unit and each channel is connected to a preamplifier which is connected to a transducer. Different frequency transducer and preamplifier pairs are available from 90 to 900 kHz. The frequencies most commonly used are 150 and 300 kHz. The BALRUE unit applies analogue signal processing to the received signals and extracts and digitises certain parameters from the signal. These parameters are stored in files with one line for each AE event. These lines are called burst descriptors. This approach was chosen and full AE signal were not recorded to enable the system to process large amounts of closely spaced in time AE events. This also keeps the size of data generated by the system at a manageable level. The system connects to a control computer via Ethernet for setting up the system, live monitoring if required and transferring the AE data off the unit. Each unit can operate on its own if required. There is accompanying software to process and visualise the received data. Flight safe versions of the BALRUE have flown on test aircraft.

A lot of the work in this thesis is applicable to any AE system but many examples will be based upon the BALRUE system. This is because it is the most commonly used system at Airbus and there are many examples and datasets from past tests using these systems.

1.6.1 BALRUE data processing

How the BALRUE system processes the signals it receives will now be described in more detail. The BALRUE system is designed to be able to process a large throughput of AE events. To enable this, and to keep the amount of data to a manageable level, the system processes each of the received signals and records

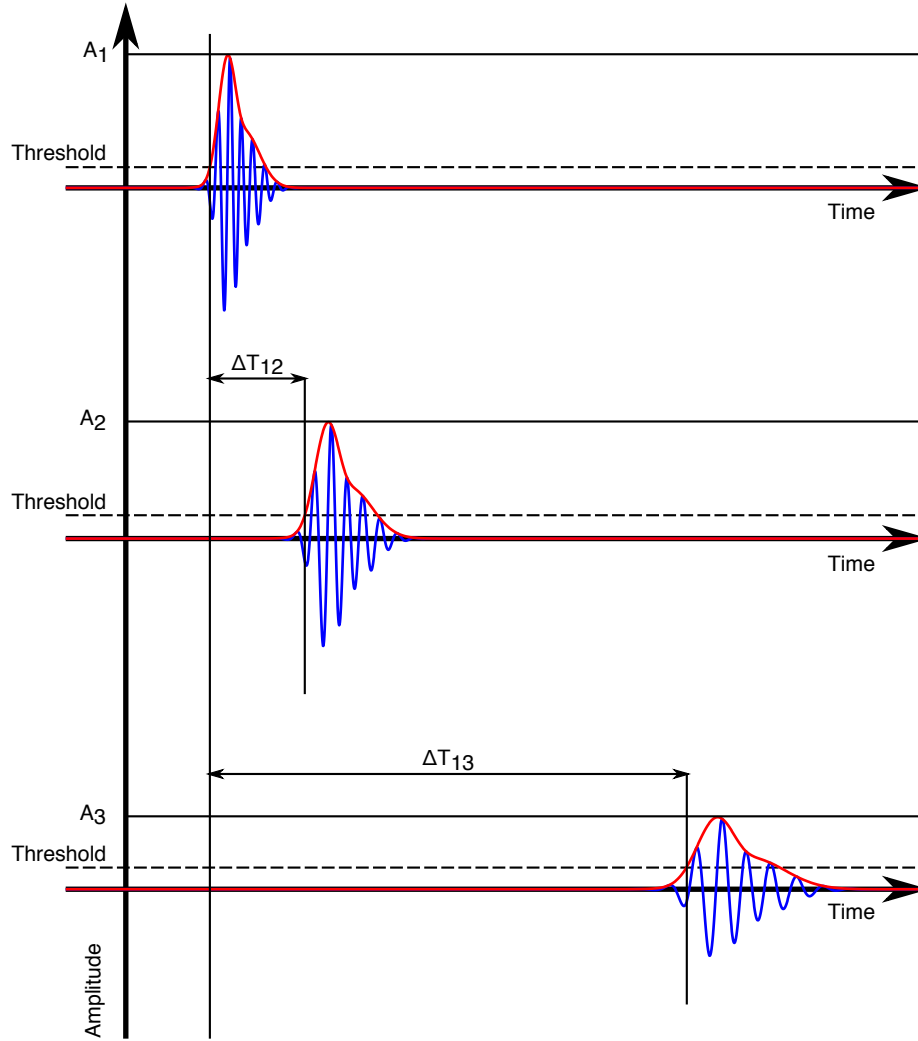


Figure 1.2: The threshold processing applied by the BALRUE system on the signals from the first 3 triggered transducers. This shows how the arrival time differences (ΔT_{12} , ΔT_{13} ,...) and maximum amplitudes of the envelope of the signals (A_1 , A_2 , A_3 ,...) are found. This processing is applied to the signals received from all of the transducers triggered by an event. This could be more than 3 transducers.

certain parameters. The processing is as follows [46]:

- A channel is triggered if the received amplitude exceeds a defined voltage. This value is typically set at double the amplitude of the background noise.
- A minimum number of hits is defined. At least this number of channels must be triggered within a defined maximum event duration for the system to register an event. All channels which trigger within the period defined as the event duration are grouped as one event. Typically the minimum number of hits is set as 3.
- An additional requirement before the event is recorded is the phenomenological filter. Separate thresholds in amplitude are applied for the first three triggered transducers. These thresholds are set to decreasing values as it is anticipated that beam spread will have caused the amplitude of the signal to decrease on the later received signals which will have travelled further. Events which do not satisfy the phenomenological filter are discarded. The aim of this filter is to prevent spurious events being recorded.
- The times at which the different transducers are triggered are recorded. The first time is recorded as the time the event occurred. The difference between this time and the times the other transducers were triggered are also recorded. These times are referred to as the ΔT times. A graphical example of how these are calculated is shown in figure 1.2.
- Other parameters describing the waveform received on each transducer are recorded. The most important of these is the maximum amplitude of the envelope of each of the received signals. How this is calculated is shown in figure 1.2.
- After the maximum event duration has passed the system waits for the next triggering event.

1.6.2 Limitations of current testing

One of the main reasons this Engineering Doctorate project was initiated is to address the issues that arose during large scale fatigue tests of the A380. Up until this point AE tests conducted with the BALRUE AE system had generally performed well with high detection rates and reasonable location accuracy. The A380 test was a large scale and ambitious test where the system did not perform well. The AE system was monitoring a section of the wing close to the fuselage during a fatigue test on the whole aircraft structure. The area monitored included both wing skins and the ribs between the two skins. The transducers

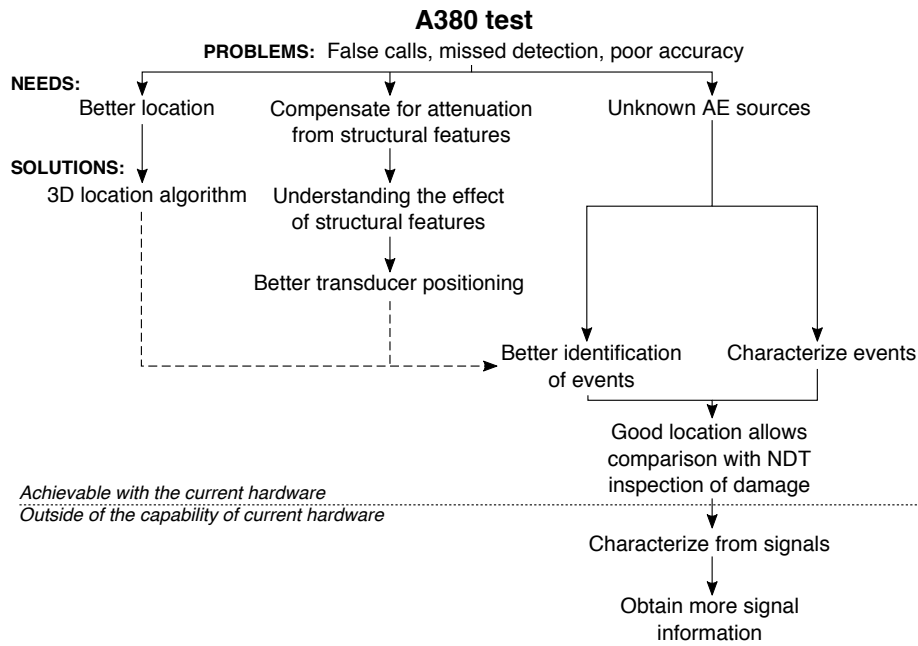


Figure 1.3: A diagram illustrating the proposed solutions to the problems which occurred with the Airbus A380 test.

were placed on the outer side of the wing skins on both the top and bottom skin. The system was therefore monitoring a complex 3 dimensional structure. The transducers were placed with a large spacing between them compared to previous tests. The results of this test were poor with a high false call rate, missed detection of damage identified by NDT and poor location accuracy when tested with simulated AE sources at known locations. This test highlighted many issues with AE testing at Airbus. These need to be addressed prior to its further use in similar scenarios.

To address the issues highlighted by the A380 test, the limitations of Airbus AE testing need to be identified. What the author believes these to be has been summarised in figure 1.3 and are explained below:

Better location

If the location algorithms could be improved then the location accuracy would be better. It is also likely that some of the false calls and cases of missed detection would decrease as these would instead be identified as damage.

The software used for location is limited to 2 dimensional location in one plane. It is therefore likely that this approach is not performing well on the 3D plate like structure monitored in the A380 test. This is especially the case as much of the damage occurred on the ribs which are perpendicular

to the skin and therefore perpendicular to the location plane. Techniques for 3 Dimensional (3D) location exist [37] so it is likely this problem could be solved. However to implement a 3D location algorithm in easy to use software for a complex aircraft structures containing multiple materials would be challenging. This would require significant effort and resources to implement.

Compensating for attenuation from structural features

The effects of structural geometry on system performance are not currently considered in a rigorous way when setting up AE tests at Airbus. Each geometrical change will cause some attenuation of the transmitted signal. Therefore if the transducer positioning means that the guided wave generated by an AE event has to cross many geometrical features, the amplitude may become too low for it to be detected. This could potentially be a cause of missed detection and the change in amplitude also has implications on location accuracy. An improved understanding of the wave propagation within the structure could therefore benefit the performance of system.

Unknown AE sources

To understand the false calls it would be useful to have a better understanding of the sources of acoustic signals in these structural tests. The AE events which are of interest are from damage occurring. These sources do not necessarily generate the largest quantity of events and can be hidden by spurious events of unknown origin [47]. To begin characterising the AE sources it would be necessary to have a good probability of detection and accurate location. It is therefore probable that the above problems need to be addressed prior to this one. If they are addressed then it would be possible to compare areas of high number of AE events with NDT inspection of the same area. This may aid in understanding the source of and reduce spurious AE events.

Ideally it would be possible to characterize the AE source directly from received signals although the literature suggests this is very difficult. For reasons of restricted data storage, the BALRUE system is designed to only store limited information about each AE event. It is unlikely this is sufficient information to perform a characterisation where, at least to begin with, the whole acoustic waveform would be useful. To achieve this, it is likely that different hardware would be required.

1.7 Aims and outline of this thesis

The previous section has highlighted several limitations in the application of AE at Airbus. These need to be overcome prior to the further adoption of this technique for similarly complex structural tests and the future potential use to provide SHM. It was chosen to focus on improving understanding of how the structure affects system performance. This was because this had the potential to improve the setup of AE systems on new tests. With a better setup location performance is likely to improve, even without improvement to the location algorithms, and a better understanding of what AE events can be detected will be obtained. To achieve this improved understanding, modelling of the whole system will be developed. This will predominately focus on the wave propagation within the structure. Other significant components within the system will also be modelled to understand the overall effect on the whole system performance. It should also be noted here that this thesis will focus on isotropic aluminium structures. This was done to remove an additional layer of complexity that comes with anisotropic materials [48]. However this is a layer of complexity that could be added to the modelling at a later date.

The first necessary component of the overall system model is an understanding of the AE sources that would be occurring in aluminium aircraft structure. This is done in chapter 2 where a candidate AE source is found from the literature. This is then compared to the data received from an Airbus structural test on a A340-600 airframe. The overall system model is also described in detail in this chapter. The next chapters then focus on developing an approach to model the wave propagation in the structure. The aim of this approach is for it to be practical to implement for a structure containing multiple geometrical features. This has led to the development of an empirical modelling approach for the transmission across geometrical features. This is demonstrated for stiffening features in chapter 3 and these are experimentally validated in chapter 4. Chapter 5 shows example uses of the overall system model to demonstrate the effect of the structure on different parts of the system. These models use the feature models and AE source developed in the previous chapters.

During the work on validating the empirical transmission models a concept for efficiently collecting simulated AE event data was developed. This is shown in chapter 6 and demonstrated on simulated and experimental data. The final work addresses another challenge that needs to be overcome for greater uptake of GWSHM. That is the long term performance of these systems. There have not been many examples of successful operation of GWSHM systems over long time periods reported in the literature. Chapter 7 analyses the results from a long term active GWSHM experiment and discusses the implications of these

results on both active GWSHM and AE systems.

1.8 Novel contributions of this thesis

The work in this thesis has several novel aspects and these will now be described. During this project, there has been the opportunity to compare the characterisation of an AE source from a fatigue crack in an aluminium plate with the results from a fatigue test on a whole aircraft airframe. There are many different sources of AE in the fatigue test dataset, some classified and some unknown, but it is thought many are fatigue cracks growing from features in the aluminium structure. This analysis is described in chapter 2. It was found that the amplitude of the AE sources in the fatigue test were significantly larger than those characterised in the literature. This raised questions about whether this was truly the case or whether the AE sources recorded in the fatigue test were from a different and larger amplitude source.

The second novel aspect of this work was the development of a modelling approach that accepted limits in the accuracy in the model to enable it to be used within the available resources. Several conservative assumptions were included in the model to simplify it and to ensure it would not over predict the amplitude of the propagating ultrasonic wave. This is necessary because the main factor in the detection of these waves and thereby the corresponding AE source is the maximum amplitude of the first arrival. Therefore it is preferable to under predict the wave amplitude but guarantee detection, so the model is biased in this direction. Development of different components of the model are described in chapters 2 to 4. Examples showing how this modelling approach is useful and can be used to simulate thousands of scenarios are described in chapter 5.

A component of the overall AE system model that was focussed on in this work is the transmission of the guided waves over geometrical features in the structure. The transmission over 3 different line features was experimentally characterised and from these results empirical models were generated. The generation of these models is described in chapter 3 and their validation in chapter 4. The novel aspects of this work are the conservative assumptions in their creation, as described above, and the use of 1 model to represent 2 similar features. Given the large number of similar but not identical features in an aircraft it would be desirable to group similar features together to reduce the modelling effort. For the 2 features here the approach works quite well but further work would be required to use this approach with confidence.

To experimentally validate models of guided wave propagation in complex structures it may be necessary to collect data at many different positions across

the structure. During the work in this thesis it was found that this was prohibitively time consuming for large 2 Dimensional (2D) areas. To reduce the data collection time a novel data collection approach has been proposed and it is described in chapter 6. The model is based upon Design of Experiments (DoE) principles with an iterative active learning step. The algorithm aims to collect data where the parameter of interest is changing in a way that does not fit simple planar models. The algorithm has been shown to be able to reduce the number of collection points during validation experiments by a factor which approximately corresponds to the geometrical complexity of the structure.

The final novel aspect of the work is described in the chapter on the long term performance of GWSHM systems. Anecdotally the performance of active GWSHM systems degrades over time. There has not been much work on the long term performance of these systems presented in the literature. Chapter 3 describes the results of monitoring a water tank subjected to real environmental conditions for a time period of more than 3 years. It was found that individual signal parameters have not changed significantly over this time period but that, despite this, the performance of typical active GWSHM processing techniques degrade over short time periods. The implications of these results for both AE and active GWSHM systems are discussed in this chapter.

Chapter 2

Acoustic Emission Sources

2.1 Introduction

To determine the overall performance of an AE system the AE source must first be defined. When modelling an AE system, the output of the model will be dependent on what is used as the source. For the modelling to be useful it is therefore important for the AE source model to be representative of the AE sources generated by the types of damage the system is expected to detect.

In the first part of this chapter the modelling approach for the entire system is described. After this the chapter focuses on defining an AE source. Two approaches to pick a suitable or multiple suitable AE source models have been attempted. First a literature search has been conducted to find suitable AE sources in aluminium aircraft structures. This will then be compared with data from a past Airbus structural test where the BALRUE system was considered to have performed well. This will enable a comparison between what Airbus believes it has been detecting and the literature to be made and allow source models for use in later modelling to be defined.

2.2 The linear time-shift invariant systems modelling approach

To model the whole of a AE system a modelling approach must be chosen. The requirements for this approach are that each component in an AE system can be included in the model. To determine the overall performance of the system multiple scenarios must be possible to test quickly. Therefore the modelling approach needs to be flexible and have reasonably low computational demands. The modelling approach that satisfies these requirements is the framework de-

veloped by Scholey in [44]. This work comprehensively covers each component of an AE system. The framework uses the Linear Time-shift Invariant (LTI) systems approach. In this model each component in the system is modelled in the frequency domain. The model for each component can be found by multiple different techniques and they can be used interchangeably. These techniques could include multiple different modelling techniques or experimental characterisations. This gives the overall model great flexibility and enables the modelling effort to be tailored to specific elements where necessary. In this work the major effort has been expended on the components related to the structure and the AE source.

The overall system equation is:

$$H(\omega) = S(\omega)U(\omega)Y(\omega) \sum_{ray\ paths} \left[R_X(\omega)E(\omega)P(\omega)A(\omega)B \prod_{reflections} R_C(\omega) \prod_{transmissions} T_C(\omega) \right] \quad (2.1)$$

Where:

ω Angular velocity

$H(\omega)$ Received signal frequency spectrum

$S(\omega)$ Source frequency spectrum

$U(\omega)$ Amplifier transfer function

$Y(\omega)$ Post processing

$R_X(\omega)$ Receiver transfer function

$E(\omega)$ Excitability of elastic waves at the source

$P(\omega)$ Phase delay due to propagation

$A(\omega)$ Attenuation

B Beam spread

$R_C(\omega)$ Reflection coefficients from all features the ray is reflected from

$T_C(\omega)$ Transmission coefficients from all the features the ray has passed through

The sum is applied over relevant ray paths.

Two key components of this model which remain constant throughout the modelling in this thesis will now be described in more detail.

Phase delay due to propagation This term models the time it takes for the wave to propagate through the structure. Given guided Lamb waves are dispersive in nature, different frequency components in the wave will travel at different velocities. The frequency dependant velocity will also vary depending on the mode of the wave. The equation to model this component is:

$$P(\omega) = \exp\left(-\frac{i\omega d}{v_p(\omega)}\right) \quad (2.2)$$

Where d is the distance travelled by the wave and $v_p(\omega)$ is the frequency dependant phase velocity for the mode being modelled.

Beam spread The AE sources and transducers are modelled in this work as point sources. In a thin plate the energy released from the point will radiate out via a circular wave front. The energy at each radius remains constant but because the wave front is increasing in length the amplitude of the wave decreases. This is modelled by:

$$B = \frac{1}{\sqrt{d}} \quad (2.3)$$

Where d is the distance travelled by the wave.

The section of the overall model which will now be focussed upon is the AE source, $S(\omega)$. The importance of this term can be seen in equation 2.1 as it effects the entire output of the model.

2.3 Literature on acoustic emission sources in aluminium

A literature review has been conducted to find a realistic model of an AE source or sources in aluminium relevant to aircraft structure. Aircraft generally consist of a structure made from plates so the most relevant source is fatigue crack growth in plates, often from a point of stress concentration such as fastener holes or points of corrosion [2]. It should be noted that due to the limitations described in the following paragraph and that more recent AE characterisation work has focused on composite materials, there are few cases where the necessary information is available.

An important factor to consider is the size of the specimen used for the AE event characterisation. This factor is raised by both Hamstad [49] and Gorman [50] and they demonstrate the restrictions of using narrow specimens. In a narrow specimen, the direct path arrival is not distinct from edge reflections due to the small difference in paths for these arrivals. The arrivals therefore superimpose and this can cause the amplitude of the AE event to appear to increase over time. It is not possible to decompose these arrivals and therefore an uncontaminated characterisation of the AE source is unachievable. Scholey also raises the issue that AE events are likely to emit angular dependant AE and this cannot be characterised on a narrow specimen as the transducers can only be placed to cover one angle [44]. Gagar and Foote [51] propose a method of characterising an AE source from multiple angles on a narrow specimen but experimental results from this have yet to be published. Considering these limitations of narrow specimens, only results from specimens which can provide a clear direct path arrival will be considered.

In a series of papers, Scruby *et al.* quantitatively characterize AE events in the bulk of different materials. These include aluminium [52] and steel that has been exposed to different environmental conditions [53]. These characterisations are in great detail and list values including the amplitude of the pulse on the surface, the source strength and its orientation, assuming that the source fits a point source model. These characterisations can only be directly used to predict the waves received at the surface from a source when the receiver is very close to the event. In a plate like structure the pressure waves from the event are converted into guided waves before detection by a transducer. Work by Ceranoglu and Pao [54] and Weaver and Pao [55] describe methods to calculate the guided waves produced by an excitation in the body of the material via the the normal modes method, for the intermediate and far field, and a ray path method, for the near field up to a distance of 6 plate thickness. This is demonstrated in [56] but the result is not confirmed experimentally. These two methods of predicting the guided wave generation would be useful in understanding in detail how the excitation occurs but an experimentally validated value for AE guided wave amplitude would be preferred.

Most probably due to the large forces required to perform fatigue tests on wide plate specimens, only one characterisation of AE events in aluminium has been found. This was conducted by Lee *et al.* [14] and presents the received waveform with a voltage scale. The plate had a droplet shaped hole made in the centre of the plate which initiated a fatigue crack. AE events were recorded as the crack grew and the waveform of a typical signal is shown in the paper. The S_0 arrival has an amplitude of about 0.01 V and the A_0 arrival has an amplitude of 0.08 V. The S_0 arrival is only just distinct from the noise. This experimental

information is very useful to build a source model because fatigue cracks from points of stress concentration are a very common type of damage in aluminium aircraft structure. The amplitudes presented in the paper are voltages and there is insufficient information to remove the effects of the transducers and transducer bonding exactly. However in the next section an attempt will be made to build a plausible source model with this information and estimate the possible upper and lower bounds of amplitude for comparison with the Airbus AE data examined later.

2.3.1 Estimating the amplitude of acoustic emission events from a fatigue crack in aluminium

In this section an estimate of the amplitude of an AE event from a fatigue crack in an aluminium plate will be constructed from the work by Lee and Scholey in [14] and [44]. In most of the work by Scholey, AE event amplitude was calculated and displayed as surface displacement at the source. This is ideal for further use in modelling as the effects of wave propagation and the receiving transducer are removed from this characterisation. The source characterisation still includes material properties and material thickness. Unfortunately the results in [14] are presented as the voltages measured at a transducer. Therefore the amplitudes measured here also include the effects of propagation in the plate, the transducer and the bonding of the transducer. In the paper there are insufficient details of the bonding and bonding procedure to repeat this and do an experimental characterisation. Instead the description of the experiment and the characterisations of transducers in [44] will be used to estimate a range of plausible surface displacements for this type of source.

The similarities between the experimental setups in [14] and [44] enable these calculations to be conducted. The components of each work used are (a) the example AE signal from [14] (b) the transducer characterisations from section 4.2.1 of [44] and (c) the Pencil Lead Break (PLB) signal from section 9.3.1 of [44]. All of these experiments were conducted on aluminium plates. The thickness of the plates for (a) and (b) are described as 3 mm. The thickness of the plate in (c) is not described in that section. It is assumed that the characterisation has been conducted consistently with the other characterisations in that work and is therefore 3 mm. All of the experiments were conducted on large plates so the results were not contaminated by overlapping modes. The bandwidth of the filters used in the experiments are similar. All have a centre frequency of 250 kHz. The bandwidth of the filters varies between 300 and 350 kHz. It is assumed that this has no significant effect because the majority of the energy in the signals is at the centre frequency.

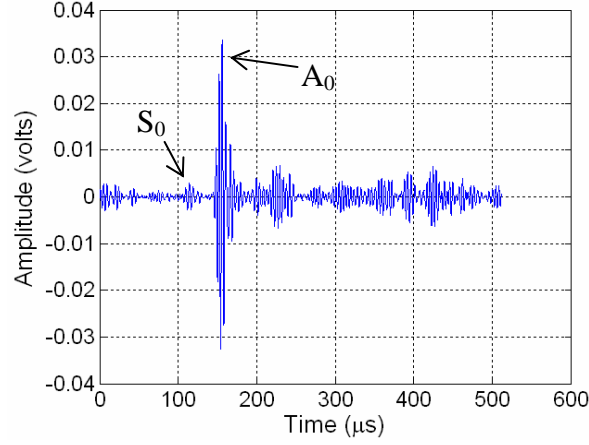


Figure 2.1: Reproduction of figure 2b from [14]. This shows the filtered waveform received from a growing fatigue crack in an aluminium plate. It is referred to here as (a).

First the maximum voltage, M , of the arrival for each mode has been found from (a). The relevant graph is reproduced here as figure 2.1 and the values taken from it are shown in table 2.1. There are 2 possible signals that could be used from [14]; a unfiltered and filtered signal. The 250 kHz filtered signal was chosen as it is more similar to the filtered PLB signal, (c), used later. The filter was a band pass filter between 75 and 425 kHz.

	A_0	S_0
$M^{250 \text{ kHz}}$	0.0338 V	$2.89 \times 10^{-3} \text{ V}$

Table 2.1: The maximum amplitude of the first arrival for each mode from a fatigue crack in an aluminium plate. The values are taken from [14] and referred to here as (a).

The exact sensor and bonding used in experiment that generates (a) are unknown. A range of transducers are characterised in (b) and it is assumed that another transducer and bonding combination is unlikely to be significantly more or less sensitive than these transducers. Therefore these calculations will be performed for each of the 4 piezoelectric transducers characterised in (b) to give a range of plausible values. From these characterisations the frequency response of the value D is found at 250 kHz for both modes. D is the ratio between the signal voltage measured at the transducer and the absolute surface displacement measured at the transducer position. The values of $D^{250 \text{ kHz}}$ for each type of transducer are shown in table 2.2.

Transducer Type	A_0	S_0
pz-27	$4.56 \times 10^{-5} \text{ V/pm}$	$4.38 \times 10^{-5} \text{ V/pm}$
pz-35	$7.09 \times 10^{-6} \text{ V/pm}$	$1.06 \times 10^{-5} \text{ V/pm}$
NS3303	$3.77 \times 10^{-3} \text{ V/pm}$	$5.51 \times 10^{-4} \text{ V/pm}$
PAC WD	$1.08 \times 10^{-4} \text{ V/pm}$	$7.30 \times 10^{-4} \text{ V/pm}$

Table 2.2: The values of $D^{250 \text{ kHz}}$ for different transducer types. The values are taken from [44] and referred to here as (b).

The measured displacement, M_0 , at the transducer position can then be calculated using the following equation [44]:

$$M_0 = \frac{M}{D} \quad (2.4)$$

The calculated values for each type of transducer are shown in table 2.3.

Transducer Type	A_0	S_0
pz-27	742 pm	66.0 pm
pz-35	4770 pm	271 pm
NS3303	896 pm	5.24 pm
PAC WD	314 pm	3.96 pm

Table 2.3: The values of displacement at the transducer position, $M_0^{250 \text{ kHz}}$, calculated for different transducer types.

The equivalent displacement at the source can then be found using equation 2.1. For the ray path between source and transducer that does not cross any features and is measured before the signal passes through the transducer this simplifies to:

$$H(\omega) = S(\omega)P(\omega)A(\omega)B \quad (2.5)$$

Which rearranges to:

$$S(\omega) = \frac{H(\omega)}{P(\omega)A(\omega)B} \quad (2.6)$$

This simplifies further when considering only the maximum amplitude of the 250 kHz component of the signal. In this case the received signal, $H(\omega)$, becomes the maximum displacement of the received signal, $M_0^{250 \text{ kHz}}$. The magnitude of the propagation term $P^{250 \text{ kHz}}$ is 1. The attenuation, $A^{250 \text{ kHz}}$, is negligible in aluminium so also goes to 1. Therefore equation 2.6 becomes:

$$S^{250 \text{ kHz}} = \frac{M_0^{250 \text{ kHz}}}{B} \quad (2.7)$$

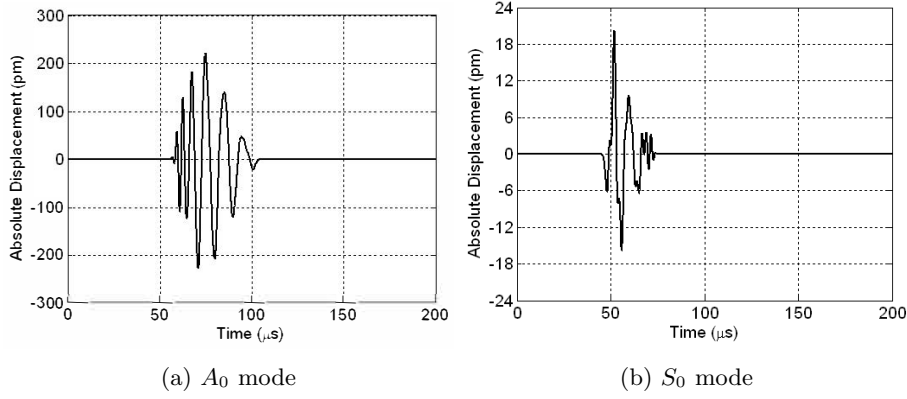


Figure 2.2: Reproduction of figure 9.5 from [44]. They show calibrated and filtered waveforms from a PLB source. They are referred to here as (c).

Where:

$$B = \frac{1}{\sqrt{d}} \quad (2.8)$$

And d is the distance the wave has propagated. Therefore:

$$S^{250 \text{ kHz}} = M_0^{250 \text{ kHz}} \sqrt{d} \quad (2.9)$$

The equivalent displacement at the source can then found and the calculated values are shown in table 2.4. The measurement point was 0.3 m from the source.

Transducer Type	A_0	S_0
pz-27	406 pm	36.1 pm
pz-35	2610 pm	149 pm
NS3303	491 pm	2.87 pm
PAC WD	172 pm	2.17 pm

Table 2.4: The values of displacement measured 0.3 m from the source, $S^{250 \text{ kHz}}$, calculated for different transducer types.

It can be seen that the calculated amplitude at the source varies significantly dependent on the sensitivity of the transducer. Particularly insensitive transducers, such as the pz-35 transducer, lead to very large displacements. This makes it difficult to chose a typical value for a AE event from a fatigue crack in a 3 mm aluminium plate. Due to the large range of amplitudes, the median value of displacement will be used giving a displacement of 449 pm for the A_0 mode and 19.5 pm for the S_0 mode.

Another useful value to characterise a AE event is its ratio in amplitude

compared to an event from a PLB. PLBs are often used to calibrate and setup AE systems so the comparable amplitude of an AE event is a useful number to know. The PLB displacement signal used is (c). The relevant signals are reproduced in figure 2.2. This is measured 0.25 m from the PLB position. Therefore the first step in finding the AE to PLB ratio is to find the displacement of the AE signals at this distance, $M_{\text{AE}}^{250 \text{ kHz}}$. For the reasons stated above, for an aluminium plate, equation 2.5 simplifies to:

$$M_{\text{AE}}^{250 \text{ kHz}} = \frac{S^{250 \text{ kHz}}}{\sqrt{d}} \quad (2.10)$$

Which for the different transducer types gives the surface displacement values at this new position shown in table 2.5.

Transducer Type	A_0	S_0
pz-27	813 pm	72.3 pm
pz-35	5230 pm	297 pm
NS3303	982 pm	5.74 pm
PAC WD	344 pm	4.33 pm

Table 2.5: The surface displacement of the signals at 0.3m from the AE source, $M_{\text{AE}}^{250 \text{ kHz}}$, calculated for different transducer types.

The displacement for the 250 kHz filtered PLB signal, (c), (reproduced here as figure 2.2) is shown in table 2.6. The filter was a band pass filter between 100 and 400 kHz.

	A_0	S_0
$M_{\text{PLB}}^{250 \text{ kHz}}$	228 pm	20.4 pm

Table 2.6: The maximum amplitude of the first arrival for each mode from a PLB on an aluminium plate. The values are taken from [44] and referred to here as (c).

Which leads to the AE to PLB ratios shown in table 2.7.

Transducer Type	A_0	S_0
pz-27	3.57	3.55
pz-35	22.9	14.6
NS3303	4.31	0.282
PAC WD	1.51	0.213

Table 2.7: The AE to PLB amplitude ratio, $M_{\text{AE}}^{250 \text{ kHz}}/M_{\text{PLB}}^{250 \text{ kHz}}$, for a fatigue crack in an aluminium plate calculated for different transducer types.

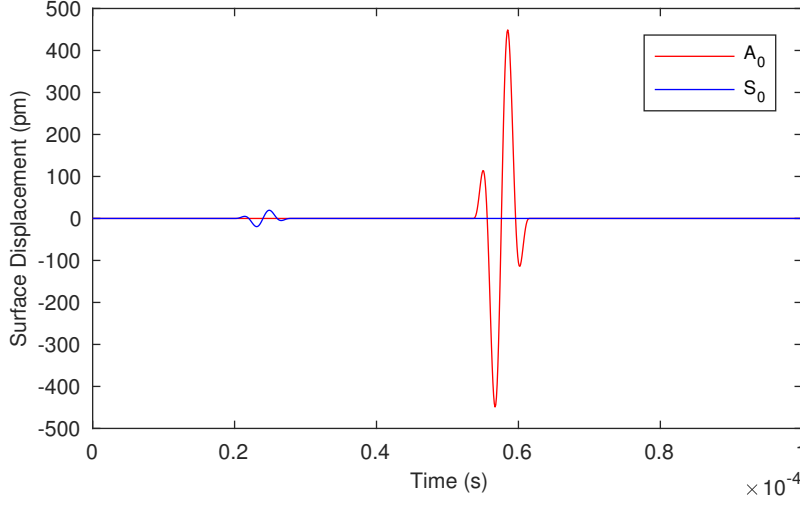


Figure 2.3: The model of an AE source for a fatigue crack in a 3 mm aluminium plate for the A_0 and S_0 mode. The different modes have been arbitrarily separated in time for clarity.

This gives median values of AE to PLB ratios of 3.94 and 1.92 for the A_0 and S_0 modes respectively. This means AE events from a fatigue crack in a 3 mm aluminium plate produce signals with slightly larger maximum amplitudes than signals from a PLB on the same plate.

In addition to the maximum amplitude, the type of excitation must also be defined for the source model. Scholey uses a 2 cycle Hanning windowed tone burst for his modelling work [44]. For consistency and unless otherwise stated, this excitation will also be used in the modelling work in this thesis. The frequency content of this excitation is broad so its dispersion will be relatively large. This means the amplitude decay will be greater with distance than a less dispersive excitation so it is a good conservative choice. The source wave packet is shown in figure 2.3. To be consistent with the work above, its centre frequency is 250 kHz.

Now that an estimate of an AE source from a fatigue crack has been obtained from the literature it will be compared with AE sources collected during a structural test performed at Airbus. The monitored structure is a section of the wing of an A340-600. AE sources will come from many types of damage, from different features, different materials and different material thicknesses. Therefore it is not expected that all of the AE sources will be of similar amplitude but it is expected that aluminium fatigue cracks will be detectable and will be a very common AE source.

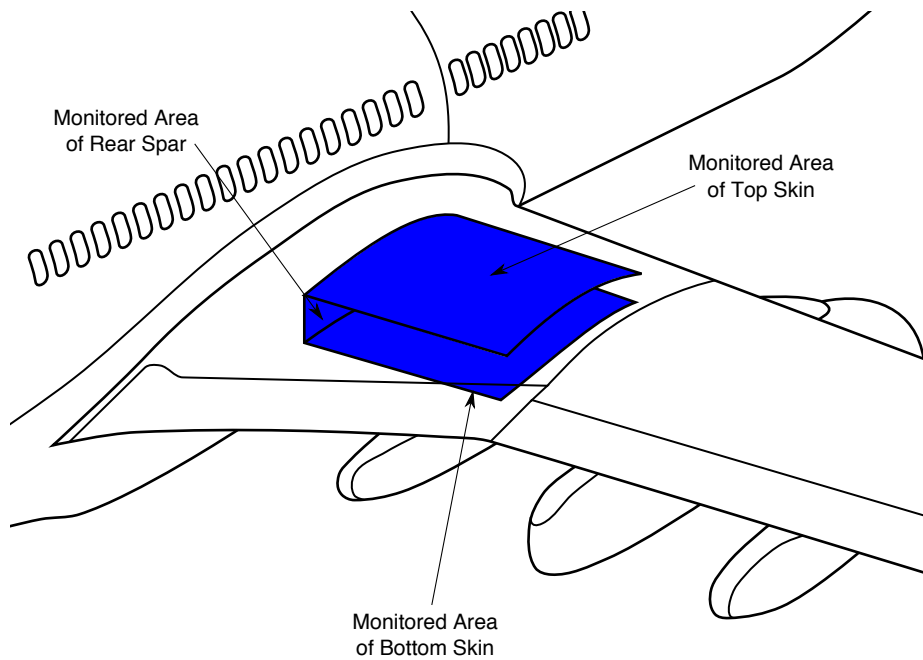


Figure 2.4: The approximate position of the area of the wing monitored with an AE system during a whole aircraft fatigue test of an A340-600. The full details of the AE system setup are available in [45].

2.4 Obtaining acoustic emission amplitudes from a structural test

A BALRUE system monitored a portion of the Right Hand Side (RHS) wing of a A340-600 during a whole aircraft fatigue test. This test occurred from May 2002 to June 2003 [45]. The system recorded the AE events that it detected throughout the test and predicted their location. During the test and after the test was completed the structure was inspected by NDT techniques which identified a number of damage locations. This test is one of the more complex and ambitious tests the BALRUE system has been used upon. The monitored region is shown in figure 2.4. Both the upper and lower wing skins were monitored with an array totalling 24 transducers. The odd numbered transducers were placed on the top skin and the even numbered transducers were placed on the bottom skin. In the data processing software a single 2D monitored region was created which covered both the top and bottom skins and the rear spar which connected the 2 skins. The transducers were 300 kHz McWade NS3303 transducers coupled with 40 dB band pass pre-amplifiers. These band pass filters were between 200 and 400 kHz. The test was considered a success and

there was good agreement between the AE results and the NDT inspections [45]. This test is also more completely documented than other comparable tests and the system performance was thoroughly validated enabling this analysis to be conducted.

After the fatigue test had been completed PLBs, which can be used to simulate AE events, were conducted at the locations identified by NDT. The damage type, where known, is shown in appendix A along with the damage identification numbers which were determined by NDT. This was done to check that the AE locations corresponded with the damage locations. This dataset therefore contains PLB signals which have propagated through approximately the same structural features as real AE events. PLBs are a simple acoustic event to measure and are an experiment which can be repeated on a featureless plate or new structure to be tested. They are often used to test and calibrate new experimental setups. Therefore if an amplitude ratio can be found between real AE and PLB events from similar locations on the A340-600 RHS wing, this ratio can be used to obtain an estimate of the voltage and displacement of an AE event from the results of a fully characterized PLB. This can then be compared with the literature to see if the amplitudes of the AE events detected by Airbus are similar to what is expected for the damage type.

The first step in this work is to identify the AE events which have occurred at a similar location to PLBs.

2.4.1 Matching acoustic emission and pencil lead break events

Figure 2.5 shows the concept behind this data processing. PLBs have been recorded from points close to the damage locations and therefore the guided waves from the PLBs will have propagated along a similar path to the AE events generated at the damage. This means the signals generated by the AE or PLB signal will have been affected by the same structural features and data collection equipment prior to being recorded. For this analysis it will be assumed that the growing damage does not affect the propagation path of the AE sources collected over time. It will also be assumed that the PLB excitations at the damage locations are not affected in a different way to the AE sources. Therefore it will be assumed that the propagation paths for the AE and PLB signals are identical. When considering this with respect to the LTI systems model shown in equation 2.1, this means all of the transfer functions cancel and the ratio between AE and PLB signal amplitude can be found from the ratio of the recorded signals.

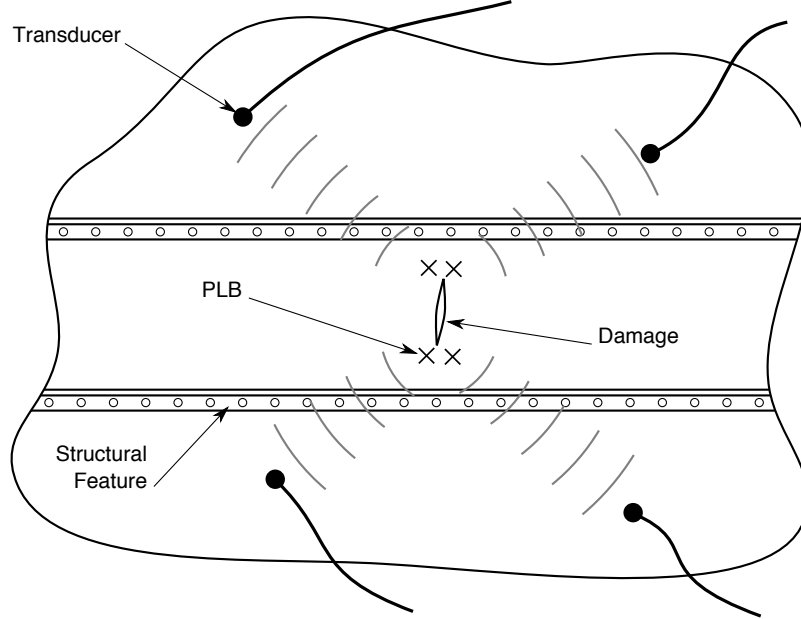


Figure 2.5: An illustrative diagram of collecting PLB signals from locations near damage on the A340-600 test.

This is shown for the first arrival of each signal by the following equation:

$$\begin{aligned} \frac{H^{AE}(\omega)}{H^{PLB}(\omega)} &= \frac{S^{AE}(\omega)U(\omega)Y(\omega)R_X(\omega)E(\omega)P(\omega)A(\omega)B \prod R_C(\omega) \prod T_C(\omega)}{S^{PLB}(\omega)U(\omega)Y(\omega)R_X(\omega)E(\omega)P(\omega)A(\omega)B \prod R_C(\omega) \prod T_C(\omega)} \\ &= \frac{S^{AE}(\omega)}{S^{PLB}(\omega)} \end{aligned} \quad (2.11)$$

Two methods have been used to match the AE and PLB events; matching on time data and matching on location. This has been done because the accuracy of the locations calculated will be limited because the structure has not been considered in the location processing. Despite the information on this particular test being comprehensive, it is not sufficiently detailed to recreate the exact transducer positions on the 3D structure. Instead the same 2D processing will be used on both the AE and PLB datasets. A 2D location algorithm is what would currently be used at Airbus. The time matching will not contain this possible cause of inaccuracy.

Time matching

The information that will be used from the BALRUE output files is the time of the event, the time difference between the arrivals for a single event (referred to

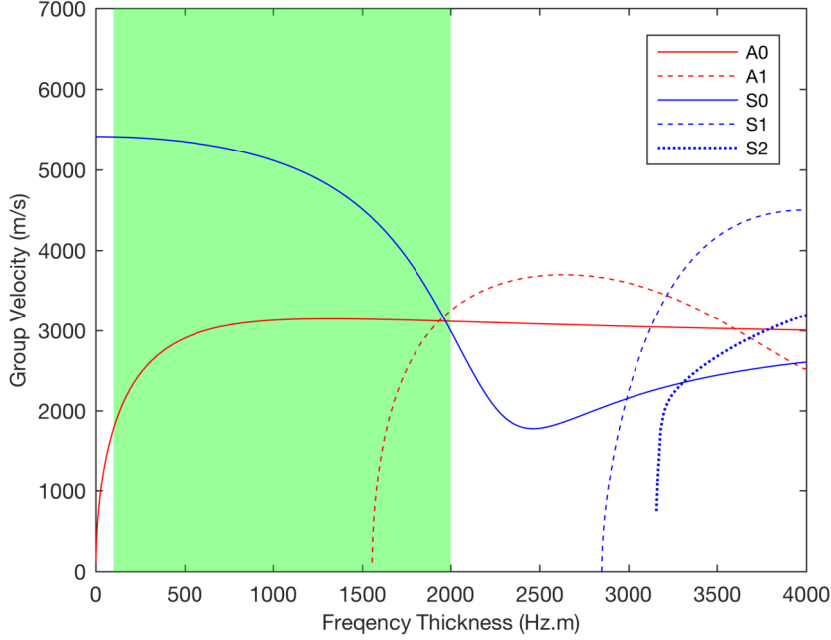


Figure 2.6: Group velocity dispersion curves for aluminium. The approximate frequency thickness region for the wing of an A340-600 is highlighted in green.

as the ΔT value) and the maximum amplitude received on each transducer. How these values are extracted from the received waveforms is shown in figure 1.2. The global event time has been recorded to monitor how the AE events from damage change over time. To match events the ΔT values of the PLBs at a known location are compared with the ΔT values from the AE events. Any events for which the first 3 triggered transducers have all ΔT values within 10% of the corresponding PLB ΔT values are defined as a match. As most events trigger more than 3 transducers it would be possible to match on more ΔT values.

Location matching

To match on location the position of each PLB and AE event has been calculated. This has been done using the Paget algorithm [36] and the Point Method [37]. The Paget algorithm is an analytical method to find the location using an elliptical assumption of velocity profile. This has been used because it is the standard location method used at Airbus for processing BALRUE data. The Point Method is a numerical search method which has been used because this has been found to be the most robust location algorithm. Locations with

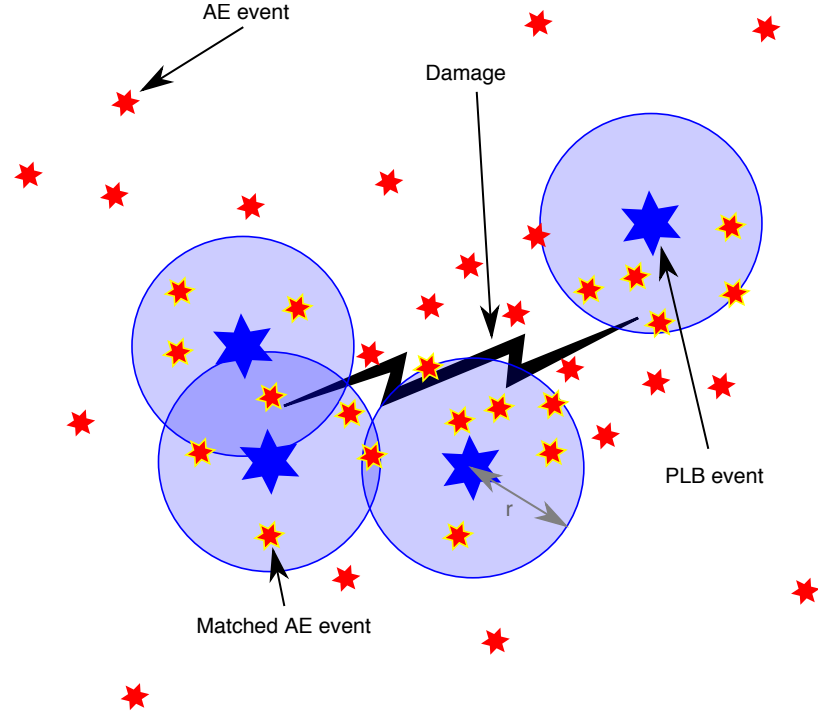


Figure 2.7: A diagram showing the location matching method.

the Point Method have been found using the algorithm with the first 3 and the first 4 hits and results will be shown for both. Using 4 hits is more restrictive and excludes both AE and PLB events that only trigger 3 transducers.

The velocity used for location is the group velocity experimentally measured at the time using a PLB as a source. The velocity was measured as 3000 m/s in the x direction and 3010 m/s in the y direction. When comparing to the dispersion curves for aluminium, which are shown in figure 2.6, it can be seen that this is most likely to be the A_0 mode. This means there is a potential alternative triggering mode because the S_0 mode is faster at these frequency thicknesses but, as shown in section 2.3.1, fatigue cracks in aluminium generate a S_0 source that is significantly lower in amplitude than A_0 . The S_0 mode is therefore unlikely to be the triggering mode and was not when measuring the velocities which is a procedure that occurs over relatively short distances.

The criteria to determine if an AE event matches a damage location is if the AE event is within 10 cm of a PLB associated with that damage location. This method is shown in figure 2.7.

Matching method		Time	Paget	Point Method	
				3 transducers	4 transducers
Number	matched	26 121 (2.89 %)	56 892 (6.30 %)	116 570 (12.90 %)	100 663 (11.14 %)
	unmatched	877 367 (97.11 %)	707 561 (78.31 %)	575 610 (63.71 %)	492 093 (54.47 %)
	outside	-	139 035	211 308	282 976
	search area		(15.39 %)	(23.39 %)	(31.32 %)
	insufficient	-	-	-	27 756
	hits				(3.07 %)

Table 2.8: Number and percentage of AE events matched to PLBs at damage for each technique.

Comparison of matching methods

The different matching methods will be compared so the results from the best can be used to analyse the data matched to each damage location. Table 2.8 shows how many AE events match for each method and, where appropriate, the reasons why some AE events have been excluded from the analysis. Time matching produces the least matches by quite a significant margin so appears to be the most restrictive. With the location methods it is possible for the algorithm to locate either AE or PLB events outside of the defined search area. This could be either because that AE event occurred in a part of the structure that was not in the monitored region or happens to have been located outside of the search region due to limitations of the location algorithms. The Point Method matches more AE events than Paget algorithm and, as expected, the version using information from 4 transducers is slightly more restrictive than that using 3 transducers. Just from this information it is difficult to pick which method is producing the best matching results. The method giving the most matches may not be producing accurate matches.

To attempt to determine which matching method is performing the best, matching for each damage location will now be analysed. The number of AE events matched for each damage location for each matching method is shown in figure 2.8. Generally the 3 methods using location match similar numbers of AE events to each damage type and the time matching displays a very different pattern. This is to be expected because, despite the different location algorithms, the 3 location methods are closely related but the time matching uses a completely different approach.

Again it is difficult to draw positive conclusions from these figures as to which method is producing the best basis for matching. Instead time matching will be excluded from further analysis because it is the least clearly deterministic. A 10 % change in ΔT value is a difficult value to visualise and varies with the

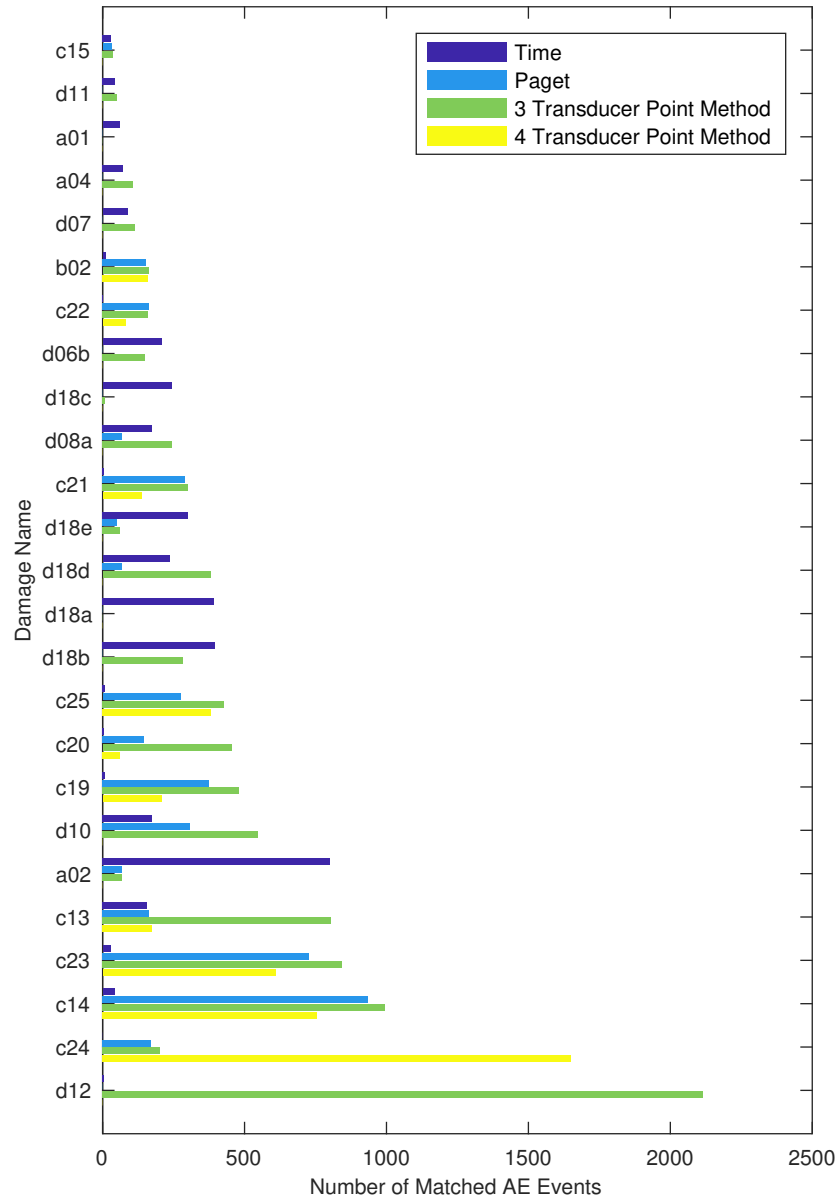


Figure 2.8: The number of AE events matched to each damage location for each matching technique. Events are ordered by maximum number of matches and this is part 1 of 2.

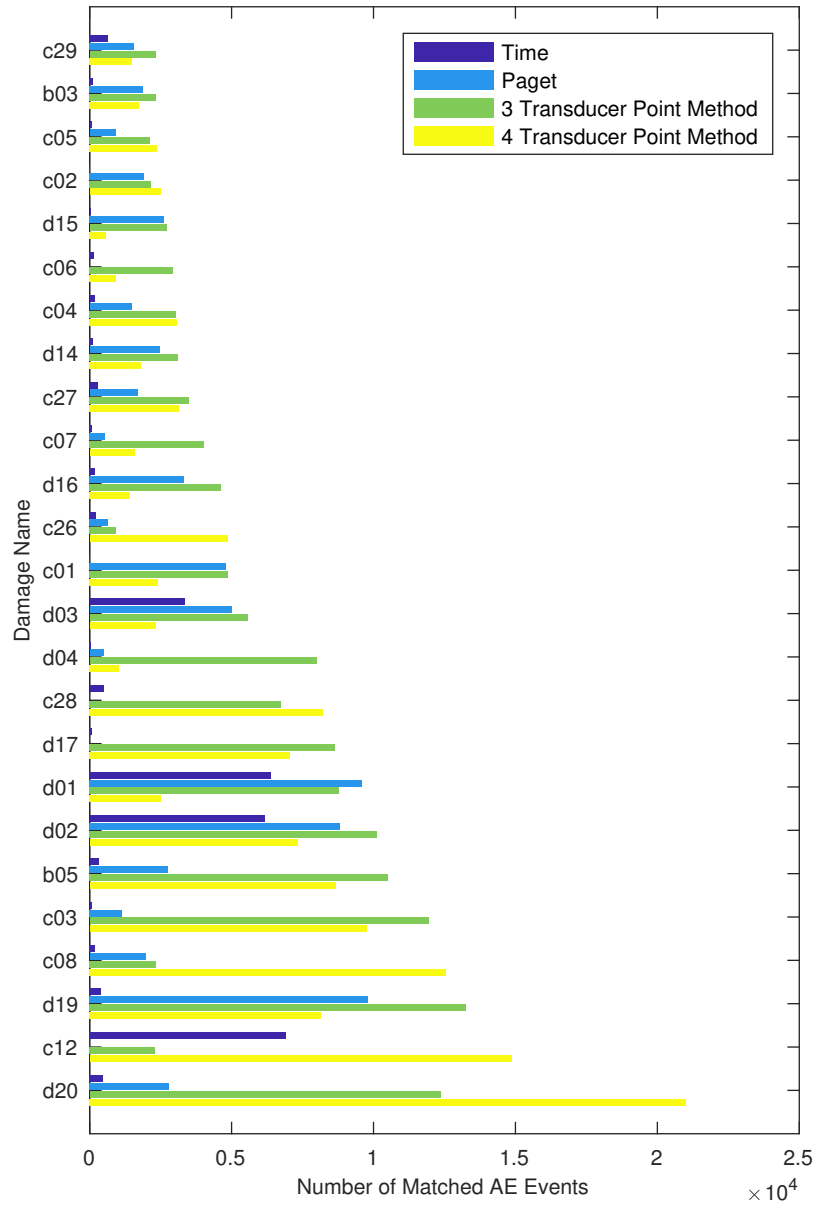


Figure 2.8: The number of AE events matched to each damage location for each matching technique. Events are ordered by maximum number of matches and this is part 2 of 2.

Matching method	Mean distance to centroid (m)
Paget	0.106
3 transducer Point Method	0.466
5 transducer Point Method	0.290

Table 2.9: Comparison of the mean PLB groupings across the different damage locations for each matching method.

position of the AE event. It is also conceivable to have AE events that the order of the first 3 arrivals will change if 2 or more arrival times are close to each other. This could mean that no match is made despite the ΔT values being within 10% of each other. There are limitations within the location methods as well. All location algorithms have inherent error and using 2D location algorithms on a 3D structure will introduce more errors as there are possible wave propagation paths that are not considered in the processing. Though the structure is normally 'unfolded' in the imaging to reduce this problem. Despite the limitations, the 2D Paget algorithm is what is used by Airbus in its AE processing leading to a certain confidence in the use of 2D location algorithms for this type of task. The location results will now be used to determine which location algorithm to use for matching.

Figure 2.9 shows the distribution of the AE locations across the entire monitored region when using the Paget algorithm. This plot agrees well with the location plots generated at the time of the test shown in [57] although the location plots here have been shown with a logarithmic colour scale to reduce the skew caused by a few points in space where there are very high number of AE events. The location plots for the different version of the Point Method are shown in figures 2.10 and 2.11. To determine which location algorithm provides the most accurate locations and therefore the best matching is not possible using the AE data as the true source location of the AE events is unknown. It is however known that the PLBs were performed at the damage locations and therefore close together. The most accurate location algorithm will therefore produce the tightest groupings of PLB events. To determine which of the methods this is, the distance between the PLB events and the centroid of the points, σ , has been found for each group of PLB that belong to a damage location. This was calculated using the following equation:

$$\sigma = \frac{\sum_{i=1}^n \sqrt{(x_i - x)^2 + (y_i - y)^2}}{n} \quad (2.12)$$

Where n is the number of PLBs that have been performed at the damage location and x and y are the positions of the centroid of the PLB locations, $[x_i, y_i]$.

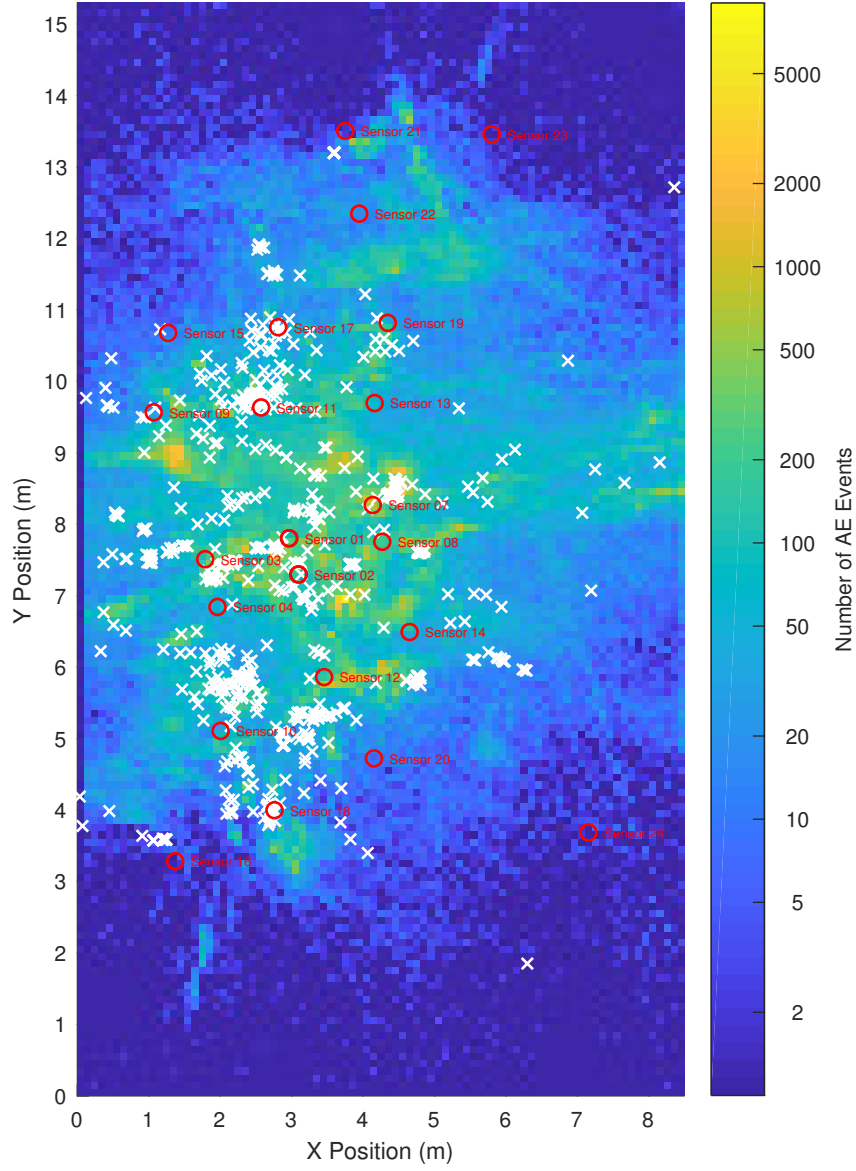


Figure 2.9: Location plot of the AE data for the A340-600 EF2 test using the Paget algorithm. White crosses show the location of validation PLB events. Red circles show transducer positions.

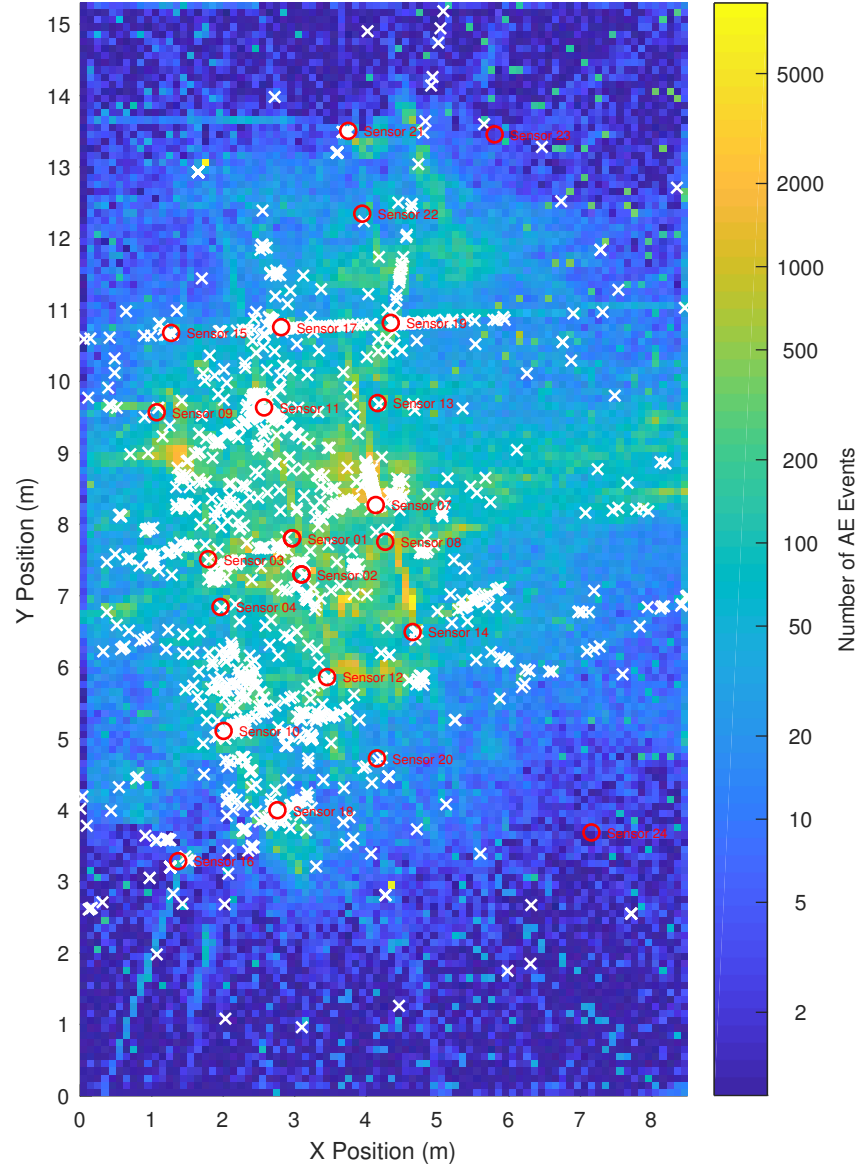


Figure 2.10: Location plot of the AE data for the A340-600 EF2 test using the point method with the first 3 hit transducers. White crosses show the location of validation PLB events. Red circles show transducer positions.

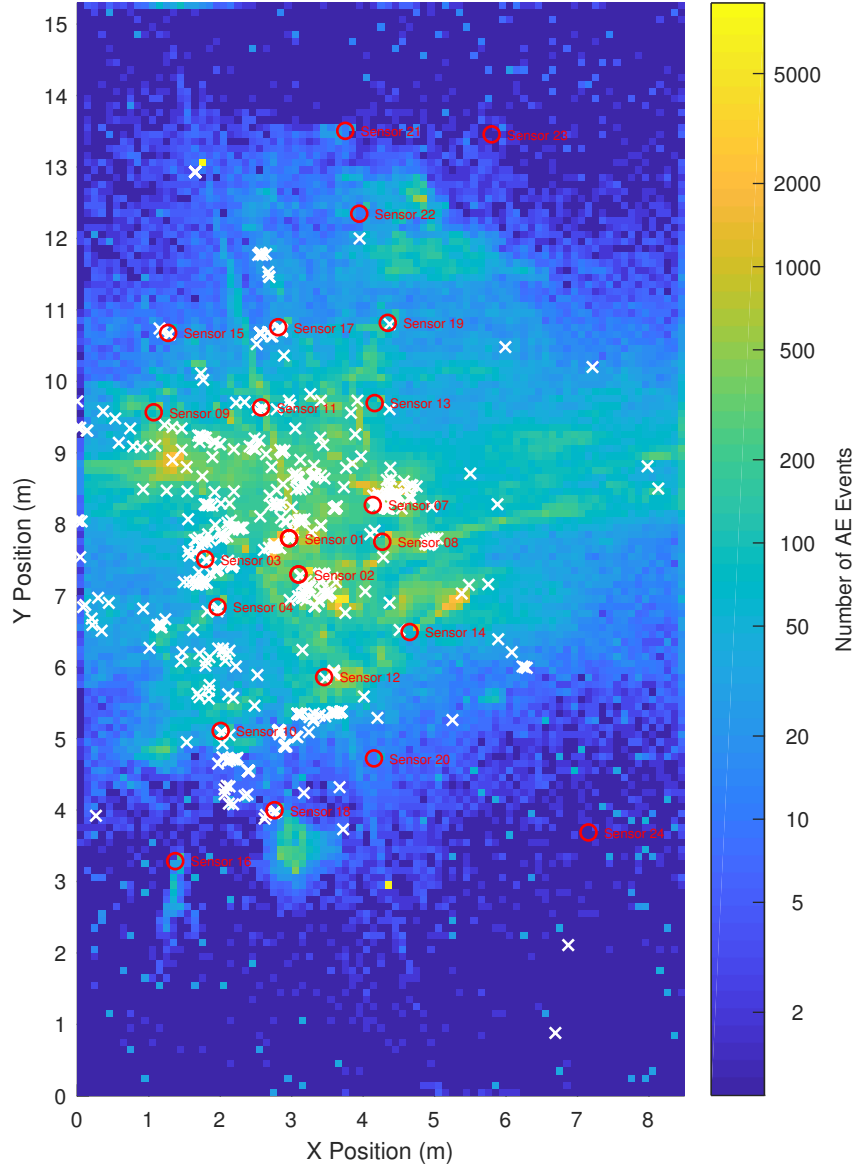


Figure 2.11: Location plot of the AE data for the A340-600 EF2 test using the point method with the first 4 hit transducers. White crosses show the location of validation PLB events. Red circles show transducer positions.

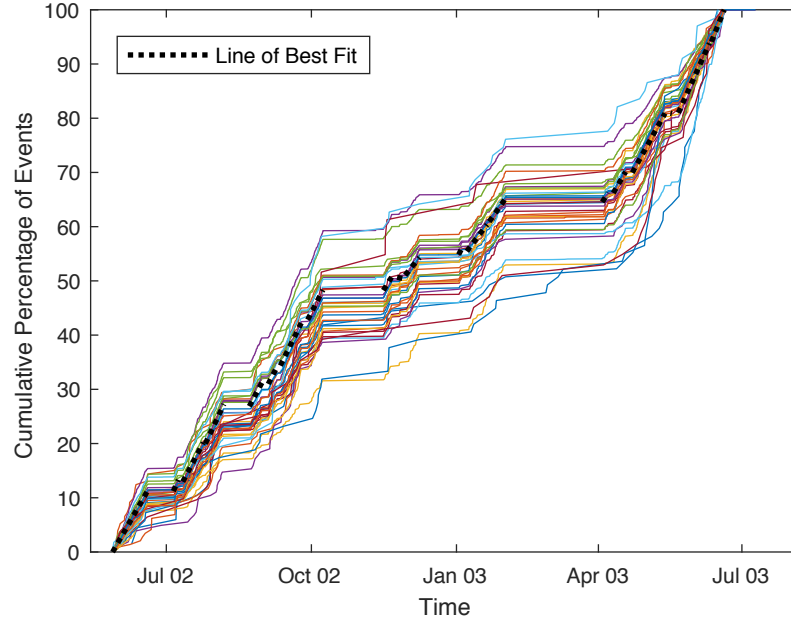


Figure 2.12: The cumulative rate of occurrence of AE events across the testing period for the A340-600 EF2 test.

This is calculated by:

$$\{x, y\} = \frac{\sum_{i=1}^n \{x_i, y_i\}}{n} \quad (2.13)$$

Table 2.9 shows the mean distance to the centroid for all damage locations for each of the matching methods. The method that produces the lowest value is the Paget location method. This matching method will therefore be used for the results shown later in this chapter.

2.4.2 Comments on the dataset

There are a few facets of the A340-600 EF2 dataset which should be considered further and have implications on the conclusions of this section. These are the rate of the AE events throughout the test and the AE events likely removed by the phenomenological filter applied by the BALRUE system.

Rate of acoustic emissions events throughout the test

The loading applied to the A340-600 airframe during this test was many simulated flights. The aim of this is to take an airframe to many more flight cycles than it was designed for to see what fatigue damage occurs. This is to validate modelling and life predictions and develop maintenance strategies for the air-

craft. The exact loading is not known by the author but, apart from clear test downtime, it can be assumed that similar loads are being applied repeatedly over the duration of the test. The rate of occurrence of AE events across the test has been found for each of the 50 damage locations and is shown in figure 2.12. Each damage location generates a different total number of AE events so each damage location is normalised by the total number of AE events and a cumulative percentage is shown. This enables the behaviour of different damage locations to be more easily compared. Where the gap between AE events is greater than 1 d then test downtime has been assumed and this has been used to delineate different groups of AE events for fitting of a line of best fit. The line of best fit has been found by fitting a 1st order polynomial using the least-squares method to each group. If there were less than 100 AE events in the group then this group was ignored.

It can be seen in figure 2.12 that for all of the damage locations, the first AE event occurs close to the start of the test period and they continue to be detected until the end of the test period. This suggests all of the damage was either pre-existing in the structure or created as the test initiated. If any new damage occurred during the test, it did not start to generate AE events from a new source that were recorded by the system. This could conceivably be correct because the airframe is designed to be resilient under these loading conditions and fatigue damage initiates from an existing defect in the structure. Given the structure is not in the real world, it does not have the opportunity to develop new small defects via incidents such as small scale collisions with debris or exposure to corrosive substances. Damage initiation sites are therefore most likely to be created during manufacture. Despite this, it is a somewhat surprising result that no damage initiates later.

The rate of AE events is not clearly shown in this figure due to displaying the y-axis as a cumulative percentage but it can be seen that the rates of occurrence of AE remain approximately constant across the whole test period. The line of best fit does not change significantly in gradient across the test. It would perhaps have been expected that the rate of occurrence of AE events would increase as the fatigue damage in the structure increased. This has not occurred but this could again be due to the structure being resilient under these loading conditions and that any gross damage would have been repaired during the test. Examples of fatigue tests on aluminium samples in [58, 59, 60] all show periods where the AE count rate was constant. The count rate increased exponentially when close to failure in some of these examples. However the A340-600 airframe will not have reached this point in this test. It should be noted that it is difficult to compare the rate of occurrence of AE because it is dependant on system setup and settings, most notably the triggering threshold value, which are different

between different experiments. This is highlighted by [61].

Both of these facets of the dataset raise questions about the dataset; did all of the AE emitting damage initiate at the beginning of the test and is it reasonable that the rate of AE remains relatively constant for all of the different damages? Given the time that has passed since this test it is difficult to answer these questions conclusively. That no AE source initiated at a point later in the test is questionable but a reasonable explanation does seem to exist for the approximately constant AE count rate. Alternatively the system could be recording AE events that do not correspond to the expected damage but are generated by a more constant acoustic source. Given the relatively low percentages of matches for any of the matching techniques, many other acoustic sources are present in the structure, so this is a possibility. These questions should be considered when drawing conclusions from this dataset and would warrant further investigation if a test like this were to occur again.

Estimating acoustic emission events missing from the dataset

This dataset was recorded using a BALRUE system which is described in section 1.6. The system will discard events if they do not pass certain criteria, most significantly the detection threshold and the thresholds set by the phenomenological filter. The setup procedure is to set the detection threshold 6 dB above the noise level. In this test, the detection threshold was set to 40 dB suggesting the noise level was 34 dB. The aim of the phenomenological filters are to remove AE events which do not fit an expected profile. The expected profile is that the signal received by the first transducer will be the largest in amplitude and the following received signals on later triggered transducers will be smaller. This filter aims to remove spurious acoustic signals, for example later reflected signals or signals from different AE sources that arrive coincidentally. The phenomenological filters were set to 60, 50 and 45 dB for the 1st, 2nd and 3rd triggered transducers, which are more restrictive thresholds than the detection threshold, so these will determine which events are not recorded in the dataset. Note that the 1st, 2nd and 3rd triggered transducers may differ between different AE events for the same damage location. What has been removed from the dataset will affect the amplitude statistics which will influence the comparison with the literature. In this section an estimate of what has not been recorded in the dataset has been attempted.

Figure 2.13 shows the amplitude distribution for 1st, 2nd and 3rd hit transducers for all of the AE events that have been matched to one of the damage locations. Figure 2.14 shows examples of the amplitude distributions for the events matched to different randomly selected damage locations. Note that in

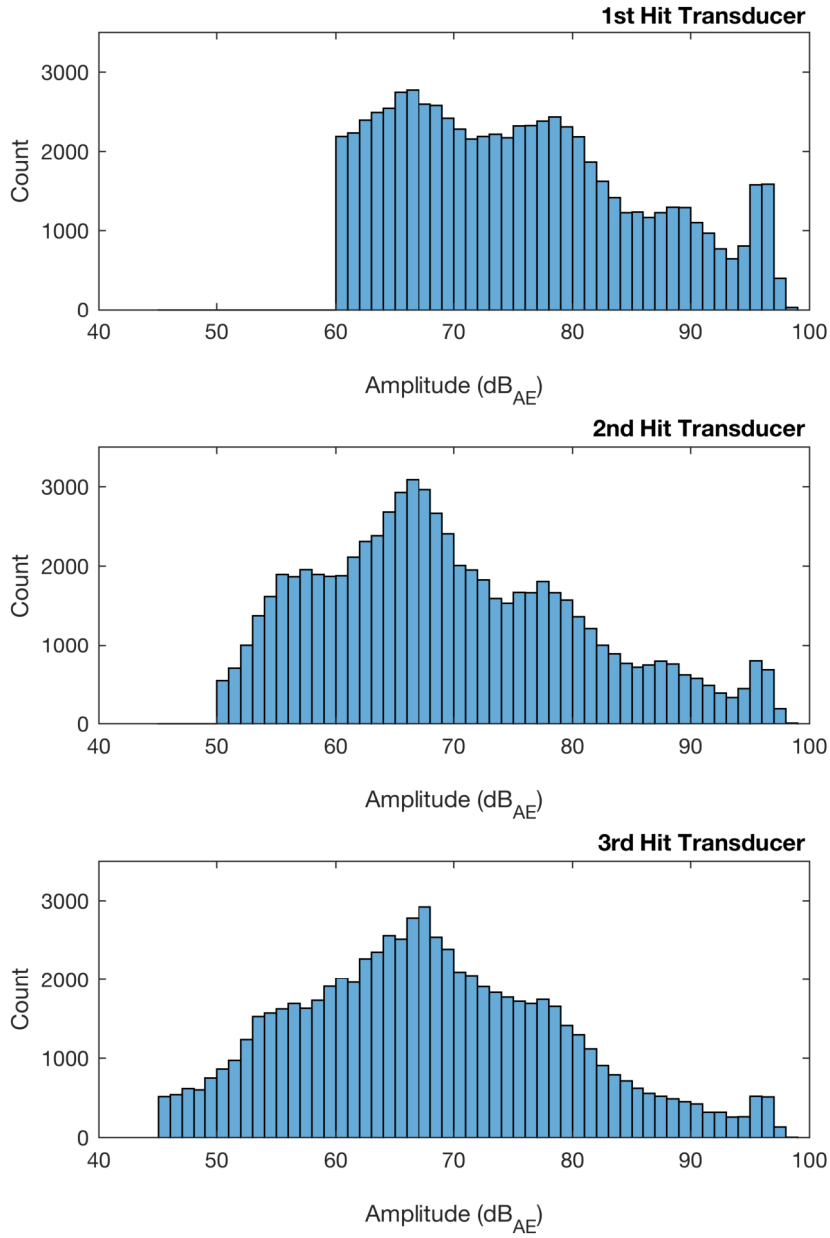
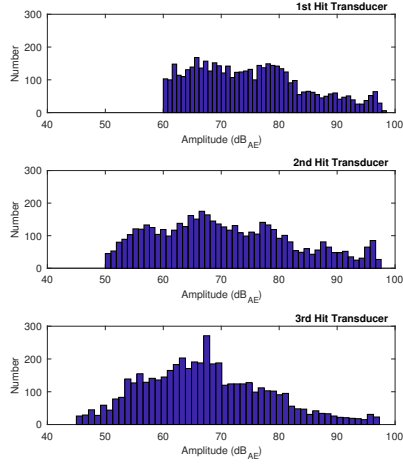
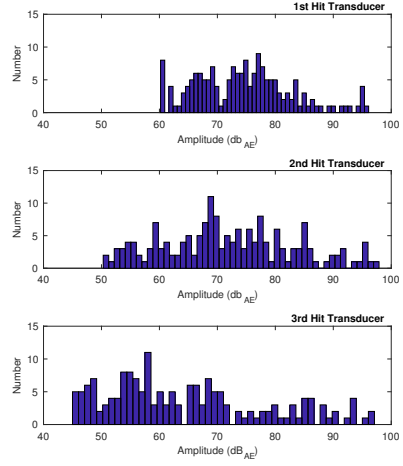


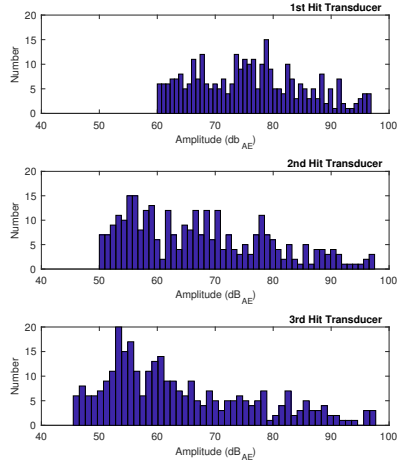
Figure 2.13: The amplitude distribution for the 1st to 3rd triggered transducers for all of the AE events collected during the A340-600 EF2 test that can be matched to identified damage locations.



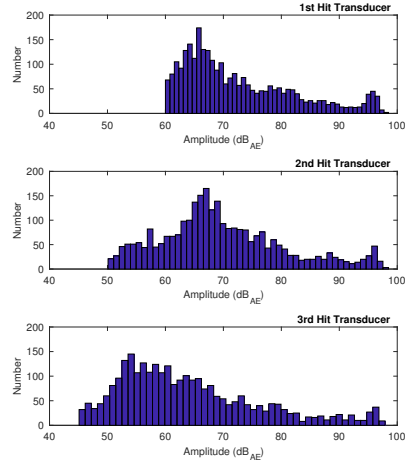
(a) Damage location C01



(b) Damage location C24



(c) Damage location D10



(d) Damage location D20

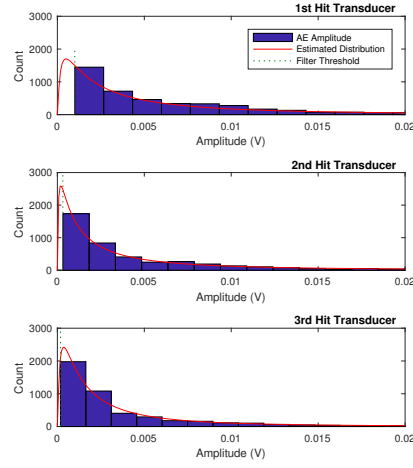
Figure 2.14: Example amplitude distributions for different damage locations in the A340-600 EF2 test.

the plots in these figures, the amplitude is shown in decibels where the reference amplitude is 0.001 mV. The cut off amplitudes for the different hit order transducers can be clearly seen in all of these histograms. The distribution of data suggests that these thresholds are removing a proportion of the AE events because the cut off causes an abrupt drop in the count. To make an estimate as to the AE events which have not been recorded, a truncated lognormal distribution has been fitted to the amplitude data for each hit transducer at each damage location. The fitting process was a maximum likelihood estimate. A truncated distribution can be fitted to data where it is known that a region of the distribution has not been recorded. In this case it is known the recorded data will be truncated below the amplitudes of the phenomenological filter. The lognormal distribution was chosen because when the whole dataset is plotted on a logarithmic scale, it appears approximately like an off centre normal distribution. As can be seen in figure 2.14, the lognormal distribution will not perfectly fit the amplitude distributions at the damage locations with a small number of events. It will still provide a method of approximating the AE events missing from the dataset.

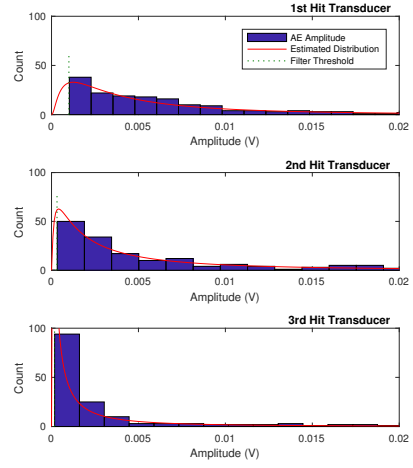
Once the truncated distribution has been fitted, the full distribution can be used to estimate the AE events missing from the dataset. Examples of the estimated distribution are shown in figure 2.15. Note that these are shown on a voltage scale where the calculation is performed. The estimated number of AE events missing from the dataset are found by finding the area under the estimated distribution curve to the left of the phenomenological filter threshold for each triggered transducer. When divided by the histogram bin width, this gives the number of events in this region. The mean value of missing events over the 3 first triggered transducers is used as the final value and these are listed for each damage location in appendix A. It can be seen that the number of missing events is relatively small with a mean of 10 % of the matched events across the damage locations. These estimated missing low amplitude events will be added into the dataset for the rest of the analysis on the A340-600 EF2 test.

2.4.3 Obtaining an estimate of amplitude from the Airbus dataset

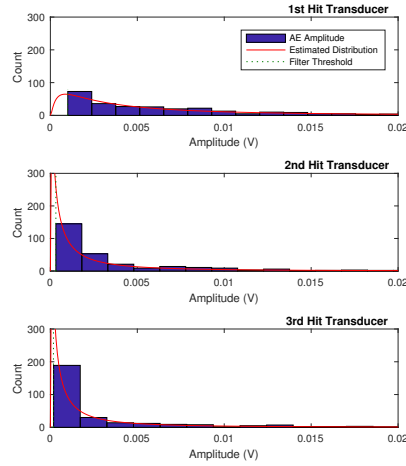
With the matching method based upon the Paget location algorithm applied and the number of missing events estimated, the amplitude data from the A340-600 EF2 test can be analysed. A random example of the amplitude of the matched signals for 1 damage location is shown in figure 2.16. This shows how the AE events are distributed over the whole time of the test and their amplitude for damage location C05. The 8 PLB events at this damage location matched with



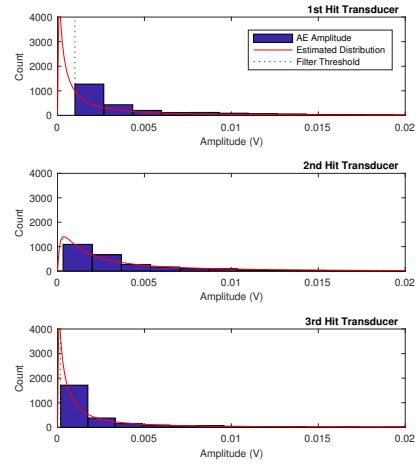
(a) Damage location C01



(b) Damage location C24



(c) Damage location D10



(d) Damage location D20

Figure 2.15: Example amplitude distributions for different damage locations in the A340-600 EF2 test and the estimated distribution of events.

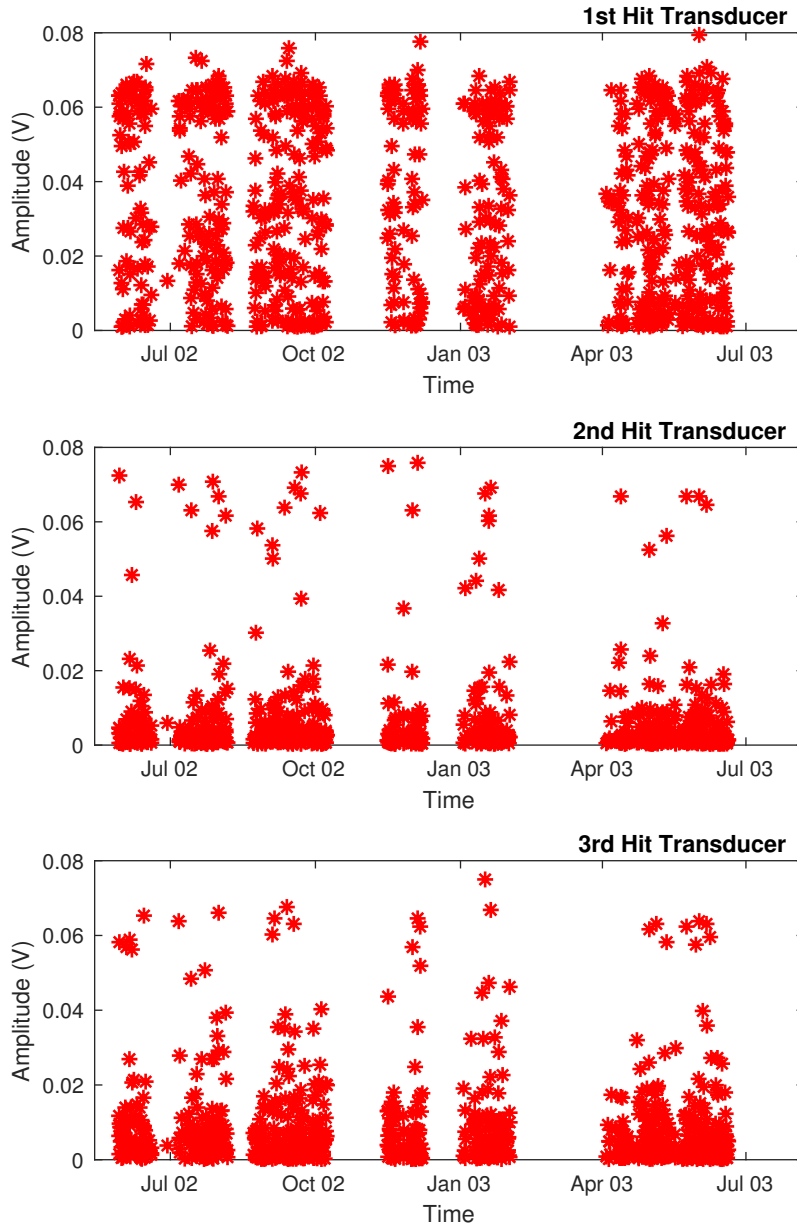


Figure 2.16: Scatter plots for the first 3 triggered transducers showing the amplitude and distribution in time of AE events for damage C05 over the whole test.

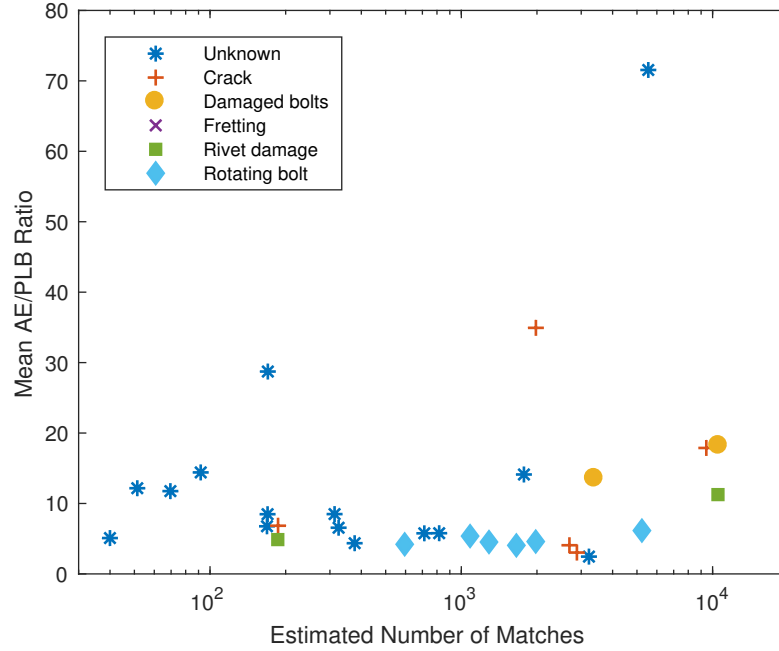


Figure 2.17: A scatter plot showing the number of matches and the AE to PLB ratio for each damage location. The type of damage is also shown where known.

906 AE events. The large gaps where no AE events were recorded are periods of time when the structure was not under fatigue during test downtime and are consistent across the whole dataset. The constant distribution of events over the test period are typical of this dataset, as shown in figure 2.12.

This procedure has been performed at all of the damage locations. To draw a more general conclusions from the dataset, mean values for each damage location across all of the 3 first hit transducers have been calculated. To remove the effects of the structure and recording equipment the AE to PLB ratio will be analysed rather than the recorded voltages. A table summarising these calculations for all of the damage locations is shown in appendix A.

Figure 2.17 shows the mean AE to PLB ratio for the first 3 triggered transducers and the estimated number of matches for each damage location. The estimated number of matches is a sum of the AE events matched to that damage location and those predicted to have been cut off by the phenomenological filter. It can be seen that there is a large range in both parameters. This is to be expected because the damages vary in size and severity. The minimum AE to PLB ratio from this dataset is 2.01, the maximum is 71.55 and the mean is 10.92. This is the mean calculated over the damage locations and does not consider the number matches for each damage location. These values of AE to

PLB are generally much larger than those calculated in section 2.3.1 for both modes.

Figure 2.17 also shows the types of damage, where it has been possible to identify the type. Generally there is no grouping of damage types by either AE to PLB ratio or number of matches. The possible exception to this is the rotating bolts which have produced relatively low values of AE to PLB ratio. The literature search focused on crack damage as an AE source because it was assumed this would be the most prominent damage mechanism. When looking at the damage locations identified solely as cracks there is a similar scatter to the whole dataset with the mean AE to PLB ratio of these points being 9.69. It is likely that cracking is a damage mechanism in some of the other damage types.

2.5 Conclusions

In this chapter work has been conducted to define a reasonable estimate of a model for AE sources in aluminium aircraft structure. This has proved difficult. From the literature, an estimate of the amplitude of excitation produced by a fatigue crack in a thin aluminium plate has been obtained. Numerous assumptions had to be made to calculate this in absolute displacement at the source. The displacement created by a PLB has also been found enabling the ratio between maximum amplitude of AE and PLB events to be found for this damage type.

A dataset from a large scale and long term Airbus structural test has also been analysed and from this AE to PLB ratios were found for 50 different damage locations. At the large majority of damage locations, the AE to PLB ratios were larger, often significantly larger, than the median value calculated from the literature. This suggests two possibilities; that the amplitude of AE events detected in this type of test is higher than both the literature suggests and the amplitude of a PLB or that the majority of the AE events detected in this test were not generated via the expected damage mechanism and instead another that produces significantly higher amplitudes. Given the time that has passed since the test and despite the large amount of information available on this particular test, the author does not believe it is possible to determine which of these statement is the correct one for this test. This is an area where further work is required by both Airbus and the wider AE community if a more quantitative assessment of AE results is to be obtained. This is likely a necessary step for the techniques wider adoption and most certainly for the technique's qualification. The analysis comparing to repeatable PLBs demonstrates the value in having a repeatable source which can be performed at known damage

locations. This is a possible route for more detailed analyses of AE events from real tests.

The model of an AE source that will be used in this work is that described in section 2.3.1. Despite the comments above, the results from the Airbus A340-600 EF2 test suggest this is a reasonable conservative model to use in models of this type of test as it is of the lower range of amplitude.

Chapter 3

Guided Wave Propagation Across Features

The component of the overall AE system model that will now be focused on is the propagation of guided waves through the structure. A common limitation of industrial GWSHM is a failure to account for the effect of wave propagation within the monitored structure and how this affects system performance. The main focus here is on AE testing but much of what is presented is relevant to active GWSHM as well. Dispersion and reflections from features quickly cause the waves to attenuate and become more complex. This limits the range at which AE events can be detected and causes the received signals to vary significantly for the same event detected on different transducers. This can have a significant effect on the performance of an AE system. These limitations have been highlighted before by authors including Hamstad [62] and Scholey [44] but, in the authors experience, the effect of wave propagation on the performance of AE systems is not directly considered in the systems being developed in industry in 2017. This is most probably due to the rapid scaling in complexity of wave propagation with multiple structural features and that Finite Element (FE) modelling for any real sized specimen is currently computationally impractical. A modern highly optimised metallic aircraft wing skin for example contains many holes, thickness changes and stringers with a pitch between features at the order of 15 cm. The same applies to composite structures. Not considering the effect of wave propagation where there are features present is a factor limiting the wider scale use of AE systems in industry.

First in this chapter relevant work on wave propagation in plate like structures is discussed. Then an empirical modelling approach is explained followed by description of experimental measurements on different features; a bonded

box section, a row of holes and a bolted L-section. The empirical models created from the data collected in the experiments are then described and these are tested in the following chapter. Finally there is a discussion on the time delay on the propagating waves as they cross features.

3.1 Modelling of guided wave propagation across features in the literature

The propagation of ultrasonic guided waves across different aerospace structural features and in more complex structures has been considered in the literature. This section will summarise a selection of this work relevant to the modelling approach used in this thesis. First models of guided wave propagation across individual features will be discussed. There are many possible features in aerospace structures and defining a comprehensive list is a challenge in itself as shown by [63]. Out of the selection here, it would be possible to use some of these feature models as a component in the modelling framework. Many of these models have been created with respect to using guided waves for direct inspection of bondlines because this is a problem which is difficult to assess with traditional NDT methods. This does not exclude them from use in this work as they predict transmission values which can also be used for modelling guided waves for any application. After the discussion of single features, there is a summary of work conducted on specimens containing multiple types of feature or segments of real structures. Less work has been conducted on these complex structures.

A common and simple feature found in aircraft is a thickness change in a plate. This is often done to remove weight. It is clear that the two different thickness's will have different dispersion curves but the feature will also affect the wave propagation by scattering the wave. Pagneux and Maurel [64] present an analytical model for smoothly varying thickness change in a plate. This technique is probably more suited to modelling uneven features such as corrosion patches than milled thinning of plates with more abrupt edges. Cho [65] models thickness changes between 1 and 2 mm plates numerically using a hybrid boundary element method and validates some of the results experimentally. Most of the results presented are in the frequency range of 0.2 to 1.2 MHz. At the lower end of this frequency range there is a high value of transmission of the incident mode in all cases and the modelling shows the reflections and mode conversions where some of the energy is lost.

Another feature commonly studied in the literature is the adhesively bonded lap joint. Methods to model this situation include analytical [66, 67] and finite

element [68] techniques. All of these approaches are successfully validated with experimental results. The similar case of plate overlap, where an adhesive layer is not considered, is modelled using a hybrid boundary element technique by Song *et al.* [69] where transmission coefficients and mode conversion are found and validated. In each of these papers it can be shown that there is a frequency range and mode that has a high level of transmission across the feature. However the exact parameters to achieve this depend on factors including the geometry of the lap joint, the adhesive type, the relative success of the adhesive cure and the plate thickness. To get the highest value of transmission coefficient requires, at a minimum, tuning the frequency of the incident wave.

The comprehensive studies by Dalton *et al.* in [70, 71] discuss guided wave propagation across multiple different types of feature present in aircraft structure. These features include a stringer joint, skin covered in sealant, double skin, tapered skin and a lap joint. They consider the application of both active GWSHM and AE systems. The FE and experimentally measured transmission coefficients show the challenges of achieving sufficient levels of transmission across multiple of these features for a sparse array of transducers to provide monitoring. This is because there is no consistent mode or frequency found which will propagate across multiple features whilst maintaining sufficient amplitude. The exception to this are the results in [71] considering AE and show high percentages of transmission for guided waves at frequencies lower than 100 kHz for both fundamental modes. This is a lower frequency range than will be used in the investigations in this work but not significantly lower.

The above examples show that for an individual feature it is likely that a technique to determine the guided wave propagation across it exists. Therefore for a single feature it will be possible to determine a frequency and mode of operation that would enable monitoring to successfully occur. However the different frequency ranges for high levels of transmission reported by the literature and particularly the work by Dalton *et al.* show, that when multiple different features are present, it can be very difficult to find a frequency of operation to successfully conduct monitoring. Despite this there is some work which demonstrates GWSHM on more complex structures.

An example of successful detection of a defect on a moderately complex structure is shown in [72]. This uses an active GWSHM system. A composite plate with two stringers is monitored and, by considering the interaction of the stringers, arrivals from a delamination are identified. The transducer density however is sufficiently high that the effect of only one stringer needs to be considered. Ideally operation across multiple stringers or features would be possible. It also uses some signal processing which may not translate to an AE system.

Modelling of complex structures has been achieved numerically. Agostini *et al.* use the Local Interaction Simulation Approach (LISA) [73] to model guided wave propagation within a Y junction stringer. The LISA is a type of numerical modelling where the structure is split into discrete segments which are modelled separately. The interactions between each segment are passed between models. The technique is validated experimentally for simpler structures within the paper but not for the Y junction. This reveals another challenge on complex structures; that it is more difficult to determine that model results are correct. Di Scalea *et al.* use the semi-analytical finite element approach to model the dispersion curves for the skin-to-spar joint bond on a unmanned aerial vehicle. This is used to inform the mode choice for a SHM system. The FE method is used by Olson *et al.* [74] to model a region of a fuselage structure and the output of the model is compared to measurements taken with a scanning laser Doppler vibrometer. The limitation with this approach is that the modelled area must be small so that a FE model can be successfully evaluated. Therefore only a section of the fuselage is considered.

For practical application of GWSHM systems on aircraft it would be useful to have a method of determining the system's performance on structures of varying complexity with multiple features. The literature described here highlights the need to understand how frequency and mode of operation can effect transmission when a structure contains different features. Modelling of GWSHM systems could be used both in system design; to inform transducer placement, transducer selection, mode selection and operating frequency. The above paragraph gives examples where guided wave propagation has been modelled successfully on complex structures but in all cases the area of coverage is small. The target application structures are much larger than any modelling examples found in the literature. Work by Flynn *et al.* [75] shows that a significant improvement in detection can be achieved with a very simple model of a stringer. The promising results here form the basis of the modelling work in this thesis. By using simple models of features it is hoped that useful information can be obtained about the operation of an AE system over a larger area of a structure. This will be done without too much computational or experimental expenditure which would be prohibitive for the use of these techniques in industry.

3.2 Experimental measurement of transmission across features typical of aircraft structure

The previous section shows examples of models of features in aerospace structures and techniques of how to obtain them. In many cases this modelling is

quite complex and could require significant effort and expertise to repeat for new features. It is also likely that some experimental work would be required to validate any new modelling. The philosophy behind the modelling approach for features in this thesis is to keep the modelling effort low because the level of accuracy generated by these models may be more than is needed to get useful predictions of AE system performance. Therefore this section will experimentally measure transmission across different features and build empirical models from these results. The reduction in effort here assumes more complex feature models would require experimental validation so this step would have to be performed anyway.

A key additional facet of the empirical models developed here is that all models aim to be conservative in their prediction of amplitude. One of the key uses of the overall system model is to predict where it is possible to detect AE events. It is important that this range is predicted conservatively because AE systems may be used in a safety critical environment. It is therefore preferable to not guarantee detection of an AE event when it is actually in range than inspire false confidence in the system performance. The crucial parameter in detection in threshold crossing AE systems is signal amplitude and therefore this parameter should be predicted conservatively. Therefore the empirical transmission models developed here will be designed to under predict amplitude in preference to over predicting it.

To demonstrate this approach, the transmission across different stiffening features will be measured. These features will be a bonded box section and a bolted L-section. During the assembly of the bolted L-section the opportunity will be taken to measure the transmission across a row of holes. These results will be used to build more general empirical models of these features which can then be tested against other experimental measurements.

3.2.1 Transmission across a box section

The first feature to be measured is a box section stiffener. There were pre-existing structures at the University of Bristol that could be used and they were used to test the concept of generating the empirical models. Before describing this work it should be noted that it was conducted before the work in chapter 2. Therefore the importance of measuring both the fundamental modes had not yet been understood and only the S_0 mode was measured.

Experimental setup

The structure on which the transmission was measured was a 3 mm thick aluminium plate with one bonded box section stiffener. A plan view of the plate

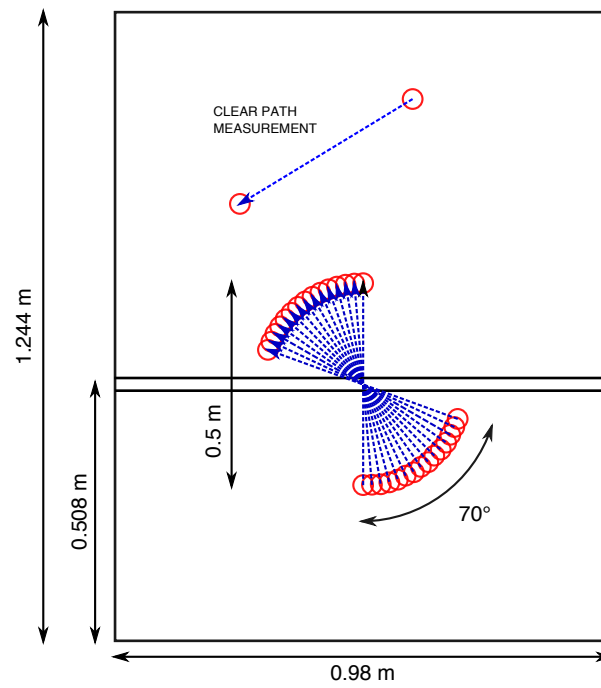


Figure 3.1: A plan view of the bonded box section transmission experiment. Transducers are red circles and measured ray paths are blue dotted arrows.

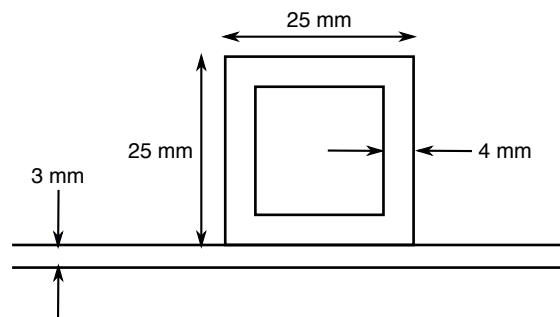


Figure 3.2: The cross section of the bonded box section.

with the dimensions is shown in figure 3.1. The stiffener was a 25 mm wide box section bonded to the plate using FM300 epoxy adhesive film. The cross section of the box section is shown in figure 3.2.

The transmission across the stringer was measured using a pair of roving EMATs. These EMATs were constructed in house at the University of Bristol. They have a centre frequency of 190 kHz and predominantly excite the S_0 mode. For this experiment, the transducers were excited at 190 kHz with a 5 cycle Hanning windowed tone burst. The EMATs were rotated around the centre point of the stringer at 5° increments from 0 to 70° angles of incidence. The spacing between the EMATs was 40 cm and this was kept constant at all incident angles. The collection at each angle was repeated 5 times including transducer repositioning and for each collection the signal was averaged 100 times to improve the SNR. The clear path collection was measured in a section of the plate not near the box section or any edges. 5 repeated collections were measured at this position.

Measurement of transmission coefficient

Example collected signals are shown in figure 3.3. In this diagram the predicted arrival times for the direct path, the first reflected signals and the direct path mode conversion are shown for the fundamental modes. The arrival times were calculated by forward propagating the input signal the respective distances for each of these ray paths. This is the same method as shown in [44]. It can be seen that in all cases the first arrival signal is about twice the length in time to what is expected or seen in the clear path signal. This suggests there is either significant mode conversion or reverberation in the box section leading to the signal being extended in time. For incident angles less than 30° the mode conversion or reverberation is larger in amplitude than the first S_0 arrival. As expected, the amplitude of the first A_0 arrival is small and overlaps with the first S_0 arrival in the clear path collection. This makes it impossible to find the A_0 transmission coefficient with these experimental results.

The collections at each angle are paired with a clear path collection to calculate the transmission coefficient. The transmission coefficient, T , was calculated by the following equation:

$$T = \frac{A_F}{A_C} \quad (3.1)$$

Where A_F and A_C are the maximum amplitudes of the envelope of the feature path signal and clear path signal respectively. This is measured within the expected time period for the first arrival for the relevant mode. This region of the signal is highlighted by the colouring in figure 3.3.

The experimentally measured transmission coefficient is shown in figure 3.4.

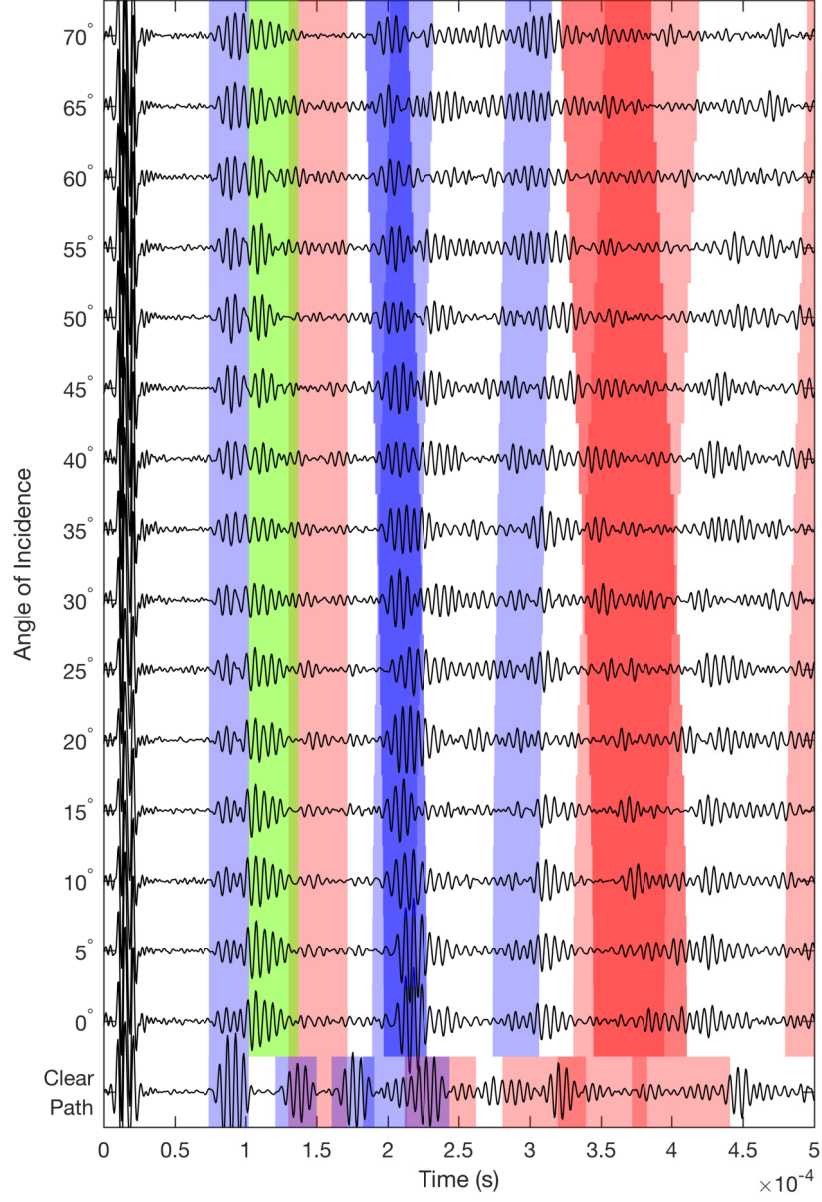


Figure 3.3: Example 190 kHz collected signals from the box section transmission experiment. The theoretical arrival times for the first arrival and subsequent first reflections for each mode are highlighted by the coloured shading; blue for the S_0 mode, red for the A_0 mode and green for the direct path mode conversion to the alternative fundamental mode.

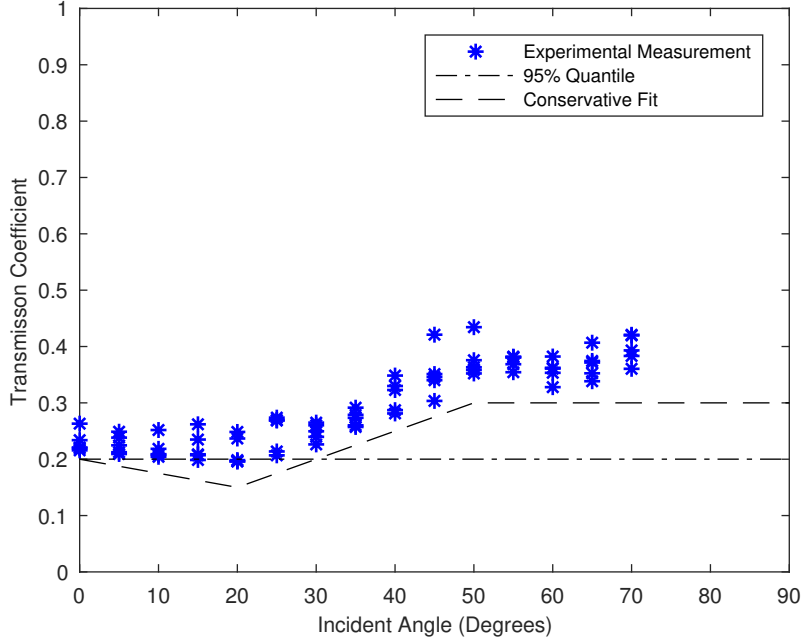


Figure 3.4: The transmission coefficient across a bonded box section for 190 kHz.

Each point in the graph represents the transmission measured from a pair of clear path and feature path signals. It can be seen that the transmission coefficient is at a value of about 0.2 from 0 to 30° then increases to a value of about 0.35 by 50° and stays at that level until the measurements finish at 70°. The scatter between the 5 measurements is approximately 0.1 but larger at a few angles of incidence. The cause of this scatter is likely the noise in the collected signals. By further inspection of the signals, shown in figure 3.3, it can be seen that the reverberation or mode conversion is of larger or equal amplitude to the S_0 arrival. It is larger for smaller incident angles. This is a significant energy loss for the first arrival but could potentially mean a greater range of detection than first assumed for signals crossing this feature. However this will not be included in the modelling because the higher amplitude signal would be arriving at a point in time later than expected. This would have a significant detrimental effect on the performance of location algorithms.

3.2.2 Transmission across a row of holes and a bolted L-section

The next feature studied is a bolted L-section. The opportunity will also be taken to measure the transmission across a row of holes. Features either like or

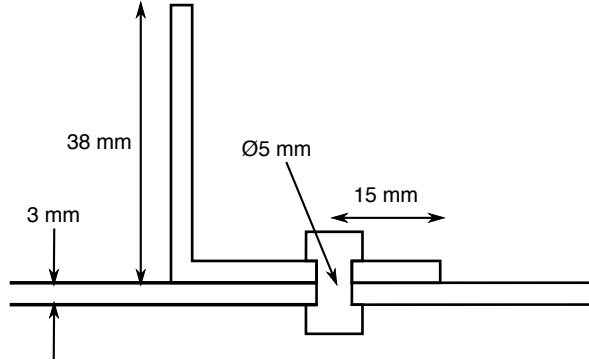


Figure 3.5: The cross section of the bolted L-section.

similar in shape to a L-section are common in aircraft structure as stiffeners and are therefore a relevant feature to model. The transmission across a smaller L-section of 25 mm in width and height is measured in [76] and is approximately 0.8 for the measured incident angles of 0 to 45°. A larger range of incident angles will be measured here for a larger feature. Changes from the previous experimental procedure used for the box section were made to improve the SNR of the signals, which should reduce scatter in the transmission coefficient, and enable the A_0 mode transmission coefficient to be measured. These changes were a modification of the transducer type and measuring the clear path signal in place rather than at another location respectively. These changes are explained in more detail below.

Experimental setup

A 3 mm thick aluminium L-section was attached to a 3 mm aluminium plate. The plate was 1 m wide and 1.5 m tall. The L-section was 38 mm in width and height and spanned the width of the plate. It was attached to the plate with 5 mm diameter bolts which had a 25 mm spacing between them. The bolts were tightened to a torque of 5 N m. The cross section of this structure is shown in figure 3.5.

12 Lead Zirconate Titanate (PZT) disk transducers were bonded to the plate in an arc. The transducers were 20 mm in diameter and 1 mm thick. The transducers were bonded with epoxy resin and were held in place by a vacuum bag during bonding. The spacing between the transducers was 40 cm and the transducers were arranged in 2 arcs either side of the L-section, centred in the middle of the L-section which corresponded to a position of a bolt. The angular spacing between the transducers was 15°. The layout of the transducers is shown in figure 3.6.

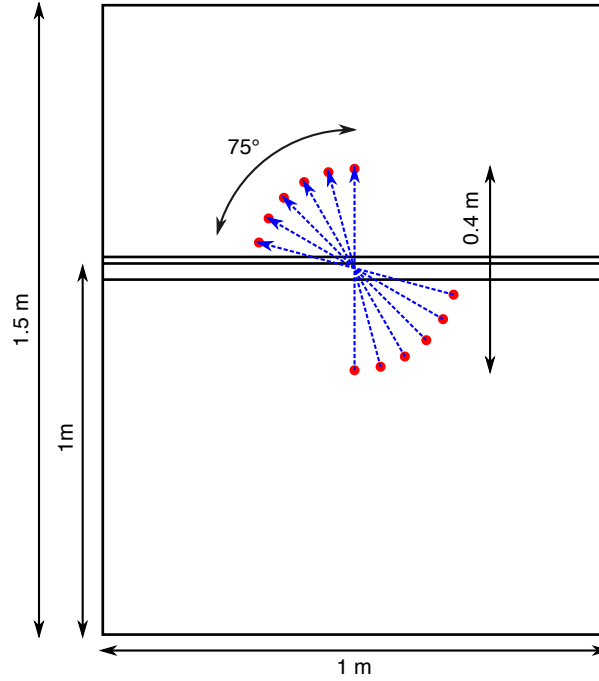


Figure 3.6: A plan view of the bolted L-section transmission experiment. Transducers are red circles and measured ray paths are blue dotted arrows.

The arrangement of the transducers allowed the direct wave paths across the stringer at different incident angles to be collected. The transducers on the lower half of the plate were excited in turn and the ultrasonic wave was measured on the corresponding transducer on the opposite side. The excitation used was a wideband chirp signal from 50 to 500 kHz. From this the responses for 5 cycle toneburst excitations at different frequencies could be deconvolved [77]. The transducers were bonded in place prior to any holes being drilled in the plate to attach the L-section which allowed clear path signals to be collected. Further measurements were then taken after holes had been drilled and finally after the L-section had been attached. This enables the transmission coefficient of a row of holes and the L-section to be measured.

Consistency test

Prior to the drilling of the holes or the attachment of the L-section, a consistency test was performed. 6 repeat collections were taken using the wideband chirp excitation and the maximum amplitude of the envelope of the first arrival was measured for signals deconvolved at different frequencies. These results are shown in figure 3.7 and it can be seen that the scatter for each frequency at each

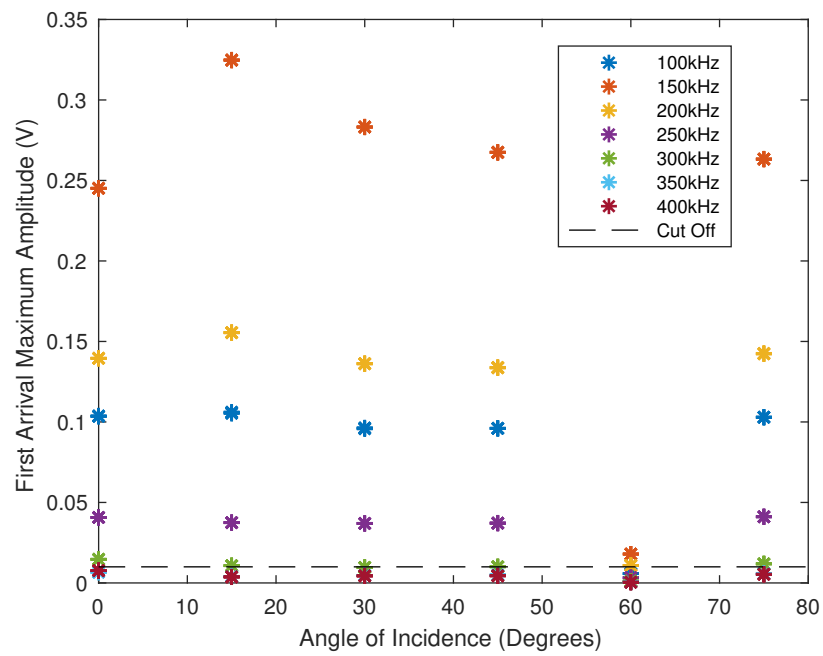


Figure 3.7: 6 repeated maximum amplitude measurements deconvolved at different frequencies for the plate prior to hole drilling and attachment of the L-section stiffener.

angle of incidence is very small and indistinguishable on this plot. For example the standard deviation of the 6 collections for 150 kHz at 15° is 0.128 mV. Due to the repeatability of the signals, repeat ultrasonic measurements for each angle will not be conducted because they are unnecessary.

This test also highlights a few limitations of the experiment. Firstly the pair of transducers at 60° are not generating as high an amplitude as the other transducers for all frequencies which suggests a problem with the transducers. Despite this, by inspection of the signals in figures 3.8 to 3.10, the signals seem valid if low in amplitude. Therefore the results at this angle should be treated with some caution. It also can be seen that the amplitude of the signals for the lower frequencies is much higher than that at higher frequencies. An amplitude cut off of 0.01 V was imposed to ensure there was enough energy in the signal to provide good information about the feature. This excludes the 350 and 400 kHz results. The deconvolved 300 kHz signal is on the borderline of this cut off but has been included. It can be seen in the signals shown in figure 3.10 that there are some strange arrivals in the 300 kHz signals. This is likely to be caused by deconvolving such low amplitude signals. Therefore the 300 kHz results should also be treated with some caution.

Measurement of transmission coefficient

The transmission coefficient was measured the same way as in section 3.2.1 (equation 3.1) except that the clear path signals were measured prior to the manufacture of the feature rather than at another position on the plate. The aim of the transducer layout was to enable both modes to be measured but, by inspection of the signals, it is clear this will not be possible for the A_0 mode. Example signals for different frequencies are shown in figures 3.8, 3.9 and 3.10 along with coloured highlighting of the expected direct path, reflected and mode converted signals arrival times. These regions were calculated by the same method as described in section 3.2.1. Note that the y axis for each angle is different. For the amplitude of the signals at each angle see figure 3.7. Although it does not occur at every angle and frequency combination, regularly reverberations or mode conversions from the feature extend into the A_0 region of the signal. This causes the transmission coefficient for the A_0 mode to be calculated as significantly greater than 1 at these positions. This is not possible. This occurs for both the row of holes and the bolted L-section. At certain frequencies there is also problems with ringing in the transducers which lengthen the S_0 signal into the A_0 region. Unfortunately this means it will only be possible to experimentally measure and generate models of the S_0 mode.

Figure 3.11 shows the experimentally measured transmission coefficient for

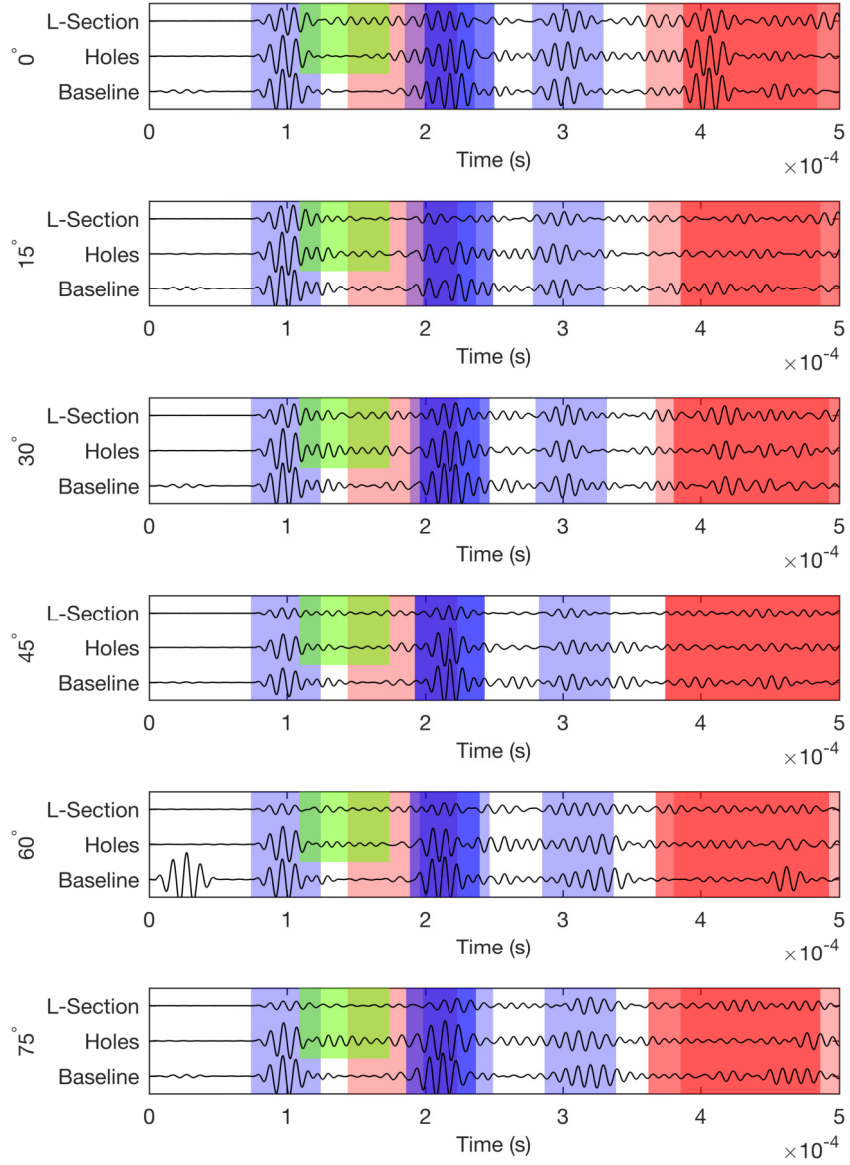


Figure 3.8: Example 100 kHz collected signals from the row of holes and the L-section experiments for different incident angles. The theoretical arrival times for the first arrival and subsequent first reflections for each mode are highlighted by the coloured shading; blue for the S_0 mode, red for the A_0 mode and green for the direct path mode conversion to the alternative fundamental mode.

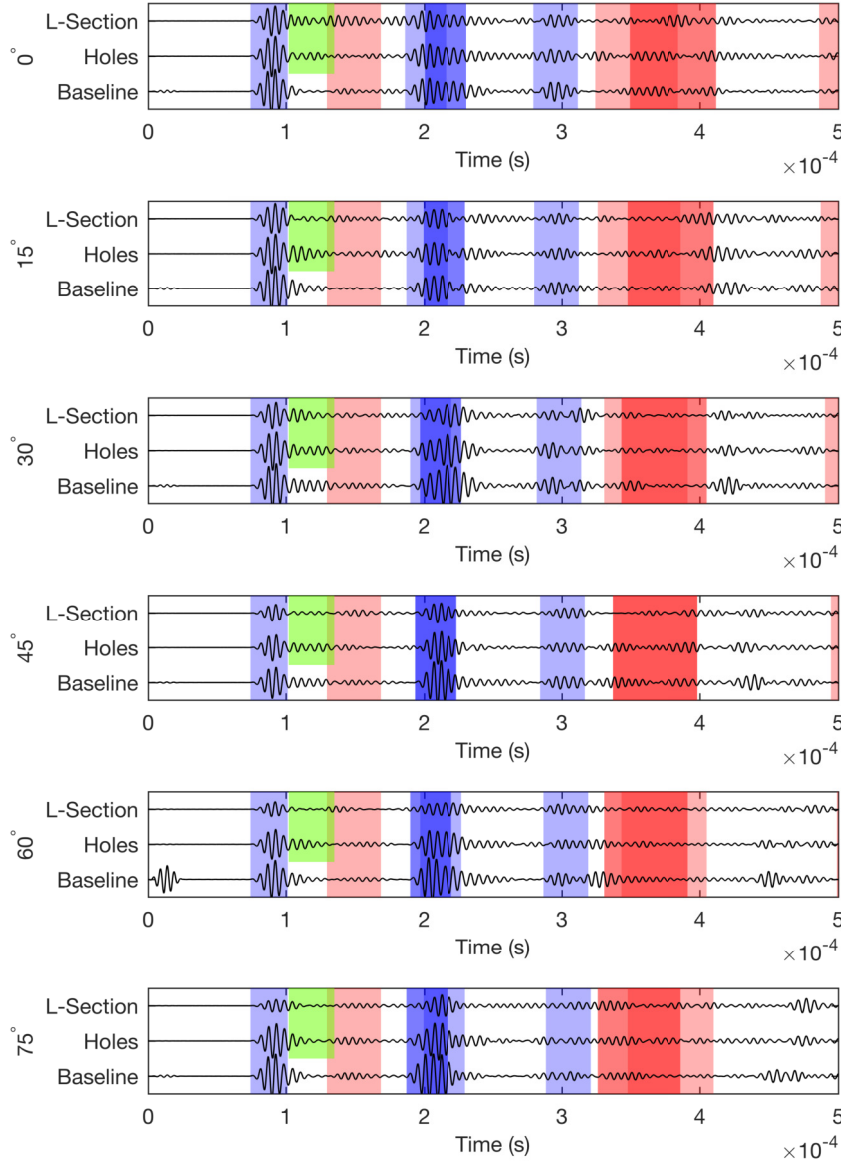


Figure 3.9: Example 200 kHz collected signals from the row of holes and the L-section experiments for different incident angles. The theoretical arrival times for the first arrival and subsequent first reflections for each mode are highlighted by the coloured shading; blue for the S_0 mode, red for the A_0 mode and green for the direct path mode conversion to the alternative fundamental mode.

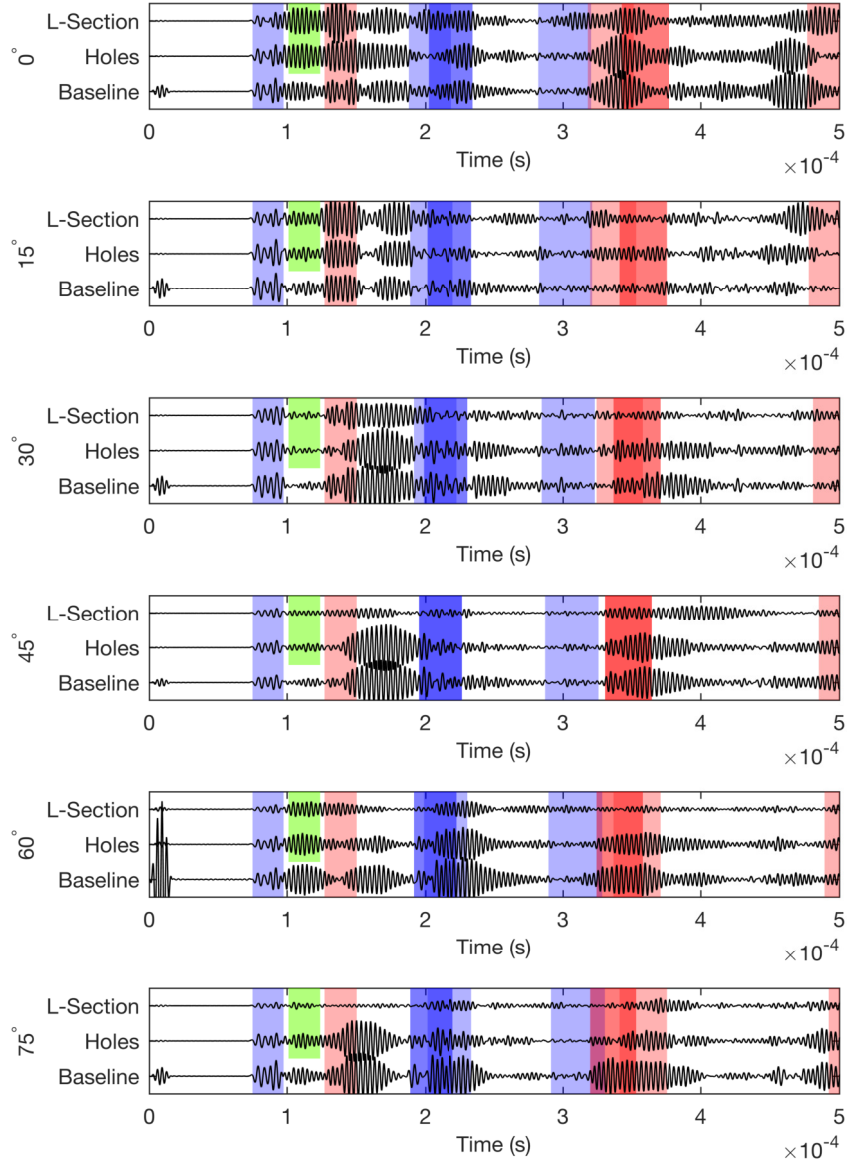


Figure 3.10: Example 300 kHz collected signals from the row of holes and the L-section experiments for different incident angles. The theoretical arrival times for the first arrival and subsequent first reflections for each mode are highlighted by the coloured shading; blue for the S_0 mode, red for the A_0 mode and green for the direct path mode conversion to the alternative fundamental mode.

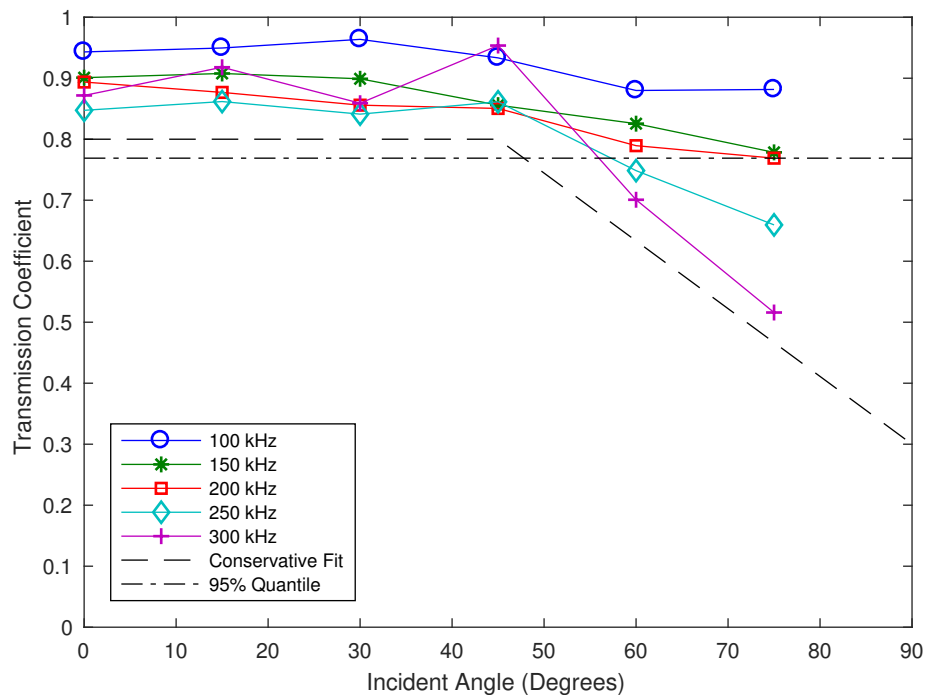


Figure 3.11: The transmission coefficient across a row of holes with a 25 mm spacing for different frequencies.

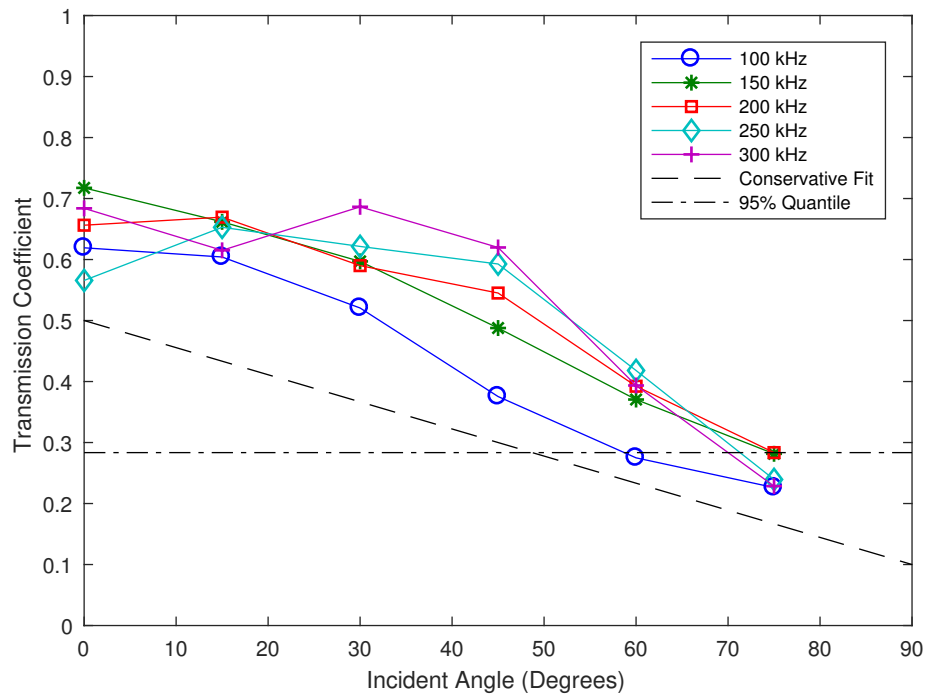


Figure 3.12: The transmission coefficient across a bolted L-section for different frequencies.

Frequency (kHz)	Wavelength (mm)
100	55
150	36
200	27
250	25
300	18

Table 3.1: The wavelengths of the S_0 mode in 3 mm aluminium for the frequencies of interest.

the row of holes for incident angles of 0° to 75° . The response that would have been collected from 5 cycle Hanning windowed tone burst excitations at different frequencies has been deconvolved from the wideband chirp response collected on the structure. For 0° to 45° the transmission coefficient stays constant and is greater than 0.8 for all frequencies. There is only a small difference in transmission for different frequencies with 100 kHz giving the highest value of transmission. At incident angles greater than 45° the behaviour is more frequency dependent with the transmission for higher frequencies being less. The wavelength of the higher frequency waves is more similar to the hole pitch and hole size. Therefore it is to be expected that the row of holes has a greater effect on these waves. The wavelengths corresponding to the frequencies of interest are shown in table 3.1 for reference. The transmission for all frequencies decreases to a greater or lesser extent at these incident angles.

The experimentally measured transmission across the L-section is shown in figure 3.12. In this case the behaviour is similar for all frequencies with the transmission decreasing from a value of about 0.65 to about 0.3 as the incident angle increases. Generally the value of transmission coefficient increases with frequency but the behaviour in this case is less frequency dependant than for the row of holes.

3.3 Selection of empirical models

The philosophy behind the modelling of these features is to create empirical models that are both simple to create and simple to use whilst still providing a good representation of the underlying guided wave propagation. The balance between simplicity and modelling accuracy will now be tested by creating several different empirical models of varying complexity. It would be useful to create models which can be applied to similar but not identical features as it would be infeasible to model and experimental measure transmission across every individual feature in a real aircraft. It is also useful to generalise across different frequencies because the frequency range AE events generate is not always known

and could be in a reasonably wide bandwidth. The models selected here will be tested against experiment results in the next chapter.

The first empirical model type will be a constant value which does not depend on input angle or frequency. The value chosen will be the lower quantile where 95 % of the experimentally measured transmission coefficients are higher in value. The box section experiment was only conducted at 190 kHz so this is the only frequency that can be measured for that feature. A wider range of frequencies was measured for the holes and L-section features but for consistency the single value will be defined by the 200 kHz results. These models will be referred to as the 95 % quantile models and are shown in figures 3.4, 3.11 and 3.12. This transmission model will be very simple to apply, even without the modelling framework used here, as it is a simple amplitude decrease. From inspection of the transmission coefficient plots, this modelling approach is likely to be more accurate for the box section and the row of holes than the L-section. This is because they exhibit less angular dependence than the L-section.

The next model type is a conservative fit that considers angular dependence and different frequencies where available. These transmission models are created manually and are lines of best fit to the lower measured values of transmission. These models are shown in figures 3.4, 3.11 and 3.12 and will be referred to as the conservative fit model. Because these models consider angular dependence it is likely that they will more accurately predict the wave propagation across the features than the 95 % models but will be less intuitive to apply. Due to the wider range of frequencies and therefore frequency-thicknesses considered in the hole and L-section models, it is aimed that these models will be suitable for similar but not identical features. An indication that this might be the case is that the 25 mm wide bolted L-section measured in [76] gives an S_0 transmission coefficient of approximately 0.8 at the measured incidence angles. This is notably higher than that predicted by the conservative fit model which is in this case a good thing because the model would under predict amplitude as desired. The large difference however highlights the balance that needs to be struck when using this approach to modelling features between accuracy and additional experimental or modelling work.

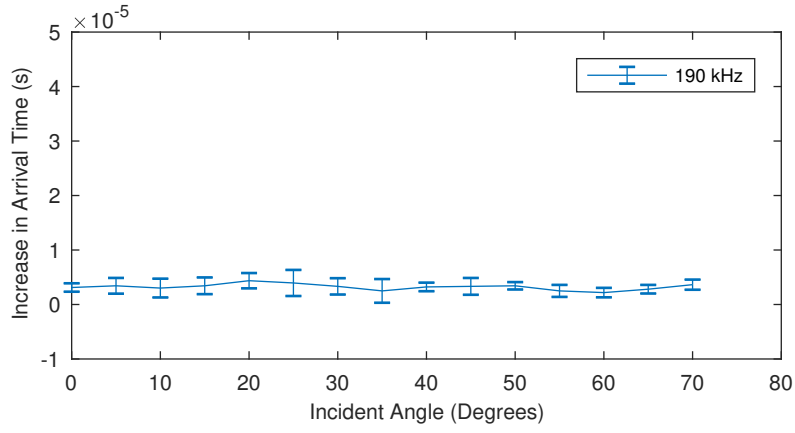
The final empirical model type used will be one that utilises all of the information available including frequency. Because different frequencies are required this will only be possible for the row of holes and L-section. The transmission coefficient here will be a linear interpolation between all the experimentally collected transmission coefficients from 100 to 300 kHz and angles of incidence from 0 to 75°. It is expected that this will be the most accurate empirical model but therefore may not translate well to other similar features.

3.4 Experimental measurement of time delay

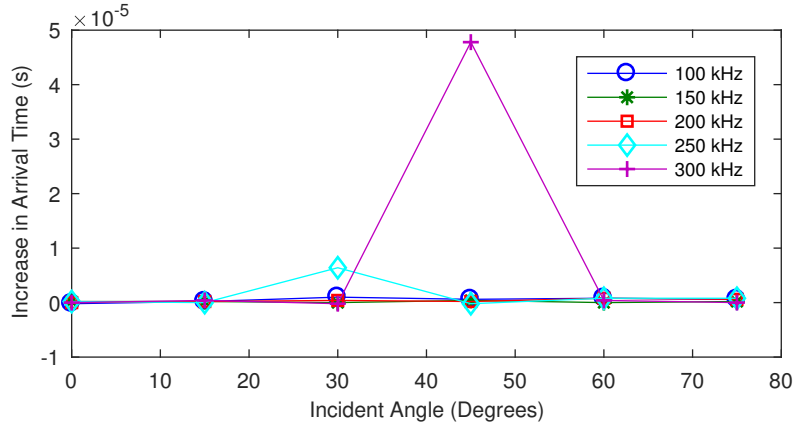
The final parameter to consider is the time delay caused by the wave propagating across features. This would potentially occur if the wave was propagating in a significantly different frequency-thickness region, propagated across the feature as a different mode or if there is interference of signals. The time delay was measured as the difference between the first arrival times for the clear path and feature path. The first arrival time was found using the threshold crossing method on the envelope of the signal. For the row of holes and L-section measurements the threshold was set to twice the maximum noise value. For the box section measurement the SNR of the feature path signals were sufficiently low that the threshold was set to 1.2 times the maximum noise value because this gave a more realistic measurement of the change in time delay between the signals.

The increase in arrival times for the different features are shown in figure 3.13. It can be seen that in most cases the time delay is small. For reference the time period of the excitations vary from 3.33×10^{-6} to 1.00×10^{-5} s for frequencies between 300 and 100 kHz respectively. Approximate values of the time delays are 3×10^{-6} s for the box section, 5×10^{-7} s for the row of holes and 2×10^{-6} s for the L-section. There are a couple of angle and frequency combinations where the time delay is significantly larger than these values. From inspecting the signals it can be seen that this has been caused by the threshold being crossed on different parts of the signal due to noise. It should be noted that this has occurred at the higher frequencies of 250 and 300 kHz where the SNR is significantly worse.

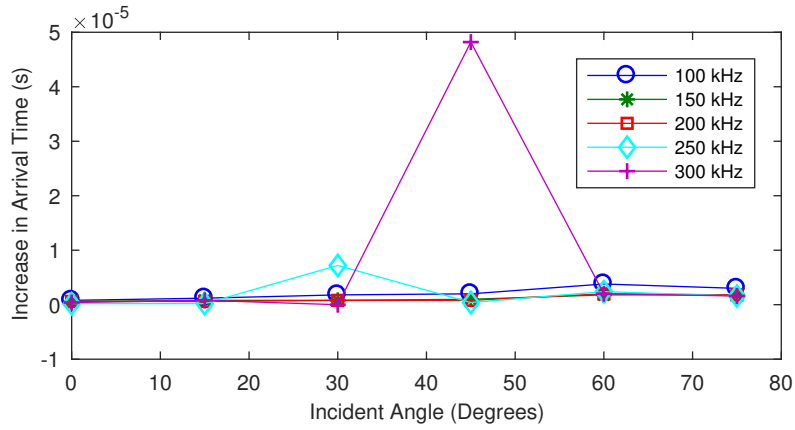
By inspecting the received signals it is clear that the cause of this small increase in arrival time is the decreasing amplitude of the signals that have crossed the features. This causes the point on the signal envelope which crosses the threshold value to be later in time. The decreasing amplitude is included in the empirical models described above so the additional modelling of time delay is not required for any of these features for this frequency range. This is also a promising result for performance of AE source location algorithms which would be negatively affected by a time delay they do not consider.



(a) Box section



(b) Row of holes



(c) L-section

Figure 3.13: The increase in arrival time measured between the clear path signal and the signal that has crossed different features. The error bars on the box section results show the standard deviation for 5 repeated measurements.

3.5 Conclusions

In this chapter the wave propagation across features has been investigated. This is a factor that is not always considered when designing GWSHM systems yet can cause significant amplitude loss which will affect system performance. Modelling features is therefore a very important component of the overall system models being developed in this work.

Many models of guided wave propagation across features are described in the literature and a selection of these are described at the beginning of this chapter. These models could potentially be used in the overall system model. An alternative empirical modelling approach is suggested after the literature review which requires less effort to implement, assuming validation experiments would have to be conducted on other modelling approaches. The S_0 transmission coefficients across different stiffening features has been measured. These features were a bonded box section, a row of holes and a bolted L-section. From these experimental measurements, 3 different types of empirical models have been created of increasing complexity. The accuracy and conservatism of these models will be tested in the following chapter.

Chapter 4

Validation of Empirical Transmission Models

This chapter will experimentally validate the empirical transmission models developed in the previous chapter. Three different approaches to creating the empirical transmission models were utilised for a bonded box section, a row of holes and a bolted L-section. The assumptions in each approach creates transmission models with different levels of conservativeness. It should be noted again that one of the key facets of the transmission models developed in this work is that they aim to be conservative in their prediction of amplitude. This is to prevent over confidence in the range the model predicts AE signals could propagate. Therefore there is a different balance in each of the models between accuracy and conservativeness, the effects of which will be analysed here.

The empirical transmission models will be compared with experimentally measured signals on different structures with different features. These include a plate with 2 bonded box sections, a plate with 2 bolted L-sections and a section of the upper wing skin of an Airbus A320. This combination of structures enables the different models to be compared with features that are identical to those the empirical models were generated from and features that are similar in profile but not identical.

4.1 The model to be validated

To validate the empirical transmission models a reduced form of the overall GWSHM system model, shown in equation 2.1 (repeated below), will be used.

$$H(\omega) = S(\omega)U(\omega)Y(\omega) \sum_{ray\ paths} \left[R_X(\omega)E(\omega)P(\omega)A(\omega)B \prod_{reflections} R_C(\omega) \prod_{transmissions} T_C(\omega) \right] \quad (2.1 \text{ repeated})$$

The equation can be reduced because the model will be compared with the first arrival from the simulated AE source. Therefore there will be no reflections and only one ray path and mode, S_0 , are relevant. The source, elastic wave excitability, receiver characteristics and amplifier will be accounted for by one experimentally measured scale factor; S_{SF} . The material used throughout this work is aluminium and the attenuation in this material is negligible so this term can be omitted. No post processing was applied to simulated or experimentally received signals. Therefore equation 2.1 reduces to:

$$H(\omega) = S_{SF}P(\omega)B \prod_{transmissions} T_C(\omega) \quad (4.1)$$

The value of S_{SF} will be found from the experimental data used to validate the transmission models. The scale factor is calculated using the measurement points collected before the source signal has propagated across any geometrical feature. Two methods will be used to determine S_{SF} ; a mean of the maximum first arrival of these signals and the lower quantile of the same values so that 95 % of amplitudes will be higher.

4.2 Validation on a plate with 2 bonded box sections

The first models to be tested against experimental results were those for the bonded box section. This experimental data for validation was collected on a

Transducer Number	X Position (m)	Y Position (m)
1	0.168	0.190
2	0.482	0.204
3	0.830	0.223
4	0.160	0.612
5	0.479	0.664
6	0.849	0.621
8	0.496	1.061

Table 4.1: The transducer positions for the structure with 2 bonded box sections.

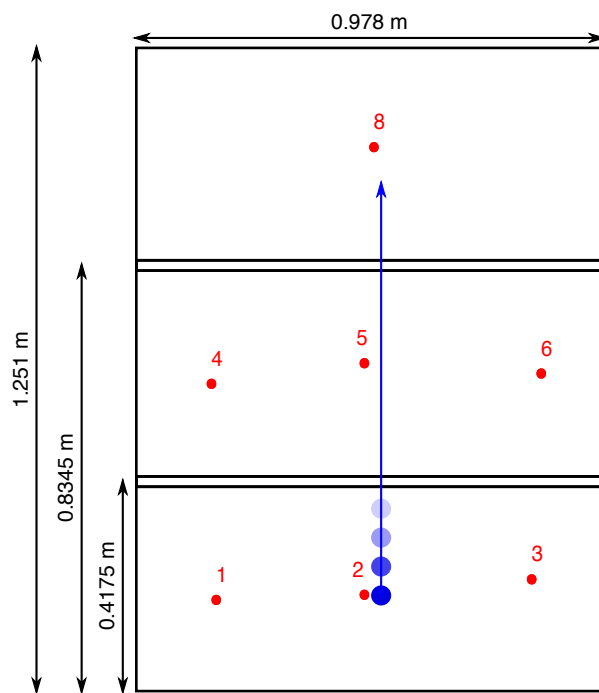


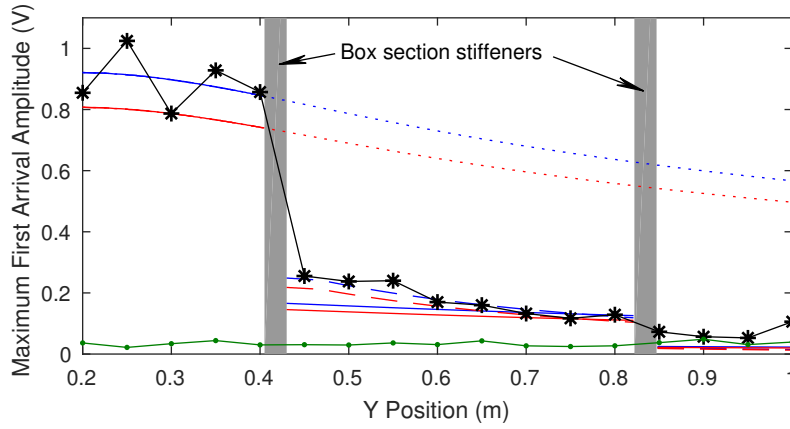
Figure 4.1: Plan view of the structure with 2 bonded box sections. The transducers positions are shown by the red circles. The blue arrow shows the line and direction of EMAT measurements.

plate with 2 bonded box sections. The plate was the same thickness and the box section stiffeners were built using the same method as in the previous experimental work, described in section 3.2.1. This means, barring manufacturing consistency, the features are identical to that which the empirical models were generated from. The plate was not in pristine condition because it had been used for active GWSHM experimental work beforehand. A few small bits of simulated damage were present though not where the experimental measurements in this work were taken. This may minimally affect the propagating signals but given AE systems aim to be applied to real structures which will not be pristine, this is not an unreasonable situation for validation.

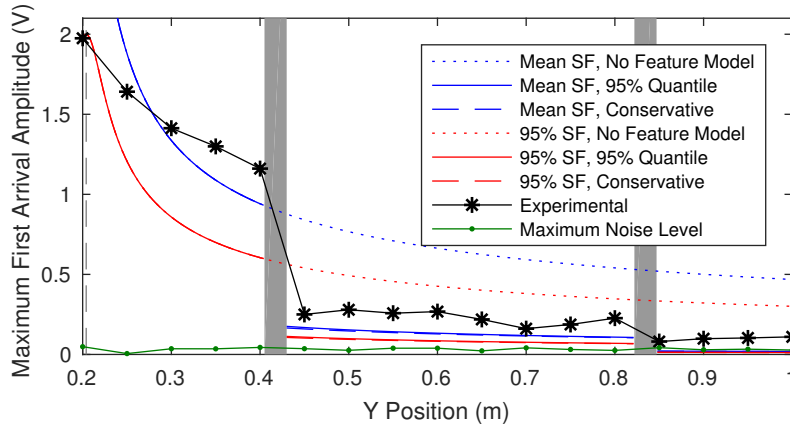
The aluminium plate with 2 bonded box section stiffeners is shown in figure 4.1. Bonded to the plate were 7 20 mm diameter and 1 mm thick PZT disk transducers. The transducers were positioned at the locations listed in table 4.1. These transducers were the same type as used in section 3.2.2 and are predominantly sensitive to the S_0 mode. A line of measurement positions were defined from point [0.5 m, 0.2 m] to point [0.5 m, 1.0 m], where the bottom left corner is considered the origin. Along this line a measurement point was defined every 5 cm. An EMAT was moved to each measurement position and used as the receiver. Each element in the transducer array was excited in turn before the transducer was moved. This is the inverse to the true operation of an AE system and was done for experimental convenience but the signals collected would be the same due to reciprocity. The excitation was a Hanning windowed 5 cycle 190 kHz tone burst which was the same as used in section 3.2.1.

From the signals collected, the maximum amplitude of the first arrival was found. This is the first arrival for the S_0 mode. The experiment was then simulated using the different models of the transmission across features and the predicted signals obtained. These signals were then scaled using the different scaling approaches. The region used for scaling was the signals collected prior to the first feature. This region therefore changes depending on which transducer is being modelled. The model predictions of maximum first arrival amplitude could then be found using the same signal processing as in the real experiment.

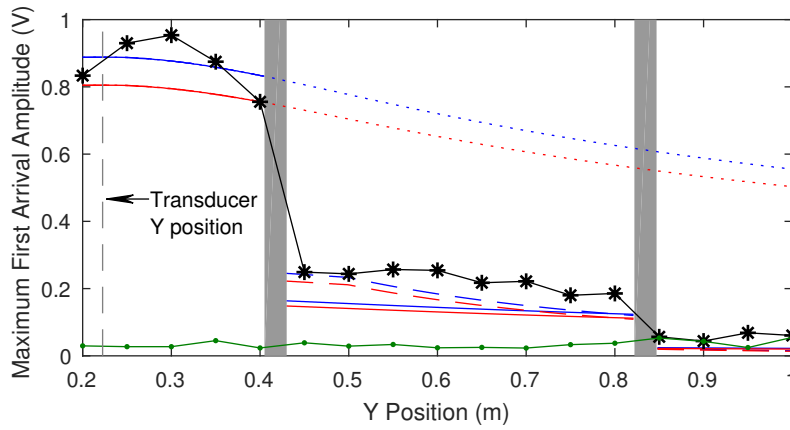
Figure 4.2 shows the experimental value of maximum first arrival amplitude and the different model predictions for each transducer at the different measurement points. The modelling result with no transmission models included is also shown for reference. In this example the predominant factor affecting amplitude is beam spread. It should be noted that transducer 6 is not operating as well as the other transducers and consequently the maximum amplitude values are significantly lower than the similarly positioned transducer 4. This is due to damage to the transducer in storage. It should also be noted that the EMAT pre-amplifier begins to saturate above 1 V and the amount of amp-



(a) Transducer 1

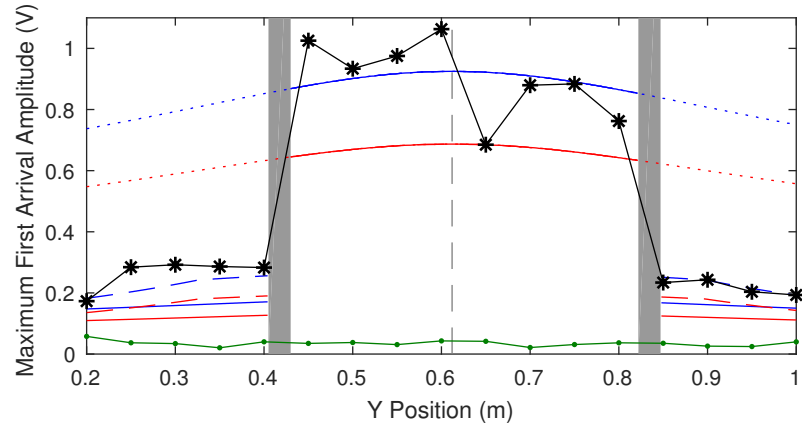


(b) Transducer 2

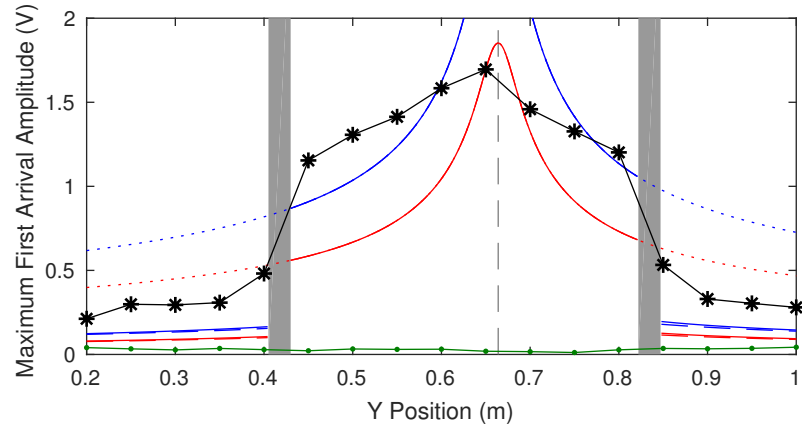


(c) Transducer 3

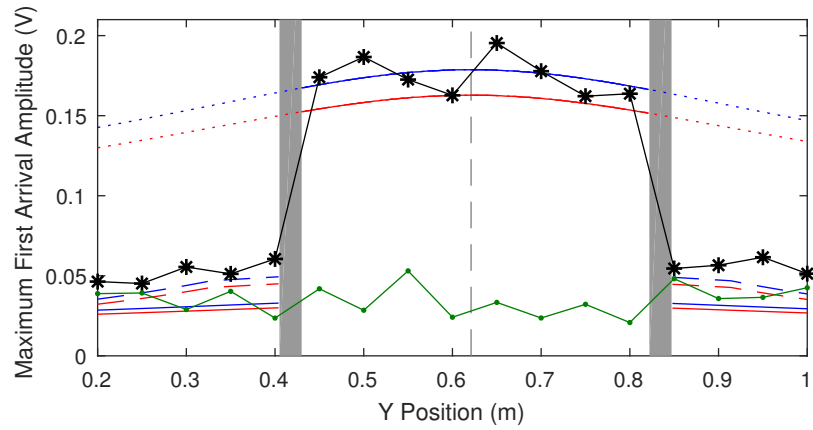
Figure 4.2: Comparisons between experimentally measured and modelled first arrival amplitude from an AE source received at different transducers on the structure with 2 bonded box sections. Different models with different transmission models and transducer Scale Factor (SF) values are shown.



(d) Transducer 4



(e) Transducer 5



(f) Transducer 6

Figure 4.2: Comparisons between experimentally measured and modelled first arrival amplitude from an AE source received at different transducers on the structure with 2 bonded box sections. Different models with different transmission models and transducer Scale Factor (SF) values are shown.

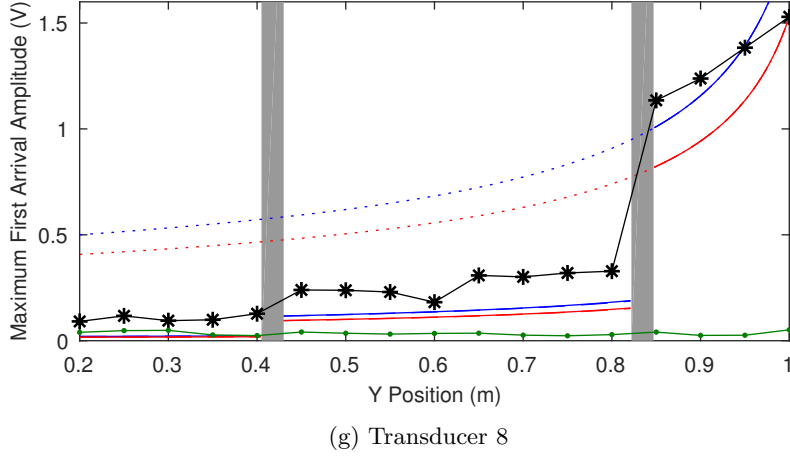


Figure 4.2: Comparisons between experimentally measured and modelled first arrival amplitude from an AE source received at different transducers on the structure with 2 bonded box sections. Different models with different transmission models and transducer Scale Factor (SF) values are shown.

lification slowly decreases near this value. However a balance had to be made during the data collection between this amplification loss near the transducer and the SNR at positions after multiple features. Because a lot of the scaling calculations occur in this region, this pre-amplifier problem has increased the conservatism of the model for transducers 2, 5 and 8. The maximum amplitude of the noise in the pre-trigger region is also shown on these plots to give an indication of the SNR. In the cases where the received signal had propagated across 2 features the SNR was small. For transducers 1 and 3 at a number of these measurement positions the signals are too small to be useful.

It can be seen in figure 4.2 that qualitatively both transmission models pre-

Transmission model type	Scale factor method	Mean absolute difference (V)	% points above model
No Feature	Mean	0.3291	19.3
Model	95 % Quantile	0.2678	36.1
95 % Quantile	Mean	0.1070	81.5
	95 % Quantile	0.1474	100.0
Conservative Fit	Mean	0.0989	77.3
	95 % Quantile	0.1397	99.2

Table 4.2: Comparison of mean absolute difference and points above the model for the different transmission models and scaling techniques for the signals collected on the structure with 2 bonded box sections. Note for comparison that the maximum amplitude after the wave had propagated across at least 1 feature is 0.5326 V. This is the maximum for all transducers.

dict amplitudes close to that which is experimentally measured. At transducer positions where the propagating wave crosses the feature at small incident angles there is little difference between the predictions for each technique. This is to be expected because, at incident angles close to 0° , the 2 transmission models are very similar in value. At positions where the direct ray path crosses the features at larger incident angles then the difference between the 2 models is more apparent. The higher prediction in amplitude of the conservative fit transmission model matches the trend of the experimental amplitude better. This is to be expected as the conservative fit transmission model is designed to be more accurate than the 95 % quantile model.

These figures also show the difference between the 2 methods of finding S_{SF} . As would be expected, the mean value is higher than the lower 95 % quantile and the difference in the values predicted by the model can be quite large in the region prior to the propagating wave crossing any features. However, once signals are being collected on the other side of a feature, it is clear that the reduction in amplitude due to the transmission coefficients has a significantly greater effect than the scaling factor.

Table 4.2 shows the mean values of absolute difference between the experimental measurements and the different models and the percentage of points above the models for all of the transducers. The absolute difference between the experimental measurements and the models is calculated by sampling the model at the experimental measurement positions. The values shown in this table show clearly the different balances between accuracy and conservative amplitude estimation for the different transmission models and scaling methods.

The combination that provides the smallest mean absolute difference is the mean scaling factor and the conservative fit transmission model. This is the combination of most accurate scaling method and transmission model on a structure with identical features so this is the expected result. It should be noted that the points above this modelling combination is 77.3 % not 50 % which shows that this modelling is still conservative.

If an additional requirement that 95 % of the experimentally measured amplitudes is greater than the model is applied, then a different combination is needed. Only 2 combinations satisfy this requirement; the 95 % scale factor and the 95 % quantile model and the 95 % scale factor and the conservative fit model. Between these 2 methods the latter is slightly more accurate and therefore preferred despite the small increase in model complexity. The mean absolute difference between model and experiment for this technique is 0.1397 V which, for reference, is about half the amplitude of the signals received after they have crossed one of the box sections.

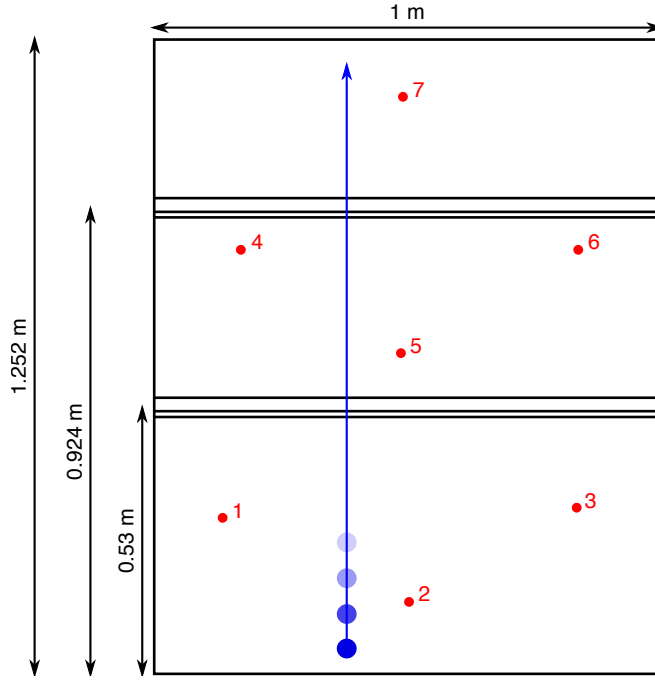


Figure 4.3: Diagram showing the 2 bolted L-sections structure. The red dots and numbers correspond to the transducer positioning and transducer number. The blue arrow corresponds to the line and direction of EMAT measurements.

4.3 Validation on a plate with 2 bolted L-sections

A similar experimental setup to that used for the box section was used to validate the model for the bolted L-section. Two L-section stiffeners were bolted to a 3 mm thick aluminium plate. The L-sections were the same dimensions as those used in section 3.2.2 and therefore were identical to the L-section the empirical models were generated upon. 7 McWade NS3303 transducers were bonded to the plate using Dow Corning 3140 RTV Coating. These transducers had a centre frequency of 150 kHz. A diagram of this structure is shown in figure 4.3 and the

Transducer Number	X Position (m)	Y Position (m)
1	0.125	0.298
2	0.493	0.132
3	0.824	0.318
4	0.161	0.827
5	0.477	0.623
6	0.827	0.827
7	0.481	1.129

Table 4.3: The transducer positions for the structure with 2 bolted L-sections.

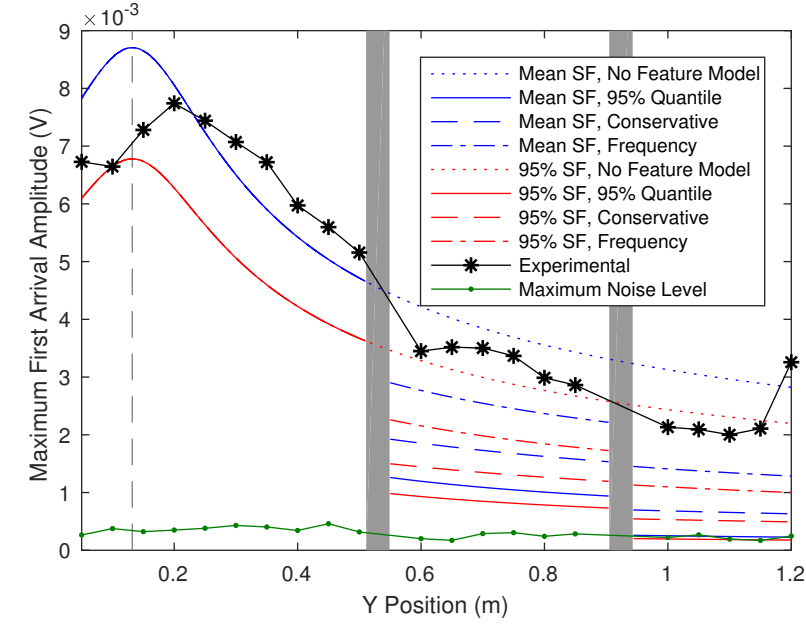
transducer positions are listed in table 4.3.

An EMAT representing an AE source was moved in a line across the plate and signals were collected every 5 cm. The line of collections was 38 cm from the longer edge and the EMAT had a centre frequency of 190 kHz. The EMAT was excited with a 190 kHz chirp excitation [77]. This is the inverse operation to that used for the validation of the box section and removed the necessity to use an EMAT pre-amplifier. This means that there is no reduced amplification above 1 V but meant that the signal amplitude was much smaller. Signals from the EMAT were received on transducers 2 and 6. The responses for a Hanning windowed 5 cycle tone burst excitation at 150 and 200 kHz were deconvolved from the chirp excitation. This enabled the performance of the transmission models to be assessed at different frequency-thicknesses.

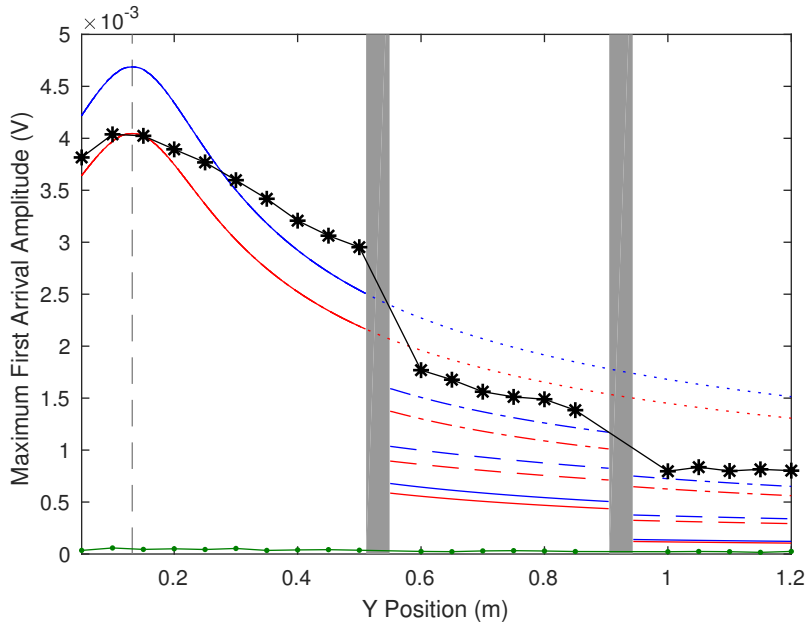
As was done previously, the experimental collections were simulated using the different transmission models and values of S_{SF} . The maximum amplitude of the first arrival was then found from both the model and experimental signals and these results are shown in figures 4.4 and 4.5. The maximum amplitude of the noise in the pre-trigger section of the experimental signals is also shown on these figures for reference.

The results for transducer 2 are shown in figure 4.4. It can be seen that the experimental and modelling results are similar for both frequencies. Where the signal is received in the first quadrant, before it has crossed a feature, it can be seen that the decrease in amplitude of the modelling result has a steeper gradient than in the experimental results. This is likely to be caused by the beam spread being modelled as an asymptote at the transducer position. This is an approximation that is unrealistic for measurement positions close to the transducer because the transducer will have a finite maximum amplitude. This may increase the conservatism of the amplitude predictions due to the effect this has on the scaling. After the received signals have crossed a feature, it can be seen that all of the transmission models under predict on amplitude. The frequency model has the smallest difference to the experimental results. This is followed by the conservative fit model and then the 95 % quantile model.

Figure 4.5 shows the results for both frequencies for transducer 6. Again the results at the 2 different frequencies are quite similar. Transducer 6 is further away from the collection points than transducer 2 and this means the potential poor fit of modelling transducers as a point source has less of an effect. This makes both scaling methods less conservative which means the frequency transmission model predicts amplitudes very close to and sometimes higher than the experimentally measured ones. At this transducer position the incident angle as the propagating wave crosses the L-section is large. At these angles of incidence the 95 % quantile model is sometimes less conservative than the other

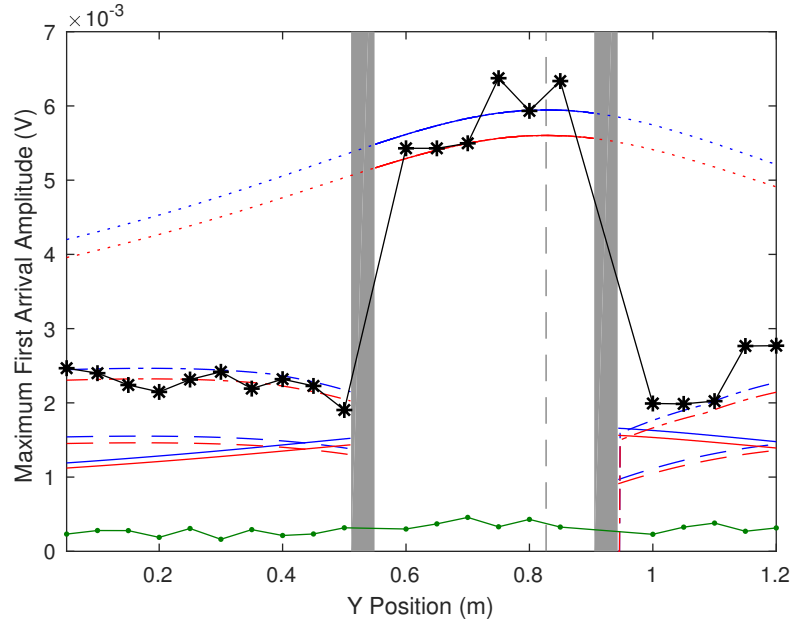


(a) 150 kHz excitation

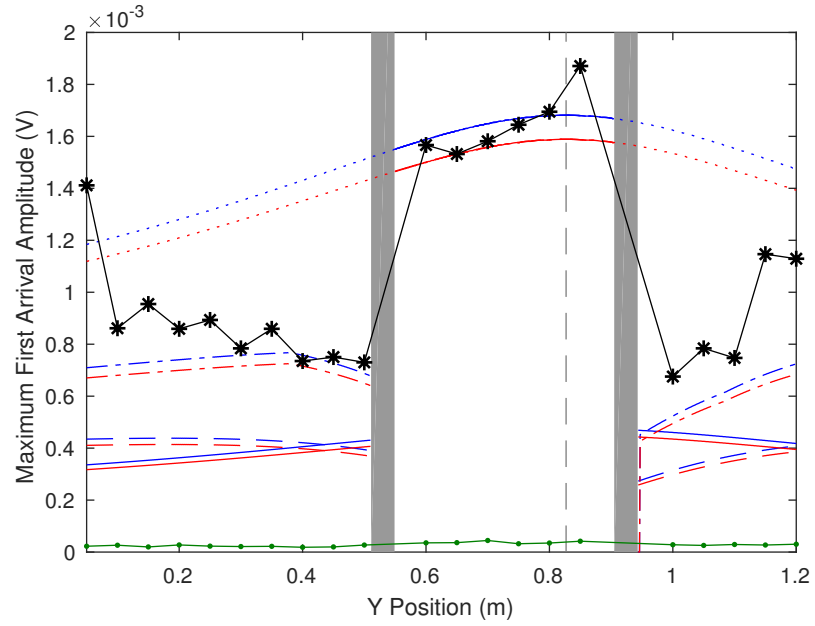


(b) 200 kHz excitation

Figure 4.4: Comparisons between experimentally measured and modelled first arrival amplitude from an AE source received at transducer 2 on the structure with 2 bolted L-sections. Different models with different transmission models and transducer Scale Factor (SF) values are shown.



(a) 150 kHz excitation



(b) 200 kHz excitation

Figure 4.5: Comparisons between experimentally measured and modelled first arrival amplitude from an AE source received at transducer 6 on the structure with 2 bolted L-sections. Different models with different transmission models and transducer Scale Factor (SF) values are shown. The line colours correspond with those in figure 4.4.

Transmission model type	Scale factor method	Mean absolute difference (V)	% points above model
No Feature	Mean	9.0963×10^{-4}	20.2
Model	95 % Quantile	8.5663×10^{-4}	47.6
95 % Quantile	Mean	7.9423×10^{-4}	79.8
	95 % Quantile	9.2071×10^{-4}	100.0
Conservative Fit	Mean	6.8040×10^{-4}	79.8
	95 % Quantile	8.2791×10^{-4}	100.0
Frequency	Mean	3.6350×10^{-4}	66.7
	95 % Quantile	5.2984×10^{-4}	94.1

Table 4.4: Comparison of mean absolute difference and points above the model for the different transmission models and scaling techniques for the signals collected on the structure with 2 bolted L-sections. Note for comparison that the maximum amplitude after the wave had propagated across at least 1 feature is 0.0035 V. This is the maximum across the different transducer and frequency combinations.

models and this can be seen in its amplitude predictions. Also at angles of incidence greater than 75° the frequency model is not defined as experimental measurements were not made at these angles. Therefore there can be seen one point after the wave has crossed the upper feature where the modelling result for the frequency transmission model goes to zero.

Table 4.4 summaries the results for both transducers at both frequencies. Similarly to the results on the structure with 2 box sections the mean scaling method consistently produces a more accurate but less conservative model. The frequency transmission model gives the smallest value of mean absolute difference between the experimental and modelling results. This is followed by the conservative fit then 95 % transmission models. Only 2 model and scale factor combinations satisfy the requirement to have 95 % of the experimental measurements to be higher than the model predictions. This is the 95 % scaling factor with the 95 % quantile transmission model and the 95 % scaling factor with the conservative fit transmission model. This is the same pair as the for the box section. Out of this pair the conservative fit transmission model result is the more accurate with a mean absolute difference of 3.635×10^{-4} V. Depending on the example this is between a half and a tenth of the maximum amplitude of the signal after it has crossed one feature. The 95 % scaling factor and the frequency transmission model come close to satisfying the requirement with 94.1 % of points being above the model prediction.

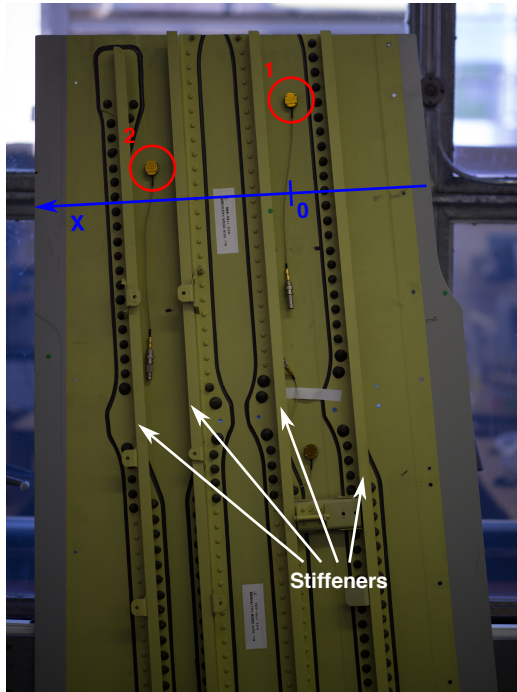


Figure 4.6: Picture of the section of A320 wing skin. The line and direction of measurements is shown by the blue arrow, the transducer positions are highlighted by the red circles and the stiffeners are labelled in white.

4.4 Validation on a section of A320 wing skin

The final structure that the transmission models will be tested upon is a section of A320 wing skin. This is an aluminium structure that consists mainly of a plate that varies in thickness from approximately 1 to 3 mm. Bolted to the plate are 4 stiffeners which vary in shape between an I-section and an L-section. The spacing between the bolts varies but is generally around 25 mm. The stiffeners are also bonded onto the plate with a sealant. The features on this structure are therefore not identical to any of the features modelled in this work but are approximately similar to an L-section in profile.

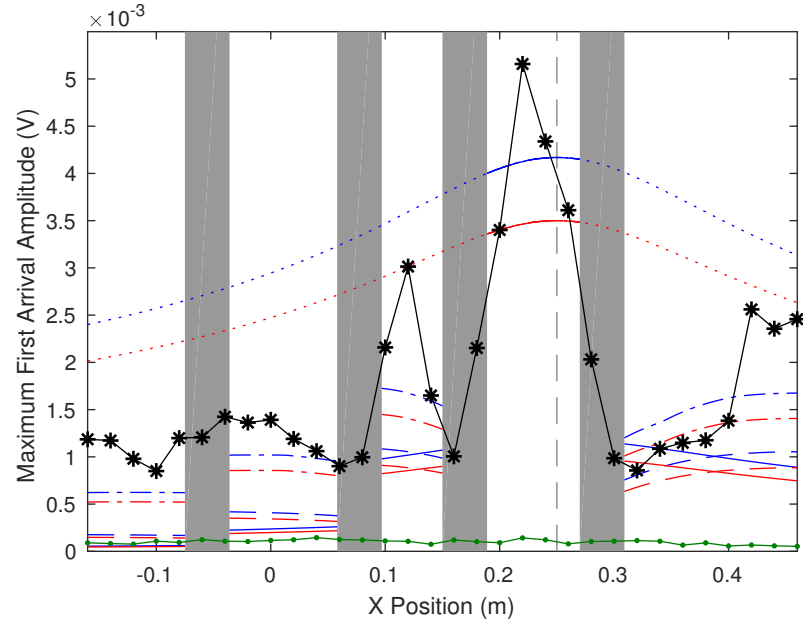
An array of 300 kHz McWade NS3303 transducers was bonded to the wing skin using Dow Corning 3140 RTV Coating. An EMAT acted as a source and was moved in a line below transducers 1 and 2. The measurements were taken on the outer wing surface which is smooth. The approximate position of the line of measurements is shown on the other side where the features are visible in figure 4.6. The transducer was moved along the line at increments of 2 cm and it was excited with a 190 kHz chirp excitation. As was done with the experiment with the 2 bolted L-sections, this was deconvolved to give the signals that would have been received from 150 and 200 kHz 5 cycle Hanning windowed tone burst excitations.

The structure was modelled using the bolted L-section transmission models in the position of the stiffeners. The thickness in the model was set to 3 mm. The received signals at the 2 transducers were then simulated using each of the L-section transmission models and the different scaling techniques. The maximum amplitude of the first arrival envelope was then found for the experimental and modelled signals. These results are shown in figures 4.7 and 4.8.

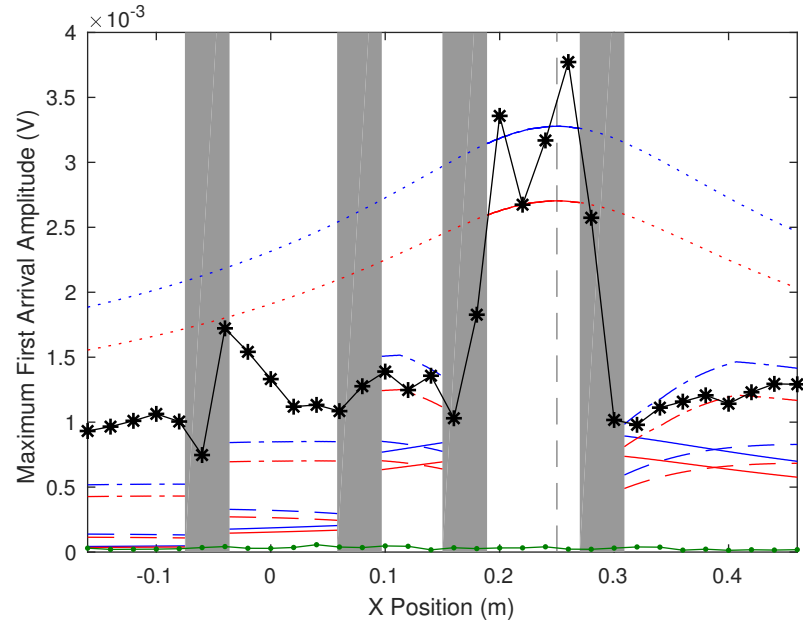
For the signals received at transducer 1, shown in figure 4.7, it can be seen that there is a significant drop in amplitude across the first stiffener on either side of the transducer. This happens for both frequencies of excitation and matches the amplitudes predicted by the various models reasonably well. Once the signal has propagated across more than 1 stiffener, as it does on the left of these plots, then the experimentally measured amplitude drop over further stiffeners is less significant than predicted by any of the models.

A similar pattern is present on the left of the plot for the 200 kHz excitation at transducer 2 which is shown in figure 4.8b. The amplitude decrease over the first stiffener matches the L-section models reasonably well. This is not the case for the right side of this plot or for any signal received at 150 kHz which is shown in figure 4.8a. At these positions the experimentally measured amplitudes best match the modelling results where no feature model is included.

These observations suggest that at measurement positions where the incident

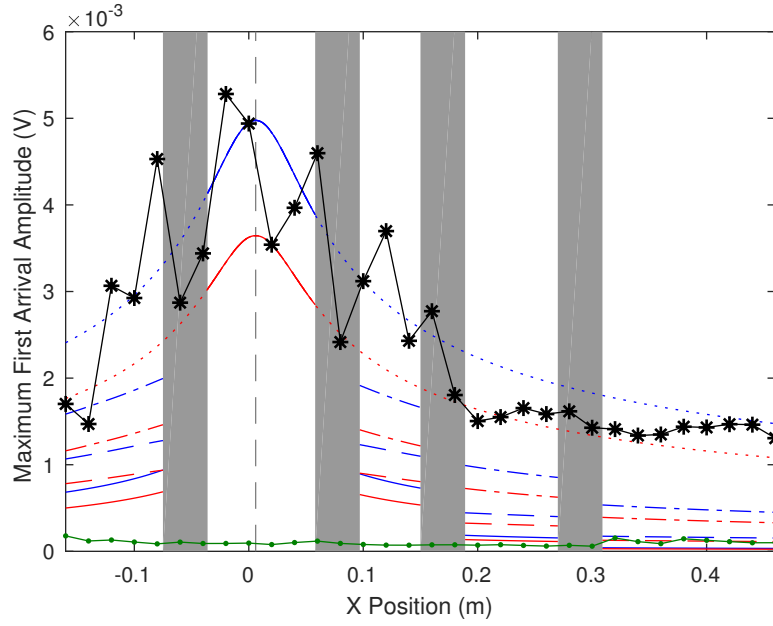


(a) 150 kHz excitation

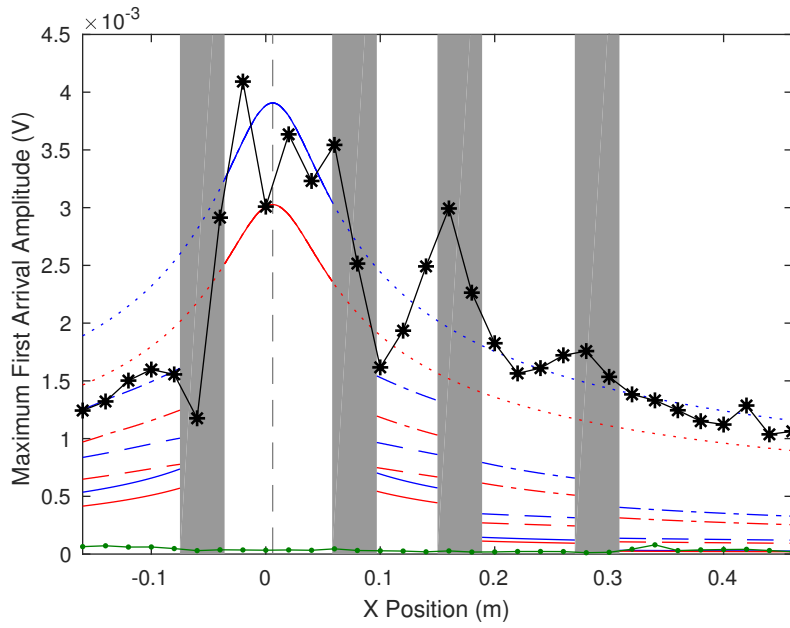


(b) 200 kHz excitation

Figure 4.7: Comparisons between experimentally measured and modelled first arrival amplitude from an AE source received at transducer 1 on a section of A320 wing skin. Different models with different transmission models and transducer Scale Factor (SF) values are shown. The line colours correspond with those in figure 4.4.



(a) 150 kHz excitation



(b) 200 kHz excitation

Figure 4.8: Comparisons between experimentally measured and modelled first arrival amplitude from an AE source received at transducer 2 on a section of A320 wing skin. Different models with different transmission models and transducer Scale Factor (SF) values are shown. The line colours correspond with those in figure 4.4.

Transmission model type	Scale factor method	Mean absolute difference (V)	% points above model
No Feature	Mean	9.3284×10^{-4}	17.2
Model	95 % Quantile	7.6741×10^{-4}	46.9
95 % Quantile	Mean	0.0010	87.5
	95 % Quantile	0.0011	99.0
Conservative Fit	Mean	8.9251×10^{-4}	89.6
	95 % Quantile	0.0010	100.0
Frequency	Mean	5.6607×10^{-4}	68.8
	95 % Quantile	7.2178×10^{-4}	94.8

Table 4.5: Comparison of mean absolute difference and points above model for the different transmission models and scaling techniques for the signals collected on the section of A320 wing skin. Note for comparison that the maximum amplitude after the wave had propagated across at least 1 feature is 0.0045 V. This is the maximum across the different transducer and frequency combinations.

angle of the propagating wave to the feature is small, the models significantly under predict amplitude. Therefore it is likely that the transmission coefficient at small incident angles is larger for the stiffeners used here than the bolted L-section from which the empirical models are derived. This could be for various reasons including the differing geometry or the presence of the sealant increasing transmission at certain incident angles. It is also worth noting that the stiffeners on the A320 wing skin are quite closely spaced and therefore there may be some interaction between the features and that they cannot be considered as wholly independent.

Table 4.5 shows the mean absolute difference between the experimental results and model predictions and the percentage of experimentally measured points that are higher in value than the model. Note that where the experimental measurement point is on a feature the model is undefined and no values are calculated. This is because the mechanism of how the wave propagates across the feature and how that affects the signal is not included in the empirical model. The mean absolute difference is quite large in value for all modelling techniques compared to the signal amplitude. This is to be expected give the differences between the models based on a bolted L-section and the real stiffeners. When considering the requirement that 95 % of the modelled points are higher in amplitude, a similar pattern to the previous validations occurs. The 2 approaches that satisfy this requirement are the 95 % quantile scaling factor with the 95 % quantile transmission model and 95 % quantile scaling factor with the conservative fit transmission model. Overall applying this modelling approach with the L-section transmission models on this structure provides satisfactorily conservative amplitude predictions but with limited accuracy, especially at points further from the transducer.

4.5 Conclusions

In this chapter the different empirical transmission models for stiffeners created in chapter 3 were tested against experimental data collected on 3 different structures. The parameter that was used for validation was the maximum amplitude of the first arrival. This was chosen because it is the key parameter in determining the performance of threshold based AE systems. Two of these structures had features identical to those from which the empirical models were derived. The third structure was a section of A320 wing skin which had 4 stiffeners attached. These stiffeners were similar in geometry to a L-section but were not identical to the L-section used to generate some of the empirical models.

On the structures with features identical to those used to generate the empirical models, the amplitudes predicted by the model behaved as expected. The modelling approaches that were expected to be the most accurate gave the smallest absolute difference in first arrival amplitude. The modelling approaches that were expected to be more conservative in their amplitude prediction behaved in this way.

On the A320 wing skin the modelling results were less accurate. Given that there were many simplifications in the construction of the model compared to the real structure and the transmission coefficients were for slightly different features this is to be expected. However when considering the conservative fit models, these performed just as well based upon the conservative metric as they had on the other less challenging structures.

The results in these tests demonstrate the balance between accuracy and conservatism in amplitude prediction that is implicit in this modelling approach. Reasonably accurate empirical models can be generated but, as was summarised in section 3.1, many approaches for accurate transmission models on different features exist and perform well. Instead the main focus of the feature models and overall approach here has been to predict the performance of AE systems with reduced experimental and modelling effort whilst still providing a useful model output. This has lead to the deliberately conservative predictions of amplitude which guarantee that AE sources of a known amplitude can be detected at a certain range. In many cases the wave is likely to be of higher amplitude but this will not affect the system performance significantly. However if the wave is lower than predicted threshold amplitude then this could cause a missed detection.

These experimental tests show that the more conservative transmission models can be used to aid the design of AE systems because they will conservatively predict the key parameter of amplitude. This means that whether a known AE event will trigger a transducer can be determined confidently. This has been shown on structures with identical features to those on which the empir-

ical models have been based, in some cases for a small divergence in frequency. With a more restricted accuracy, using approximate rather than identical feature models has also been demonstrated to provide suitably conservative amplitude predictions. They therefore can be used as basis for creating forward models of a system which can be used to aid overall AE system design. The approach on a new structure should be to obtain conservative models of transmission for the main types of geometrical feature then refine the model by increased modelling effort or experimental work on the specific features as need or resources allow.

Now that the accuracy and conservatism of the transmission models has been understood they will be used to demonstrate how benefit can be drawn from this type of modelling. These results will be shown in the next chapter. Unless otherwise stated, the conservative fit transmission model will be utilised to represent features because this method of generating an empirical model has been shown to satisfy the 95% of points above the model criteria with the greatest accuracy of amplitude prediction.

Chapter 5

Example Uses of Modelling

In this chapter examples of how the modelling framework can be used with the AE source defined in chapter 2 and the transmission models developed in chapters 3 and 4 will be shown. The aim behind the modelling is provide a flexible tool to aid understanding of how an AE system will perform. This could be used to design new experiments or installations or to provide more information about existing setups. In this chapter simple examples will be used to highlight how different aspects of AE system's performance can be assessed using the model. These examples include determining which transducers will be triggered by AE events at different locations, understanding how the transducers affect location accuracy, comparing how different location algorithms perform and understanding potential problems when using the slower A_0 mode.

5.1 Modelling details

The overall LTI model for an AE system is shown in equation 2.1 and this is repeated here:

$$H(\omega) = S(\omega)U(\omega)Y(\omega) \sum_{ray\ paths} \left[R_X(\omega)E(\omega)P(\omega)A(\omega)B \right. \\ \left. \prod_{reflections} R_C(\omega) \prod_{transmissions} T_C(\omega) \right] \quad (2.1\ repeated)$$

This model can be simplified for the single mode modelling examples given the following assumptions and simplifications:

- The AE systems considered here operate using a threshold crossing method

Transducer Number	X Position (m)	Y Position (m)
1	0.210	0.206
2	0.792	0.250
3	0.809	1.004
4	0.220	0.996
5	0.499	0.198
6	0.503	1.010
7	0.499	0.398
8	0.503	0.810

Table 5.1: The positions of transducers in the modelling examples.

and assume the first triggering arrival has propagated by the direct path between the AE source and triggered transducer. This means only the direct ray path and the relevant mode needs to be considered. Therefore there is only 1 ray path and no reflections that need to be modelled.

- The AE source and the excitability of the elastic waves at the source will be modelled as one term, $S_E(\omega)$, where:

$$S_E(\omega) = S(\omega)E(\omega) \quad (5.1)$$

This means the source term is dependant on the material, material thickness and mode that is considered [44].

- No amplifiers or signal post processing will be modelled here.
- The structures modelled here are constructed from aluminium. Attenuation in aluminium is negligible so this term is omitted for the results shown here.

Applying these conditions reduces equation 2.1 to:

$$H(\omega) = S_E(\omega)R_X(\omega)P(\omega)B \prod_{transmissions} T_C(\omega) \quad (5.2)$$

Examples of the modelling will be shown on a 1 m wide, 1.2 m tall and 3 mm thick aluminium plate with a feature positioned across the centre. The feature will change between some of the examples but, unless otherwise stated, the transmission model will be of the conservative model type as shown in chapter 3. The material properties used in the model are a density of 2700 kg/m³, Young's modulus of 70 GPa and Poisson's ratio of 0.34.

Transducers are placed in the positions shown in table 5.1. The transducers have been deliberately arranged with a small perturbation of up to 5 cm from a geometric grid because this has been found to improve performance of some AE

location algorithms by reducing identical triggering times of transducers. The transducers used in these examples will be McWade 300 kHz NS3303. These will be modelled by the values of frequency response, $D^{250\text{ kHz}}$, that are listed in section 2.3.1 which were found from [44]. At 250 kHz these transducers are approximately 7 times more sensitive to the A_0 mode than the S_0 mode.

The AE source used throughout these examples is that from a fatigue crack in a 3 mm plate that is described in section 2.3.1 and shown in figure 2.3. This source produces a larger amplitude displacement of 449 pm for the A_0 mode than 19.5 pm for the S_0 mode. The centre frequency of the excitation will be 250 kHz and it will be modelled as a 2 cycle Hanning windowed tone burst. Unless otherwise stated, the S_0 mode will be modelled as it is the fastest propagating mode at the frequency-thickness range considered. Arrivals of this mode are therefore likely to be the first to reach the transducers. This is despite this mode being significantly smaller in amplitude.

The final parameter to set is the threshold the signal needs to exceed for it to be deemed to have been detected on a transducer. This is not directly part of the model of the signals but is typically how an AE system processes the signals it receives. The value of threshold will be based upon the same work as was used to determine the AE source in chapter 2 which is [14]. The threshold will be set to the maximum value of the noise in this work which is measured from the figure repeated here as figure 2.1. This gives the threshold a value of 2.89 mV.

5.2 Predicting the triggered transducers

The most important factor in an AE system is that it can detect AE events in the area it is monitoring. An AE event is detected on a transducer if the maximum amplitude of the signal exceeds the threshold of 2.89 mV. If the signal exceeds the threshold it is often referred to as having triggered the transducer. For an AE event to be detected it must first trigger 1 or more transducers. Figures 5.1, 5.2 and 5.3 show the number of transducers that will be triggered by events throughout the plate for 3 different features; a row of holes, a bolted L-section and a bonded box section. All of the transmission models used here are described in chapter 3. Each pixel in these images represents an AE source location.

Figure 5.1 shows the result for a plate with a line of holes feature. It can be seen that AE events at all positions throughout the plate would trigger all 4 transducers and therefore can easily be detected. The line of holes has a large value of transmission coefficient at all incident angles. Figure 5.2 shows the results in the case where the feature is a bolted L-section. The L-section has a

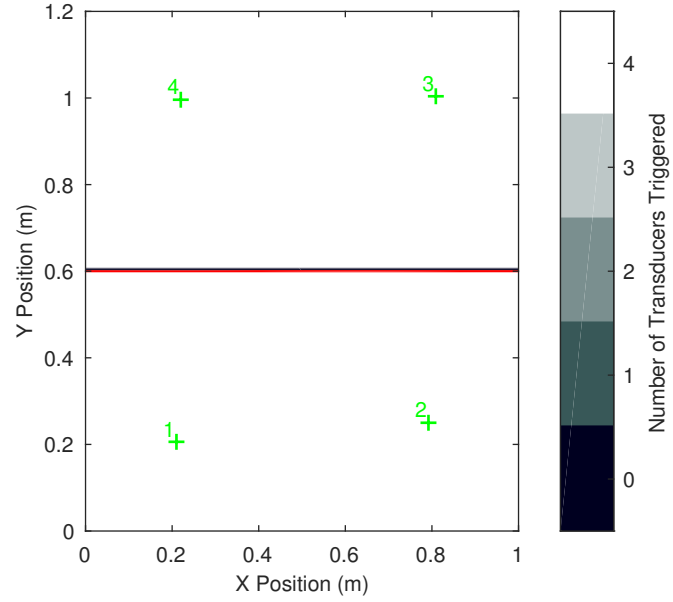


Figure 5.1: The number of transducers (green crosses) AE events at different positions will trigger with row of holes (red line) in between. Each pixel in the image represents an AE source location.

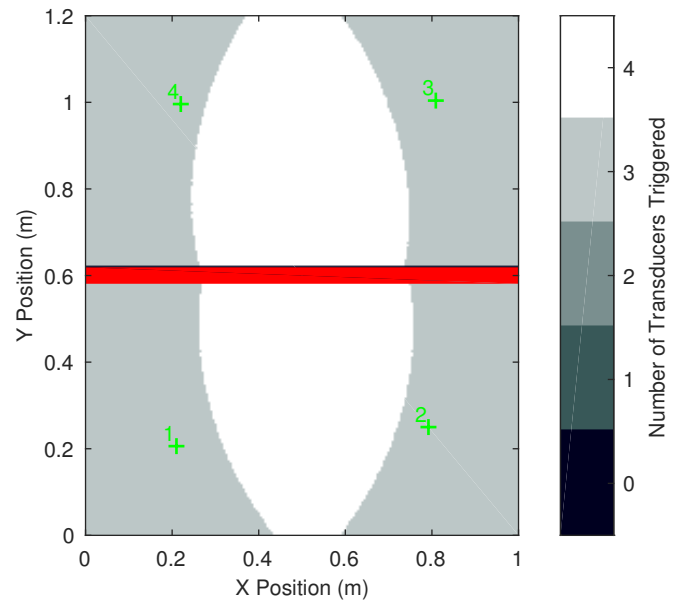


Figure 5.2: The number of transducers (green crosses) AE events at different positions will trigger with a bolted L-section (red line) in between. Each pixel in the image represents an AE source location.

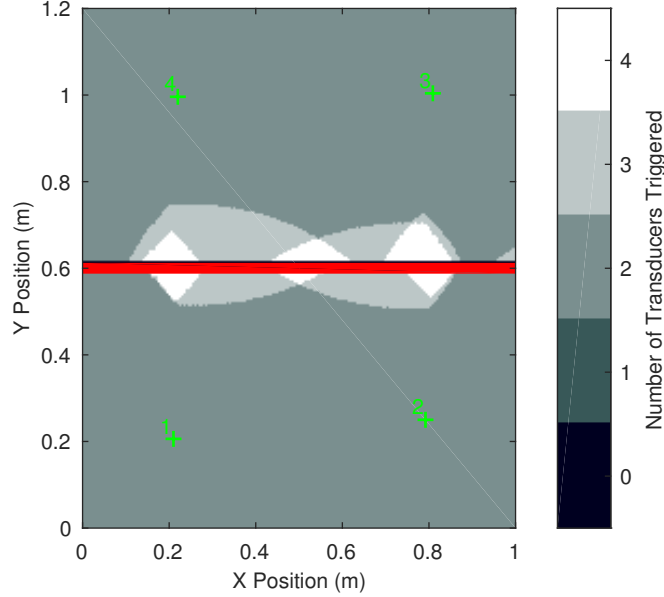


Figure 5.3: The number of transducers (green crosses) AE events at different positions will trigger with a bonded box section (red line) in between. Each pixel in the image represents an AE source location.

lower transmission coefficient than the line of holes and this means at positions at the sides of the plate the AE events are only detected by 3 transducers. In the central section all transducers can still detect the AE event. AE events can therefore still be easily detected throughout the plate. The final example is shown in figure 5.3 for the bonded box section. This is a highly attenuating feature which means in the majority of the plate only 2 transducers will be triggered by AE events at these positions. This means AE events can be detected at all positions within the plate but not by that many transducers.

The number of triggered transducers also determines if and how well AE events can be located. The majority of location methods require at least 3 transducers to be triggered to successfully locate an event. Therefore this would not be possible at most potential AE event positions in the structure with a bonded box section. In some cases, as discussed in the next section, it is desirable to use 4 transducers for location and this would not be possible in certain regions of the plate with a bolted L-section.

Given many industrial AE tests are designed just considering the plate properties, where detection limits will be determined by attenuation and beam spread, situations can be conceived where this modelling approach would be useful to guarantee detection and location would be possible.

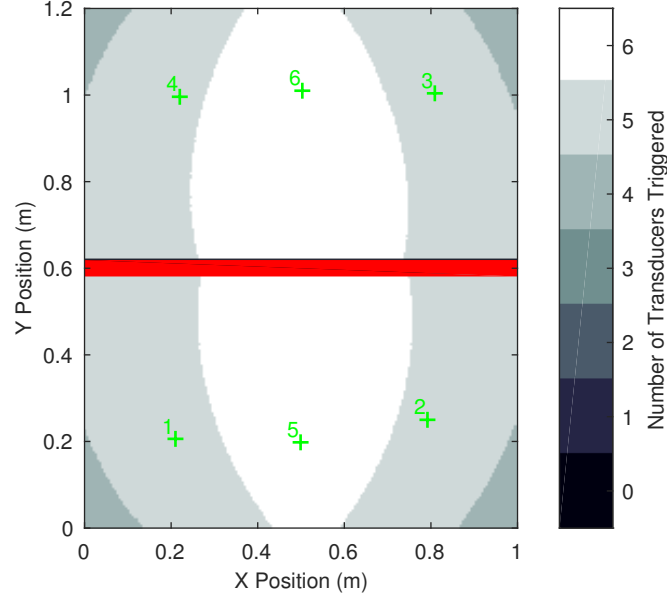
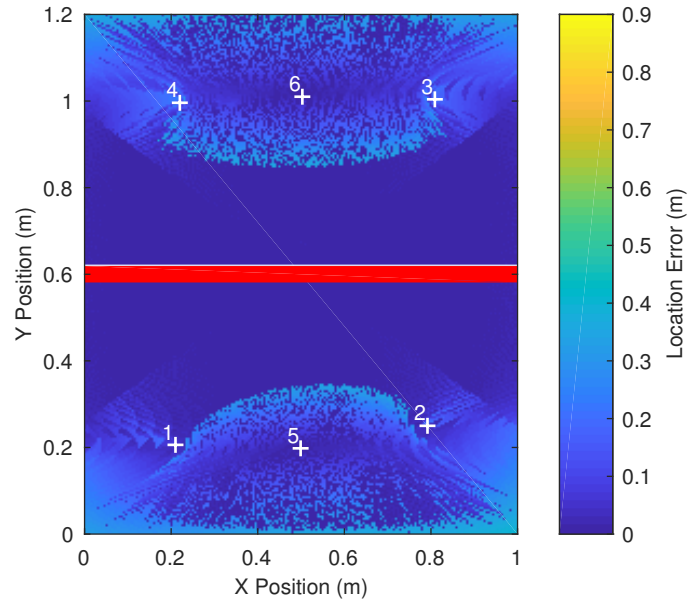


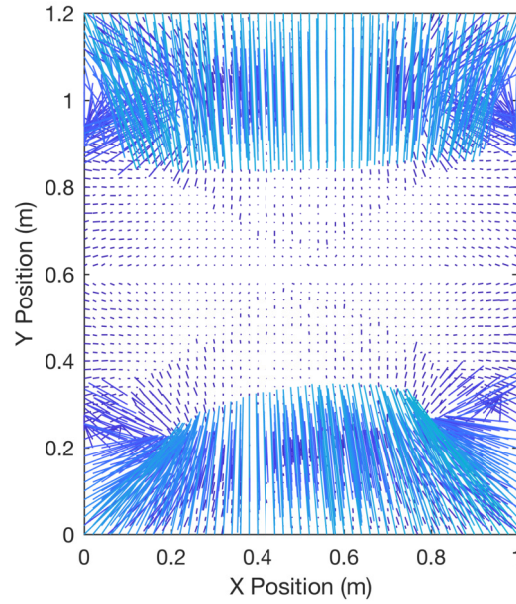
Figure 5.4: The number of transducers (green crosses) AE events at different positions will trigger with a bolted L-section (red line) in between. Each pixel in the image represents an AE source location.

5.3 The influence of number of transducers on location accuracy

In this section the influence on the number of transducers on location performance will be investigated using the model. The location algorithm used will be the Point Method described in [37]. This is a numerical method where an array of ΔT values, the time difference between triggering of different transducers, are generated for a structure and transducer layout. The closest match in this array to experimentally measured or, in this case, simulated ΔT values is then found and the location of the AE event is inferred. This method has been chosen in preference to alternative analytical approaches because it is very robust and has been found to perform better in situations with low amplitude signals which is the case here. The following section will discuss different location algorithms in more detail. The ΔT array has been generated using the plate properties and does not consider the existence of a feature. It would be possible to include this information in the ΔT array if sufficient information was known about the AE source but this is often not the case. Also no significant time delay was found for the bolted L-section when this was measured in section 3.4. Positions in the ΔT array were calculated for a grid of possible locations within the area of the



(a) The location error for AE events for a plate with a bolted L-section in the centre (red line). The location algorithm is the Point Method using 3 transducers. Each pixel in the image represents an AE source location. The transducer locations are shown by white crosses.



(b) The location line plot for the location algorithm and transducer arrangement shown above. One end of each line represents the true source location and the other shows the location determined by the algorithm. This figure shows a subset of AE source positions for clarity.

Figure 5.5

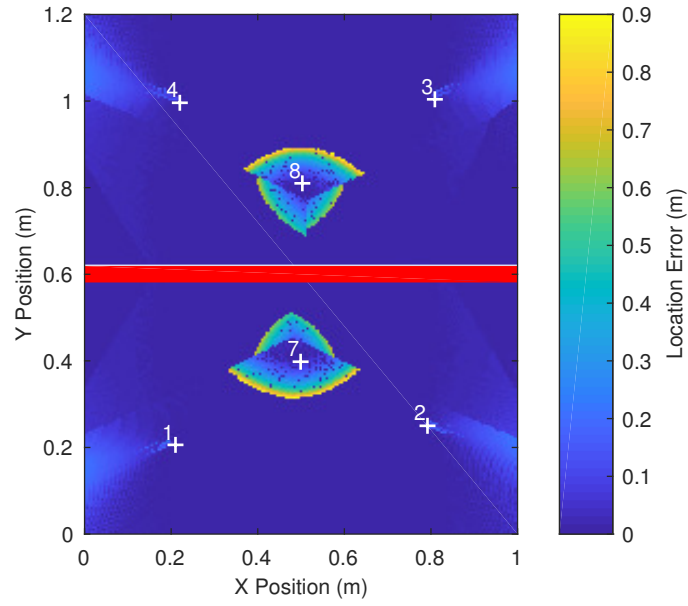
plate. There was a 1 mm space between each location point in the grid in both the x and y directions.

The structure upon which the location performance will be assessed is the same as the L-section structure in section 5.2 but with two additional transducers to ensure that at least 4 transducers will be triggered by each AE event. The number of transducers triggered is shown in figure 5.4.

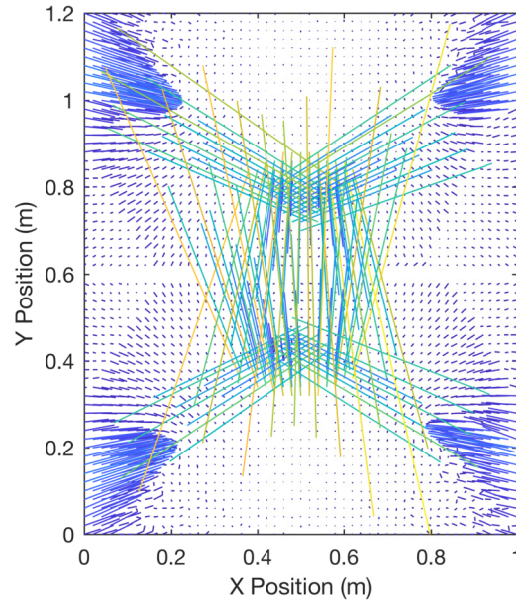
The minimum number of transducers required to determine the location of an AE event is 3. This gives 2 ΔT values to be matched. The location results where 3 transducers are arranged in approximately a line either side of the feature are shown in figure 5.5a. It can be seen that the location error is generally small but there are regions where the location error is greater than 0.3m. This includes regions inside the area covered by the transducers. The cause of this error is overlap in the ΔT array where similar combinations of ΔT values correspond to markedly different locations. There is a particularly large overlap in this ΔT array because of the arrangement of the transducers. For many of the AE events in this structure the first 3 triggering transducers will be in a straight line. It is therefore hard for the algorithm to discriminate if this event occurred above or below the line of transducers. This can be clearly seen in the location line plot for this setup shown in figure 5.5b where some of the events are located on the opposite side of the line of transducers to their true location. In this type of plot one end of each line shows the true AE source location and the other end is at the position at which the event has been located by the algorithm.

The lack of accuracy where transducers are arranged in a line is a well known problem with AE location algorithms and is typically prevented by arranging the transducers in a pattern where they form less shallow triangles. This has been attempted and the results are shown in figure 5.6. It can be seen that generally the location error is smaller throughout the plate but larger location errors of up to 0.9m are present in regions surrounding the central transducers. This is again caused by overlap in the ΔT array. In practise it is very difficult to remove all regions of overlap in the ΔT array when using only 3 transducers. Just rearranging the transducers to avoid shallow triangles does not remove regions where large location errors can occur.

Another potential method of solving this problem is to find the location using 4 transducers and therefore 3 ΔT values. This significantly reduces the cases where there can be overlap in the ΔT array. This has been done with the original transducer layout and the result is shown in figure 5.7. The location error is generally smaller in this example but errors of up to 0.35m do exist in regions close to the corners of the plate in the regions near and behind the transducers.

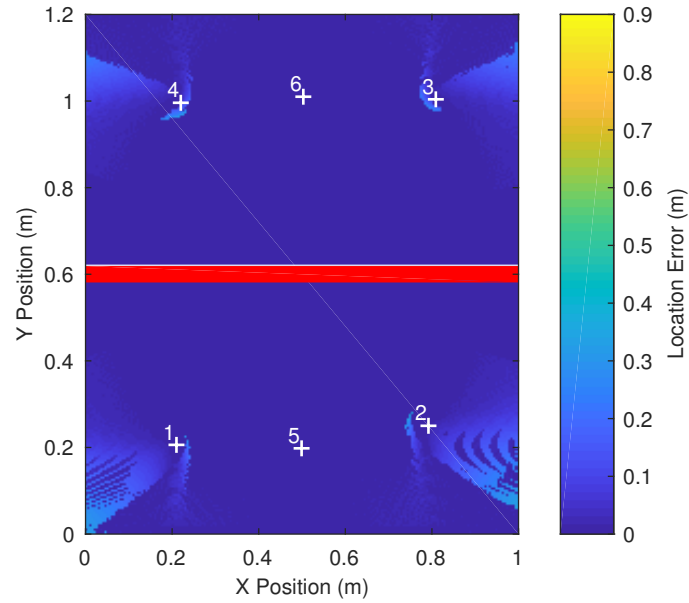


(a) The location error for AE events for a plate with a bolted L-section in the centre (red line). The location algorithm is the Point Method using 3 transducers. Each pixel in the image represents an AE source location. The transducer locations are shown by white crosses.

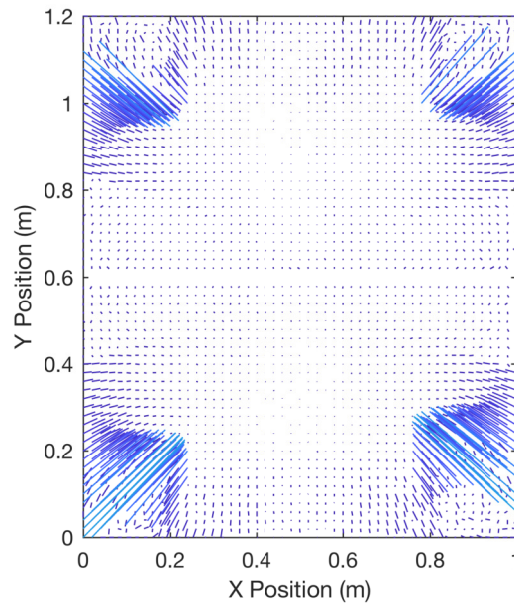


(b) The location line plot for the location algorithm and transducer arrangement shown above. One end of each line represents the true source location and the other shows the location determined by the algorithm. This figure shows a subset of AE source positions for clarity.

Figure 5.6



(a) The location error for AE events for a plate with a bolted L-section in the centre (red line). The location algorithm is the point method using 4 transducers. Each pixel in the image represents an AE source location. The transducer locations are shown by white crosses.



(b) The location line plot for the location algorithm and transducer arrangement shown above. One end of each line represents the true source location and the other shows the location determined by the algorithm. This figure shows a subset of AE source positions for clarity.

Figure 5.7

This section shows the challenges of arranging transducers to give good location accuracy. This is on simulated data so additional experimental error is likely to exacerbate these challenges. In situations such as this where the signal to noise ratio is low it would be best to tailor the transducer layout to the area where AE is most likely to occur. This could be done with this modelling approach. There is also a clear advantage in using 4 transducers for location. This would be especially true if the only potential AE source locations could be guaranteed to be within the region surrounded by the transducers because this would further reduce the overlap in the ΔT array. However this is unlikely to be possible on most real structures.

5.4 Comparing location algorithm performance

After detection the next step for an AE system is to locate the position at which the AE event occurred. There are many different approaches and algorithms that can be used to find the location of the source. Some of these are discussed in section 1.5.3. In this section it will be shown how the model can be used to predict the performance of 2 location algorithms. The results of this can be used to discuss the different advantages and disadvantages of each algorithm.

The 2 location algorithms that will be compared here are the Paget algorithm [36] and the Point Method [37]. Both of the location algorithms require at least 2 ΔT values found from the arrival times at 3 or more transducers. In this work the arrival time is determined by the threshold crossing method. In the previous section the advantage of using an additional ΔT value was shown for the Point Method and this applies to other location algorithms as well. Therefore the arrival times from the first 4 triggered transducers will be provided to both of the algorithms used in this comparison.

The Paget algorithm is a analytical method that assumes an elliptical velocity profile. This is defined by 2 velocities measured perpendicular to each other. To find the location a quartic polynomial equation is solved. This equation can give more than one real root and therefore more than one potential location. The implementation of the algorithm used here is the one used in the BALRUE system. In this implementation, if a third ΔT value is available, the triangulation is repeated with a different combination of ΔT values to determine which of the initial solutions is the correct location.

The second algorithm used in this comparison is the Point Method. This is a numerical search method. The ΔT times for positions throughout the plate are calculated theoretically and stored in an array. The location of a real AE event is found by finding the closest matching ΔT values in the array to those for the real event. The number of ΔT values that are used to find the closest

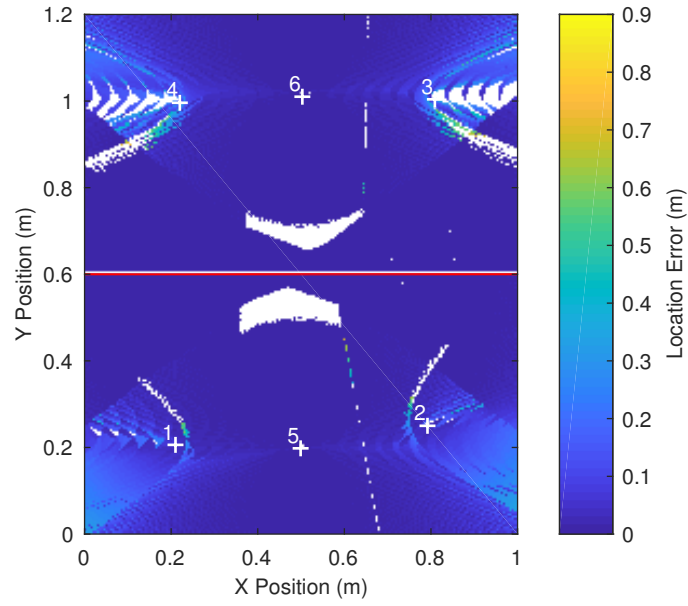
match can be 2 or more. In the previous section the benefit of using 3 ΔT values from 4 transducers was shown because it greatly reduces overlap in the ΔT array. This is a similar problem to having multiple real roots in the Paget algorithm.

To compare the different location algorithms they will be applied to 2 sets of arrival times generated by the model for 2 different structures. The 2 structures were the plate with a row of holes and the plate with a bolted L-section. Transducers 1 to 6 were used to ensure that at least 4 transducers were triggered by AE events at all possible positions. To compare fairly the 2 algorithms, the region covered by the ΔT array in the Point Method has been expanded outside of the structure by 0.5 m. This is to make it comparable with the Paget algorithm which does not use information about the extent of the structure. For this example it was found that the Paget algorithm did not locate any AE events further than 0.5 m from the outside of the plate. If the search region for the Point Method was limited to just the extent of the structure then the location accuracy would clearly be improved and results for this will be shown later. The ΔT array was calculated with a resolution of 1 mm between location points.

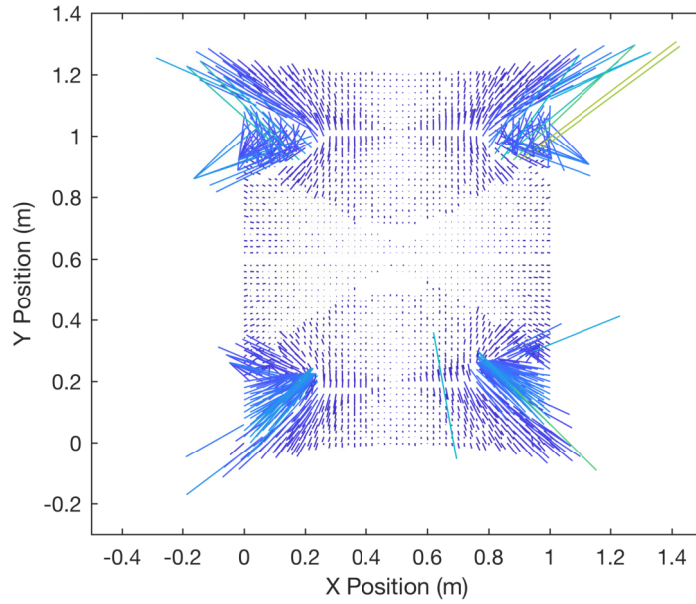
Plots showing the location error and location line plots for each of the structures and location algorithm combinations are shown in figures 5.8 to 5.11. The first thing to be noted is that the performance of each algorithm is very similar for both of the structures. This is the case for both the values of location error and the locations identified by the algorithm. The presence of a more or less attenuating feature does not significantly change location algorithm performance as long as the signal triggers the necessary transducers. This is because although the change in maximum amplitude caused by the more attenuating feature does affect where the first arrival crosses the threshold, the time difference is small. Therefore the ΔT values remain similar.

The second behaviour that can be seen is the Paget algorithm does not find locations for AE events at all positions in the plate. This can be seen in figures 5.8 and 5.10. At positions in the location error plots that are white, no real solutions to the location equation have been found. Therefore no source location can be identified. Some but not all of the regions where no location is found are on lines of symmetry between the transducers. This is where one of the ΔT values will be zero which reduces the number of possible roots to 2. The Point Method does not have this problem and will give a solution for any values of ΔT .

Excluding the positions where the Paget algorithm does not find solutions, it can be seen in all of the location error plots that both algorithms give good performance for AE sources located throughout the plate. The exception to this

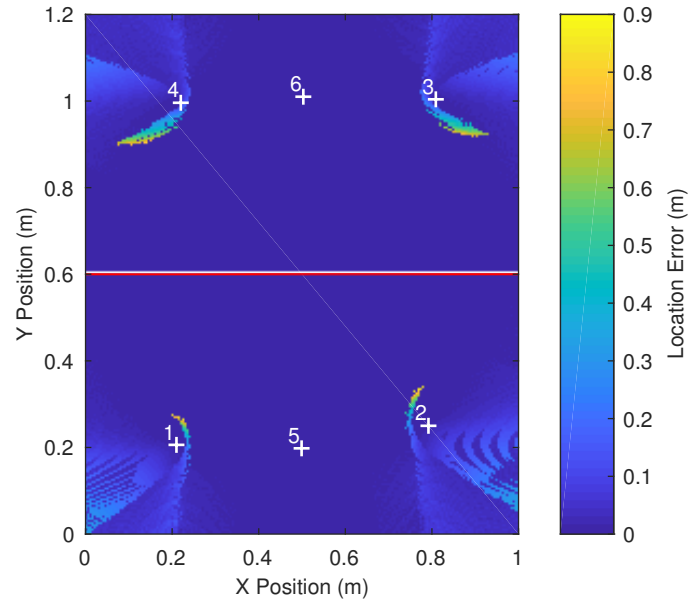


(a) The location error for AE events for a plate with a row of holes in the centre (red line). The location algorithm is the Paget algorithm using up to 4 transducers. Each pixel in the image represents an AE source location. The transducer locations are shown by white crosses.

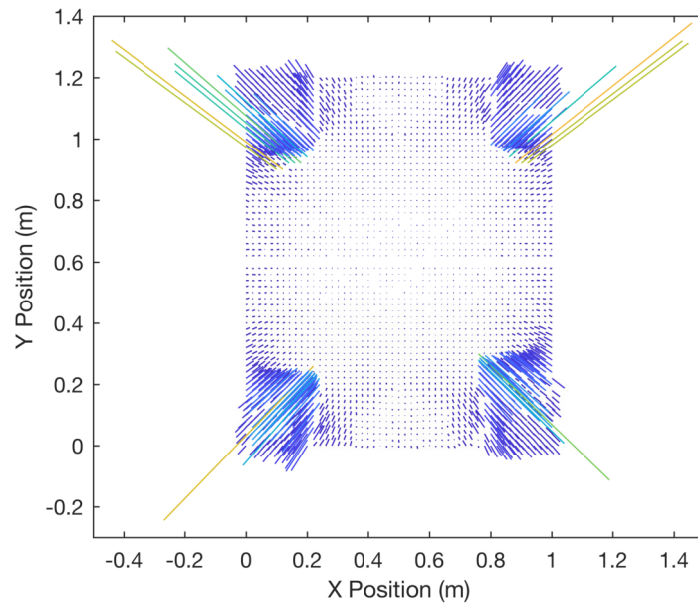


(b) The location line plot for the location algorithm and transducer arrangement shown above. One end of each line represents the true source location and the other shows the location determined by the algorithm. This figure shows a subset of AE source positions for clarity.

Figure 5.8

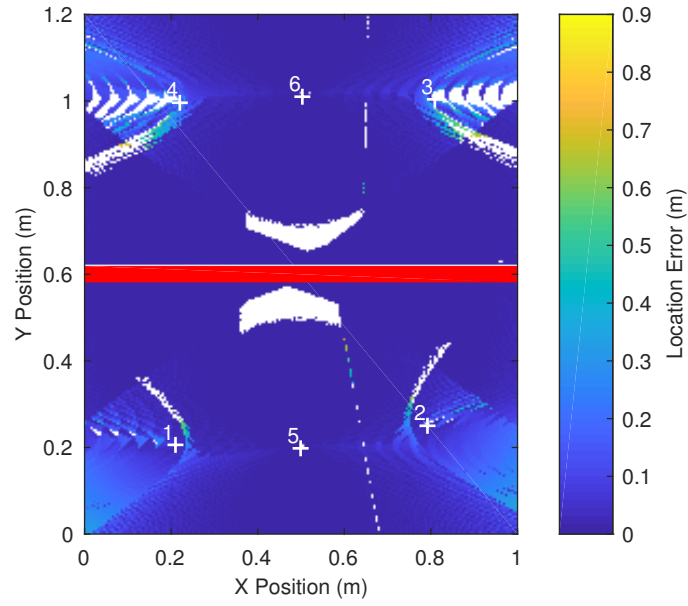


(a) The location error for AE events for a plate with a row of holes in the centre (red line). The location algorithm is the Point Method with an expanded search region using 4 transducers. Each pixel in the image represents an AE source location. The transducer locations are shown by white crosses.

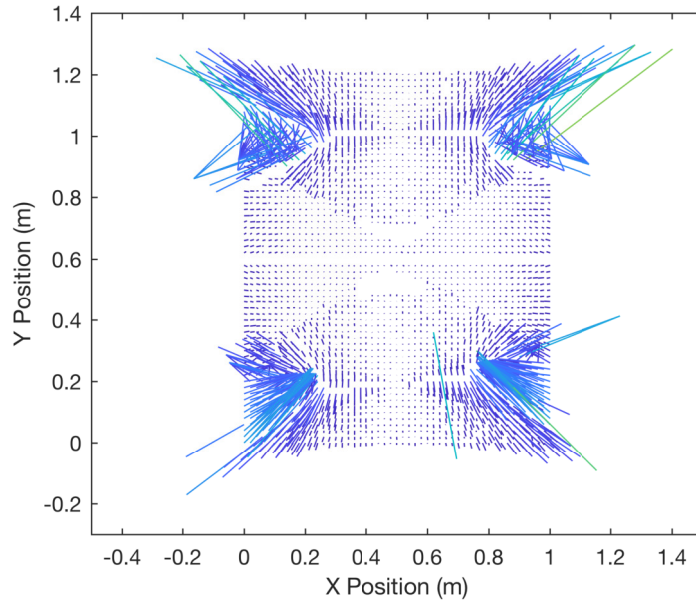


(b) The location line plot for the location algorithm and transducer arrangement shown above. One end of each line represents the true source location and the other shows the location determined by the algorithm. This figure shows a subset of AE source positions for clarity.

Figure 5.9

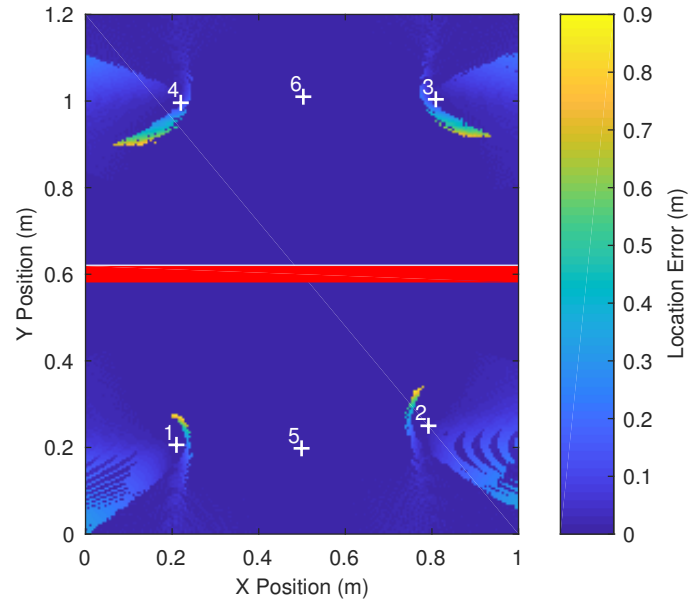


(a) The location error for AE events for a plate with a bolted L-section in the centre (red line). The location algorithm is the Paget algorithm using 4 transducers. Each pixel in the image represents an AE source location. The transducer locations are shown by white crosses.

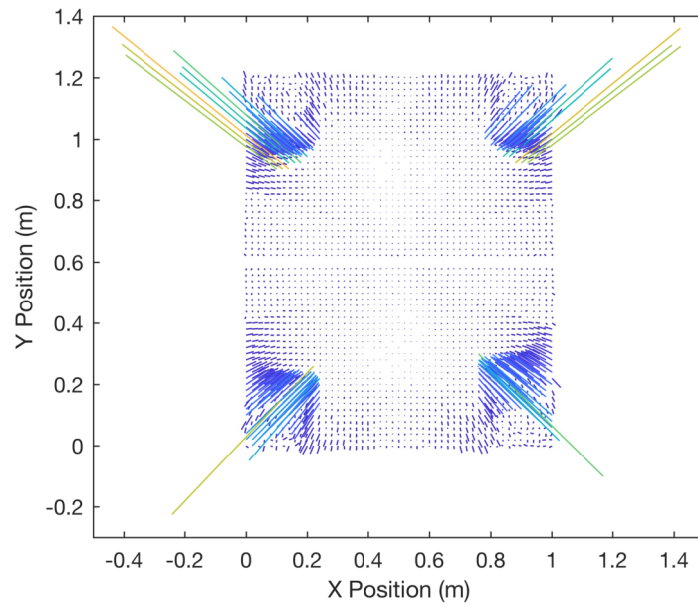


(b) The location line plot for the location algorithm and transducer arrangement shown above. One end of each line represents the true source location and the other shows the location determined by the algorithm. This figure shows a subset of AE source positions for clarity.

Figure 5.10



(a) The location error for AE events for a plate with a bolted L-section in the centre (red line). The location algorithm is the point method with an expanded search region using 4 transducers. Each pixel in the image represents an AE source location. The transducer locations are shown by white crosses.



(b) The location line plot for the location algorithm and transducer arrangement shown above. One end of each line represents the true source location and the other shows the location determined by the algorithm. This figure shows a subset of AE source positions for clarity.

Figure 5.11

Feature	Row of holes		Bolted L-section	
	Paget	Point Method	Paget	Point Method
Mean of all	3.268 cm	2.049 cm (1.872 cm)	3.514 cm	1.880 cm (1.536 cm)
Median of all	0.792 cm	0.424 cm (0.412 cm)	0.935 cm	0.447 cm (0.424 cm)
Mean inside transducers	0.892 cm	0.460 cm (0.273 cm)	1.009 cm	0.501 cm (0.295 cm)
Median inside transducers	0.411 cm	0.224 cm (0.224 cm)	0.461 cm	0.224 cm (0.224 cm)

Table 5.2: The mean and median values of location error for the 2 location algorithms on the different structures. The results in brackets are the values if the Point Method’s search region is restricted to the dimensions of the structure.

is the regions near to and outside of the corner transducers. Here the location error can be as large as 0.8 m though is generally less. Many of these points are located outside of the structure. Table 5.2 shows the mean and median values of location error for the different structures and algorithms. This confirms that the location error is generally small, especially within the area surrounded by the transducers. The maximum mean value is 3.5 cm which occurs for the Paget algorithm on the structure with a bolted L-section. The Point Method is more accurate by all measures than the Paget algorithm but the difference is small. The difference does however increase if the Point Method is restricted to searching within the structure where it performs the best. Both algorithms perform slightly better on the structure with the row of holes than the bolted L-section.

Given both the Point Method and the Paget algorithm perform similarly in terms of location error, the main distinguishing factor is that the Paget algorithm occasionally does not give a solution. On a real experiment it is likely that small variations in the ΔT values due to noise will mean some solutions are found in these no solution regions. However there would be a reduced count of events in these regions. One other factor to note is the Point Method is a significantly more computationally intensive location algorithm so where real time location is to be implemented the Paget algorithm or another analytical approach may be preferred.

This section has demonstrated how the model can be used to predict the performance of location algorithms for an AE setup on a structure. Once the performance of the location algorithms has been understood this could be used to choose the appropriate algorithm, improve the setup or identify where location performance may be poor to aid understanding results. The key parameter in determining how the location algorithms behave is the position of the trans-

ducers, not the affect of the geometrical features. Therefore for this application, the modelling effort could be tailored differently to the 2 previous examples.

5.5 Using the A_0 mode

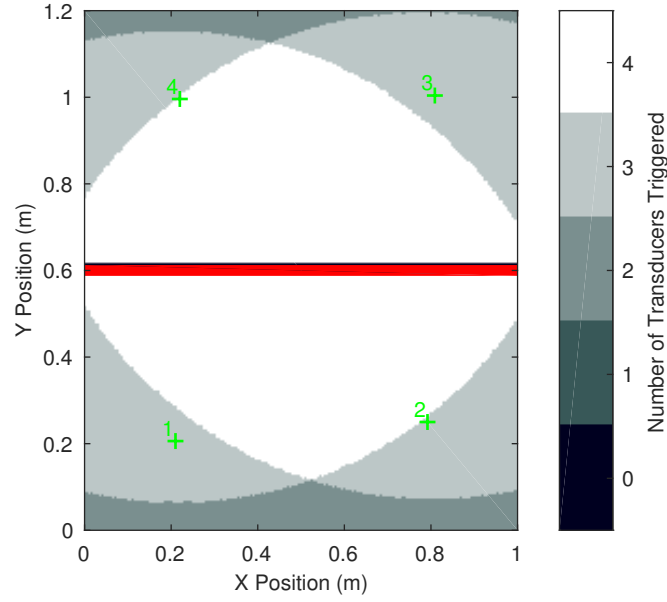
In the final example use of modelling the additional considerations necessary when using the A_0 mode will be demonstrated. At the frequency-thicknesses considered here, the group velocity of the A_0 mode is slower than the S_0 mode. This means it will not be the first arrival if the S_0 mode is of sufficient amplitude. However the amplitude of the A_0 source from the fatigue crack used in these examples is much greater than for the S_0 mode. The McWade NS3303 300 kHz transducers are also more sensitive to the A_0 mode than the S_0 mode. This means the A_0 mode has potentially a much greater range than S_0 .

To demonstrate this several modifications need to be made to the current construction of the modelling examples. The first is to include 2 modes in the overall system equation. All terms apart from beam spread will be specific to different modes. Therefore equation 5.2 becomes:

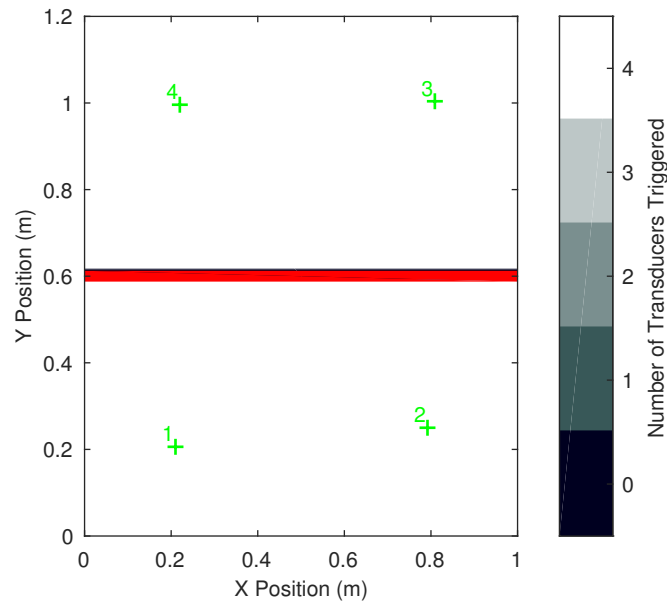
$$H(\omega) = B \sum_{modes} \left[S_E(\omega) R_X(\omega) P(\omega) \prod_{transmissions} T_C(\omega) \right] \quad (5.3)$$

As it was not possible to determine the A_0 transmission coefficient in any of the examples in chapter 3, a transmission coefficient from the literature must be used. The one chosen is that for a 25 mm bolted L-section measured by Scholey in [44]. In this the transmission coefficient was measured for both modes at incident angles from 0 to 45° at 15° intervals. This was done on a 2.5 mm thick aluminium plate at 200 kHz. The transmission coefficient was measured in both the frequency and time domains at each incident angle. The time domain values will be used here. In a similar approach to the 95 % quantile transmission models developed in chapter 3, the lowest value of transmission measured at any incident angle was chosen to give a single value of transmission coefficient. This gave a value of 0.72 for the S_0 mode and 0.32 for the A_0 mode.

To better demonstrate the advantages of the A_0 mode, a situation where the range of the S_0 mode is limited has been contrived. To do this only 4 transducers have been used and the threshold has been doubled to 5.77 mV. This is a feasible situation in a location with more background noise. The number of transducers triggered for each mode is shown in figure 5.12. This shows how the range of the S_0 mode has been limited. At all locations the S_0 mode will trigger at least 2 transducers but at many positions an AE source will not trigger sufficient transducers for location using the S_0 mode. Figure 5.12b



(a) S_0 mode



(b) A_0 mode

Figure 5.12: The number of transducers (green crosses) AE events at different positions will trigger for different modes on a structure with Scholey's bolted L-section (red line) centrally positioned. Each pixel in the image represents an AE source location.

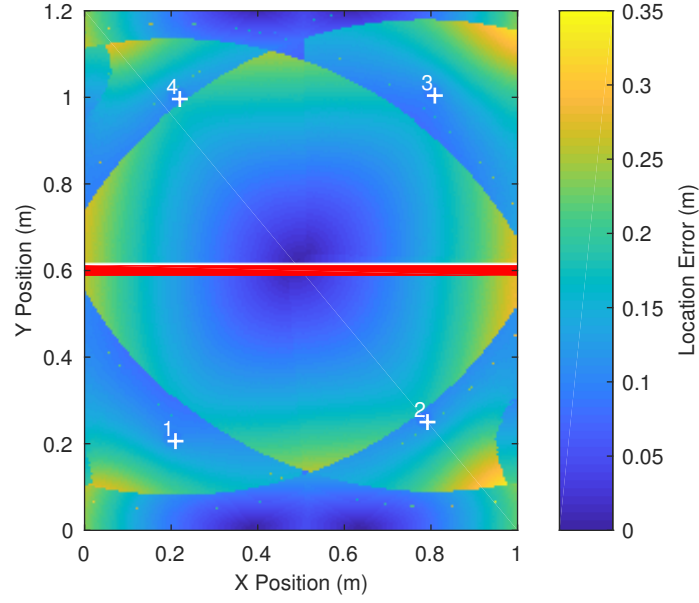
shows that the A_0 mode arrival will trigger all of the transducers for AE sources positioned throughout the plate.

If the A_0 mode had been assumed as the operating mode for this setup then the A_0 velocity at 250 kHz would be used for location. This has been done using the Point Method and the resulting location error is shown in figure 5.13a. It can be seen that the location error is quite high at many positions throughout the plate. This includes inside the area surrounded by the transducers where the location performance is normally excellent for the Point Method. The cause of the large values of location error is that the S_0 mode is triggering the transducers on at least some of the transducers. Therefore the ΔT values do not correspond to the velocities assumed for the location algorithm.

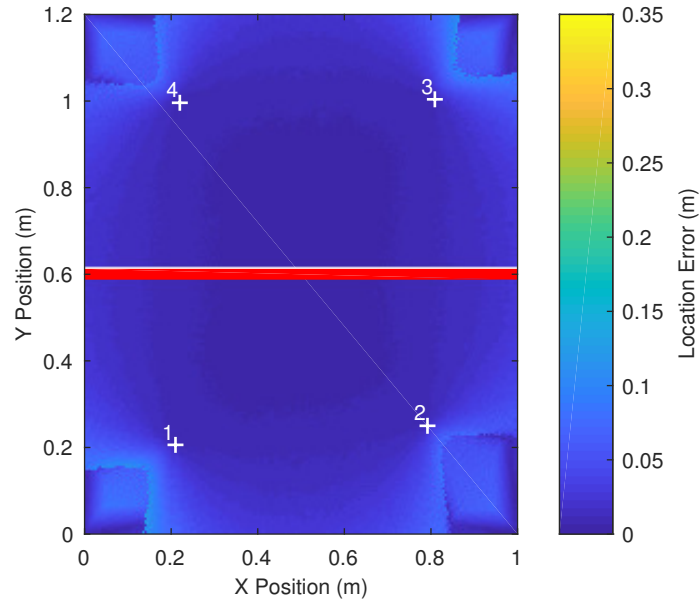
There are several potential ways to solve this problem and still use the range of the A_0 mode. These include using transducers that are even more biased in sensitivity towards the A_0 mode, using a location algorithm that considers both modes such as the algorithm presented in [78] or raising the threshold higher to reduce the influence of the S_0 mode. The last of these suggestions will now be demonstrated. The transducers and AE sources are modelled as a point source or receiver. The beam spread is therefore $\frac{1}{\sqrt{d}}$ where d is the distance between the source and the transducer. This means the amplitude of the signal rises exponentially as the distance between the source and receiver decreases. Therefore the amplitude of the S_0 mode is comparatively large when the source is close to the transducer. This means finding a threshold where the S_0 mode does not trigger any transducers and the A_0 mode can be detected at all positions in the plate is impossible. Instead a balance must be found where the early triggering by the S_0 mode does not significantly affect location accuracy.

To do this the maximum amplitude of the S_0 arrival was found for where the source was 1 cm from the transducer. This value was 0.108 V and was set as the threshold. This means there is only a small region close to the transducers where the S_0 mode arrival triggers the transducer. This is shown in figure 5.14. The S_0 mode therefore has little effect on the ΔT values. For this threshold the A_0 mode still triggers all 4 transducers no matter where the AE source is positioned in the plate. The location error for this threshold using the A_0 mode is shown in figure 5.13b. It can be seen that the location error is generally very small except for in the regions behind the transducers where the Point Method is known to perform poorly.

This section demonstrates how using this modelling approach can determine what problems will occur when using the slower A_0 mode. These problems are caused by triggering on the faster S_0 mode when that is not desired. This problem can be mitigated simply by raising the triggering threshold on the AE system but that will have other effects on the overall system performance, most



(a) 5.77×10^{-3} V threshold



(b) 0.108 V threshold

Figure 5.13: The location error for AE events for a plate with Scholey's bolted L-section in the centre (red line). The location algorithm is the point method using 4 transducers with 2 different thresholds. Each pixel in the image represents an AE source location. The transducer locations are shown by white crosses.

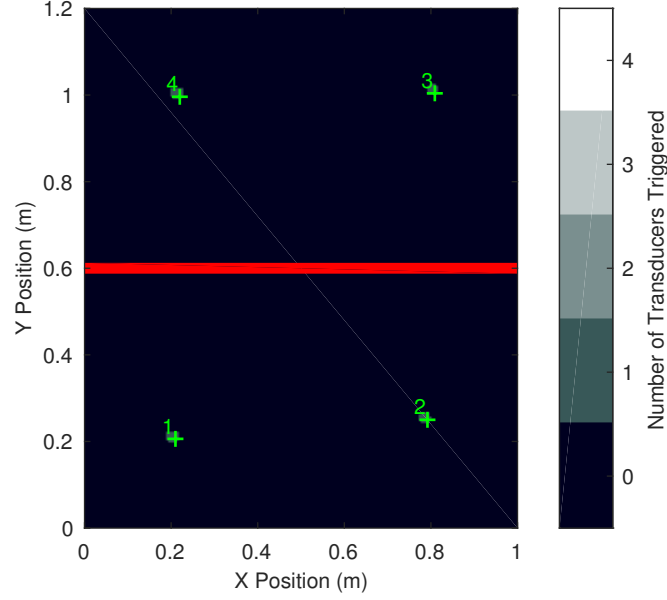


Figure 5.14: The number of transducers (green crosses) AE events at different positions will trigger on the structure with Scholey's bolted L-section (red line) centrally positioned. This is for the S_0 mode with a raised threshold. Each pixel in the image represents an AE source location.

particularly on the range the A_0 mode can be detected. It should be noted that this is one example use of the modelling where the conservative assumptions for transmission may be detrimental. This is because it may be important to know the upper range of the S_0 mode so more accurate modelling or even over estimation of the transmission over features may be required for this mode. This is likely to only be a consideration over longer propagation distances in which case the first reflections of the faster S_0 mode may need to be considered. This would be a possible addition to the overall system model but has not been done here as the focus has been on the S_0 mode.

5.6 Conclusions

In this chapter example uses of the overall system model have been demonstrated. This model contains components from the work on AE sources and transmission models described in chapters 2 to 4. The model has been used to find the number of transducers which will detect an AE event, demonstrate the effect of transducer positioning and number of ΔT values on location performance, show how different location algorithms can be compared and assessed and

demonstrate some of the additional considerations when using the A_0 mode. These are all behaviours to consider when designing an AE system or understanding the results of existing systems. This modelling approach has the ability to be a tool to aid those processes. All of these examples have been deliberately shown on simple structures to highlight the factors in each more clearly. The advantages of using forward modelling are likely to only increase as the structural complexity increases and resulting effects on system performance become less intuitive.

Another advantage of the LTI systems modelling approach is the low computational demands of the technique. In many of the figures shown in this chapter thousands of AE events at different locations have been modelled. All these models have been run on personal computers with simulation times significantly below 10 min. This approach to modelling AE systems has compromises on accuracy to enable it to be implemented with limited resources. This chapter demonstrates how despite this it can be used usefully as a tool as long as the underlying conservative assumptions in the model are understood. For greater accuracy significantly more resources and time would need to be expended which is unlikely to be necessary for many of the applications of a forward model during development of such systems. It is hoped that this modelling approach provides a sensible balance between resources and accuracy whilst remaining a useful tool.

Chapter 6

A Design of Experiments Based Data Collection Approach

To validate models of guided wave propagation in structures it is necessary to gather experimental data to test the modelling results against. In the validations of different transmission models shown in chapter 4 a line of experimental measurements was used. This line was arranged at a position to ensure the waves propagated across the features at a comprehensive selection of incident angles when the signals from the source to multiple different transducers were collected. During this work, what the next step would be for a more comprehensive validation was considered. The obvious extrapolation from a line was to move the simulated AE source over a 2D area instead of a line. A few attempts to do this were conducted but it was quickly found that this was very time consuming for the areas considered. This was especially the case because the spatial resolution of the measurements needed to be high to show any additional information over the line based validation experiments. On the relatively simple structures used for validation in chapter 4 this was especially the case. These activities did however raise the question of how to perform a comprehensive 2D experimental validation with a reduced number of collection points to reduce the experimental effort. This could be used to validate this modelling approach on more complex structures or more generally to validate guided wave propagation models on structures of high complexity.

The type of experimental work considered here is similar to that used in chapter 4. The data is collected using a EMAT as a proxy for an AE source. An EMAT has the advantages that it can be easily be moved from one meas-

urement position to the next, it has very consistent coupling and its sensitivity is reasonably omnidirectional. It has the disadvantage of a low transduction efficiency when compared to piezoelectric based transducers. This means the combination of a narrowband chirp signal [77] and averaging multiple measurements is required to get a received signal with a sufficiently high SNR. The areas over which measurements are required are relatively large, in the order of 1 m^2 , and the EMAT is positioned manually. The pitch between measurements can be required to be as small as half a wavelength. This combination of measurement time and positioning time means each measurement is relatively time consuming. Depending on the background noise level, measurements can take 1 to 3 minutes. This situation has led to investigations on how to reduce the time to conduct the whole data collection, resulting in the development of an iterative data collection approach. This algorithm is based upon DoE principles.

The first part of this chapter explains the background to the technique. This is followed by an explanation of the algorithms operation and implementation. In the final part of the chapter the algorithm is tested on a simulated dataset and a experimental dataset.

6.1 Background information

The most common experimental design is grid based, also known as a raster scan. This is a type of geometrical experimental design. Here measurements are taken at a certain pitch which is constant across the measurement space. This method comprehensively covers the measurement space but is the most time consuming permutation. Alternative geometrical experimental designs exist including Fractional Factorial and Latin Hypercube [79]. These types of experimental design reduce the number of sampling points and therefore time required but do not consider the process output in choosing these points. Given the features of interest in the target application are in small regions, these techniques are unlikely to sample at a sufficient resolution in these regions.

Another common group of experimental design techniques is optimal experimental designs. Here a model of the output is assumed and the sample points are chosen to minimise a certain type of variance of this output [79]. These type of experimental designs reduce the number of sampling points required but require a model type to be assumed. This model type is normally a simple polynomial model, which is unlikely to fit the output response in this application, but can be a more specific model. Given that the results collected by this algorithm will be used to test a model of guided wave propagation, it is preferable not to have to predict another model of the response. If this was done there is a risk of missing unexpected results and conformational bias in

the chosen sampling points.

For the experiments described above, much of the structure is a plate of constant thickness. Here the wave propagation is influenced by beam spread and attenuation, both of which are well understood. Therefore measurements in the centre of plates are generally not showing interesting information and these regions can be sampled less densely. Geometrical features are likely to have a more significant effect on the wave propagation [70] so measurements in these regions are of more interest. Denser sampling is therefore required in these regions. To achieve this without making assumptions about the response requires the use of another type of DoE approach; an experimental design with an active learning step.

The algorithm chosen here is the *Hierarchical local model tree* for *Design of Experiments* (HilomotDoE) [79, 80]. The operation of the algorithm will be described in detail in the following section but it consists of a set of local models which are fitted to subsets of the dataset. These local models are adaptive in size and resolution and the local model which worst fits its dataset is improved on each iteration by collecting more data. This means the algorithm will collect data points where changes are present which should correspond to the regions where the guided wave amplitude is changing. It will collect less data points in regions where the amplitude is constant or changing linearly. This is the desired collection behaviour of collecting fewer points but the most relevant points.

The next section will describe the details of the algorithm and then the following sections will demonstrate the algorithm on simulated and experimentally collected data.

6.2 Algorithm operation

The algorithm operates in the following way:

- First a seed dataset is collected which sparsely covers the region to be measured.
- A model, which can be of any type, is fitted to the dataset to give a global model. The same type of model is used throughout the algorithm. The Root Mean Squared (RMS) difference between the global model and the data set is calculated.
- If this global model difference is too large, the model is refined by splitting the model in half. The optimum split is found so that the two new local models created have the minimum difference between the model and the experimental results. The partitioning strategy is based upon the one

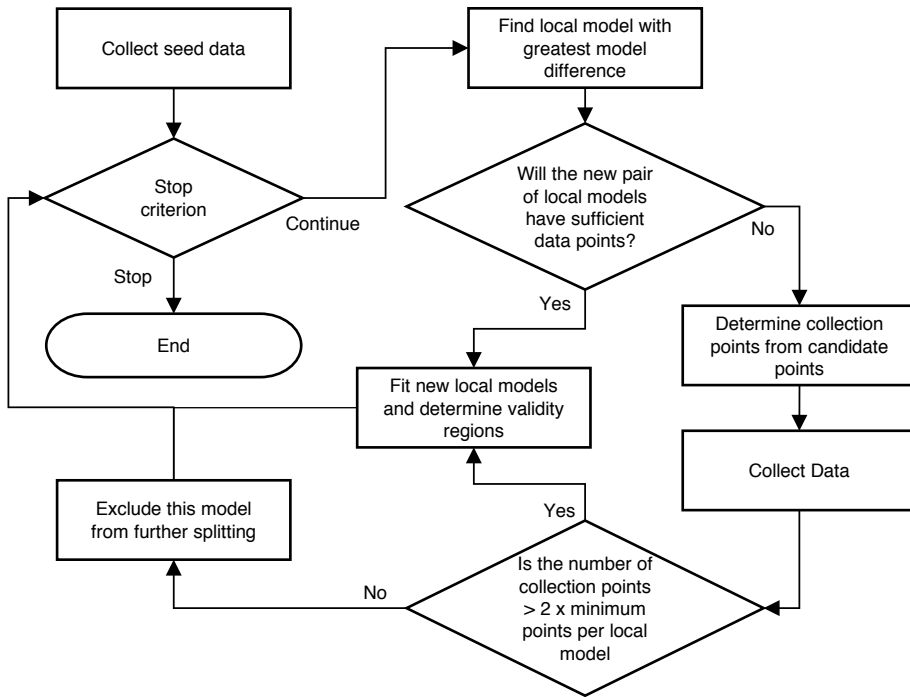


Figure 6.1: Flow chart showing the operation of the data collection algorithm.

described by Nelles in [81]. A minimum number of points per local model is defined and if the new local models to be created will not have sufficient points, more measurements are made prior to the split being calculated.

- A new global model is formed from the local models and the validity functions created by the partitioning strategy. The global model difference is recalculated and if refinement is still required then the local model with the worst error will be split in half.
- The iterations continue until a stop criterion is met. This could be convergence of the model difference or a maximum number of samples to take.

6.2.1 Algorithm implementation

The implementation of the algorithm used to collect data for this report will now be explained including the deviations from the HilomotDoE algorithm explained above. The operation of the data collection algorithm is shown in figure 6.1.

Collect seed data

A minimum resolution is defined by the size of the smallest feature of interest. It is important to have at least one sample point on each feature

otherwise the algorithm may not choose that region to collect more points and therefore the feature would be missed. The minimum spacing between points is used to define an initial set of sample points at which measurements are taken. The points are determined by the modified pseudo-Monte Carlo sampling algorithm explained below.

Stop criterion

The decision whether to continue can be based upon many factors including the time available for experimentation, a threshold on the value of model difference or the convergence of the model difference. In this work a threshold will be used but further work is required in this area.

Find local model with greatest model difference

To determine which local model is to be split, the local model with the greatest RMS model difference is found. This is the criteria used to determine which local model least well represents the underlying process.

Determine collection points from candidate points

When a model region is to be split into two local models, new data collection points are required if there will not be sufficient points in the two new models to satisfy the defined minimum number of points per model. It is necessary to have a minimum number of points per model to ensure that the model does not become over-fitted which would damage the validity of the model difference calculation. The new collection points are chosen from a list of candidate points which are determined by a user defined resolution which will be half the minimum wavelength of the frequency range of interest in most cases. The candidate point chosen is that with the greatest nearest neighbour distance to the already collected points. This is repeated until the necessary number of new candidate points have been defined. This method is used so that the points picked are well spaced and is inspired by the pseudo-Monte Carlo sampling algorithm in [79] but with a more constrained set of candidate points. If multiple points have an equal greatest nearest neighbour distance then one of these points is chosen at random. If there are not sufficient available candidate points to satisfy the minimum number of points per model then the available points are collected and the local model is excluded from further splitting.

Collect data

The ultrasonic time traces for each transducer in the array is collected and saved for each measurement position. The variable of interest is then calculated from the time trace. In this case this is the maximum amplitude of the first arrival.

Fit new local models and determine validity regions

The best pair of local models is found by minimising the RMS model difference for the two new local models. First the validity functions for each new region are calculated. The split is constrained to pass through the centre of the points to ensure that they are split in half and therefore each new local model satisfies the minimum number of points per model. Then the best fit model is found for the data. The model type used here is a hinging hyperplane [82]. This is a pair of planes which meet at a line like a piece of paper with a single fold. Hinging planes are used because they do not fit well over discontinuities, for example the amplitude drop as the guided waves travel over a feature, and therefore force data collection in this region. An iterative search is performed to find the optimum pair of validity functions. This and the corresponding local models are included in the global model. The local model they replace is removed from the global model.

The exception to this procedure is the first iteration. Here the global model consists of one local model which is valid everywhere. Because there is no split between models, the local model is a plane fitted to the data and not a hinging hyperplane.

6.3 Example on simulated data

First the algorithm will be applied to a simulated dataset to demonstrate its performance. The advantage of using a simulated dataset is that the full raster scan can be generated in a short period of time, negating the issue which the algorithm aims to address. The structure modelled is that used to validate the bolted L-section results in section 4.3. The structure is shown in figure 6.2. It consists of a 3 mm plate which has had 2 L-section stiffeners bolted to it. The wave propagation in the structure was modelled using the same methodology as was used in chapter 5. Each of the direct ray paths from the AE source to the receiving transducer was modelled for the S_0 mode. The conservative transmission model was used to model the bolted L-section stiffeners. The excitation signal was a 5 cycle 200 kHz Hanning windowed tone burst. The raster scan image of the S_0 first arrival amplitude is shown in figure 6.3. Here the effect of beam spread has been removed because this is a predictable asymptotic relationship.

The algorithm has been applied to the simulated structure and it picks locations from the raster scan iteratively, as it would request measurements to be made during a real experiment. Components within the algorithm are random

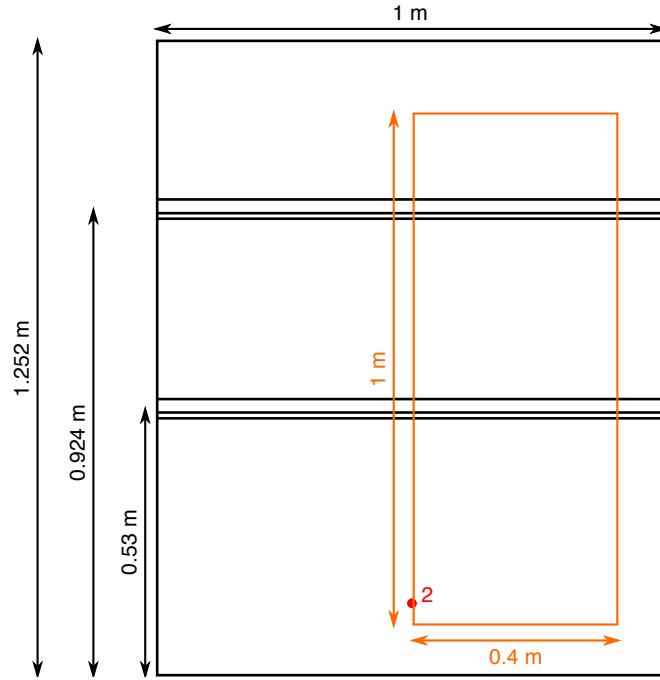


Figure 6.2: Diagram of simulated experiment including the receiver position (red circle), source locations (within the orange rectangle) and L-section stiffeners.

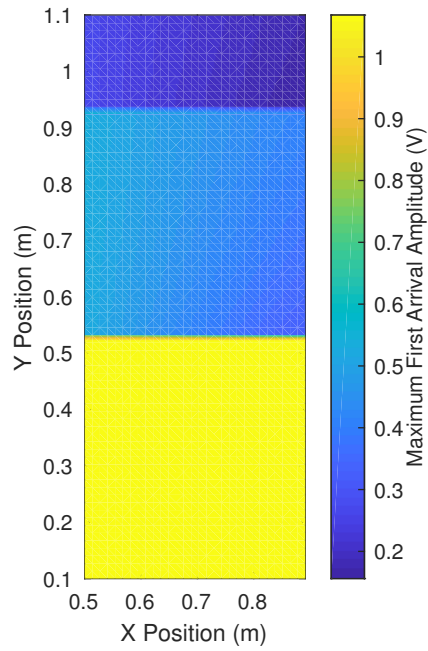


Figure 6.3: The amplitude of the first S_0 arrival on the plate with 2 L-section stiffeners after the effect of beam spread has been removed.

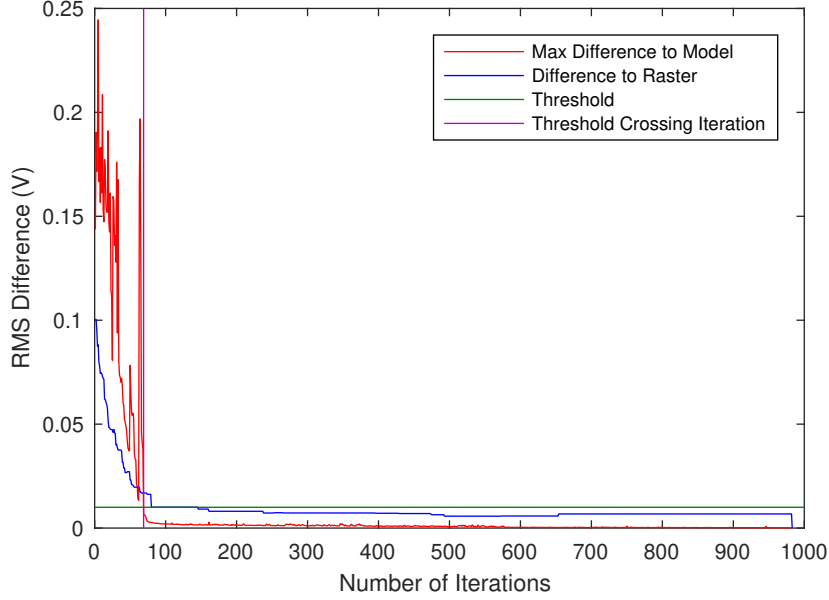


Figure 6.4: How the difference of model to sparse dataset and raster scan to sparse dataset changes as the algorithm progresses. This is the result for a simulation of a single experiment.

and because the full raster scan is available, the algorithm will be run over the same dataset multiple times to check the convergence of the model difference is consistent. This is the metric that informs the stop criterion so reliable convergence of this value is required for the algorithm to be successfully applied. The target number of points per local model was set to 12 because this was found by trial and error to perform well.

6.3.1 Convergence of model difference

Figures 6.4 and 6.5 show how the difference between the sparse dataset collected by the algorithm at that iteration to the values predicted by the model change as the number of iterations the algorithm is applied increases. This is for one run of the algorithm and multiple runs of the algorithm respectively. The difference to model is calculated at each point in the full raster scan and where data has not yet been collected in the sparse dataset, the value is found from a linear interpolation, base upon a triangulation. From this the RMS difference is found for each local model. The maximum RMS difference across the local models is then found and this is the value shown in figure 6.4. If all possible points in a local model are collected it is excluded from this calculation. The algorithm has been run with no stop criterion and therefore eventually collects all available

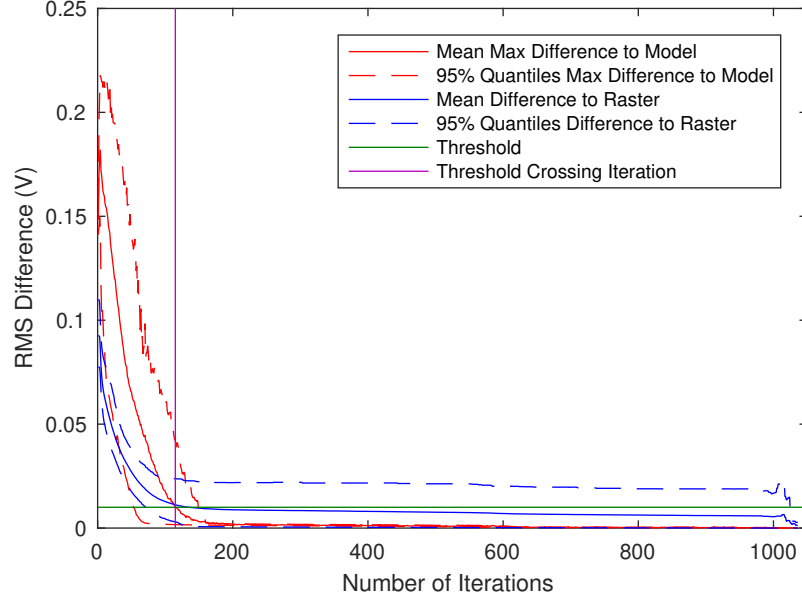


Figure 6.5: How the mean difference of model to sparse dataset and raster scan to sparse dataset changes as the algorithm progresses. The results here are from 924 simulations of the same experiment.

points. It can be seen that the maximum RMS difference to model decreases to a very small value prior to 100 iterations. The value decreases in quite a chaotic way as refinement of the model discovers larger differences than were previously present in the sparse dataset. No significant difference is present after 100 iterations. The RMS difference between the sparse dataset and the raster scan decreases in a similar way. This information is not known to the algorithm as it requires a full raster scan to be measured but demonstrates how well the sparse dataset represents the full raster scan. The difference to raster converges at a similar number of iterations to the difference to model showing that this is a good metric to base the stop criterion upon. The difference to raster converges to a value of $6.79 \times 10^{-3} \text{ V}$ until the very end of the algorithm operation when it goes to zero. This is because of errors in the interpolation from the sparse dataset which are only corrected once all points are collected. This difference is acceptably small when considering the amplitude of the signals. The maximum first arrival amplitude varies between 0.156 to 1.068 V once beam spread has been removed.

The algorithm has been applied to this simulated dataset 924 times. The maximum model difference has been found for each run and the mean and 95 % quantiles of this value can then be found. This is shown in figure 6.5. It can

be seen that the behaviour of the difference to model and difference to raster are similar to that of the single run but mean convergence occurs at a slightly higher number of iterations. Both variables converge at a similar number of iterations confirming that the difference to model is a good metric to base a stop criterion upon. It should be noted that each run of the algorithm stops at a different number of iterations so the greater variability in the quantiles at the largest number of iterations is caused by a smaller sample size.

6.3.2 Threshold as a stop criterion

One proposed stop criterion for the data collection is a threshold on the maximum difference to model. A threshold of 0.01 V was set which is approximately 100 times smaller than the maximum first arrival amplitude. This was deemed to be a sufficiently small error. In the single run of the algorithm on the simulated dataset, shown in figure 6.4, the iteration where the threshold was crossed was 69 which corresponds to 600 data points collected out of a possible 5040 which is 11.9 % of the total number of points. Across the 924 runs of the algorithm, shown in figure 6.5, the mean number of data points required to reach the threshold was 870 which is 17.3 % of the total number of points. This is a significant reduction in the number of points that need to be collected and therefore a significant reduction in total experiment time.

Other potential stop criteria exist and it is believed it would be worth investigating a stop criterion based upon the convergence of the maximum difference to model. This would potentially remove the requirement to define a threshold which currently has to be done intuitively from an estimate of the signal amplitude.

6.4 Example on experimental data

The algorithm will now be applied to an experimentally collected dataset to demonstrate its performance on real signals which contain noise. The dataset is a raster scan collected on a section of A320 wing skin. A roving EMAT transducer was used as a repeatable representation of an AE source. It was excited with a 250 kHz 5 cycle Hanning windowed tone burst. Due to time constraints the region was sampled at 20 mm in the x direction and 40 mm in the y direction. This is a larger spacing than a half wavelength of the centre frequency of excitation. The wavelength at 250 kHz on this sample is approximately 25 mm. The collection region is shown in figure 6.6 and the amplitude of the first arrival after beam spread has been removed is shown in figure 6.7.

As was done with the simulated plate with 2 L-section stiffeners, the al-

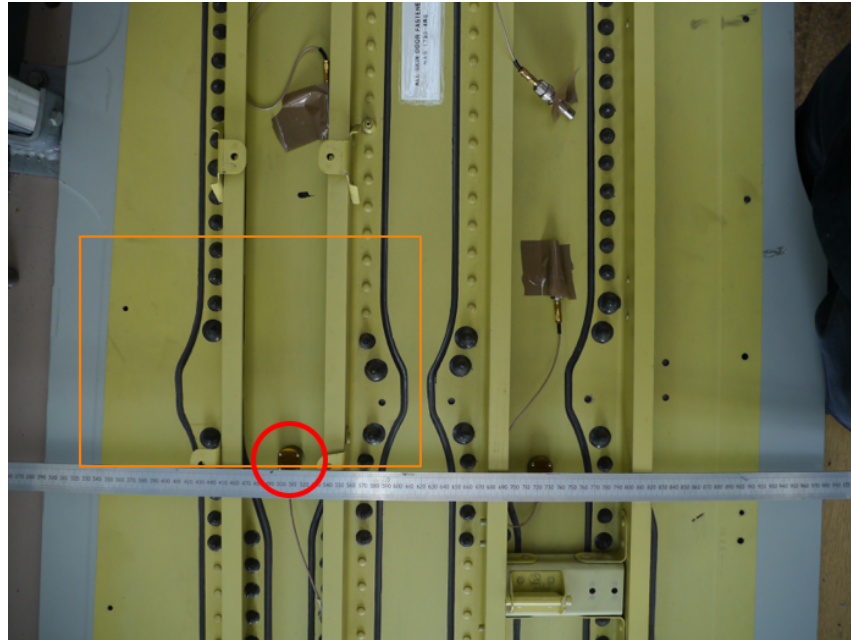


Figure 6.6: A diagram of the collection region (inside the orange rectangle) and receiver position (red circle) on a section of A320 wing skin.

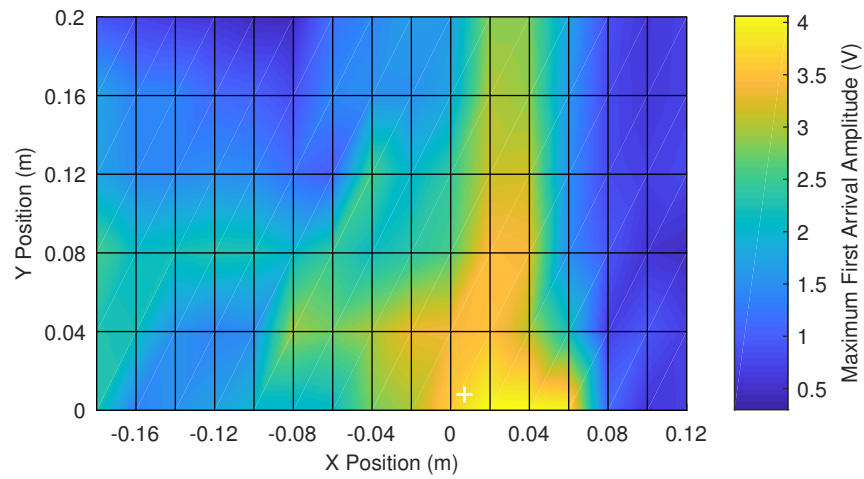


Figure 6.7: The amplitude of the first S_0 arrival on a section of A320 wing skin after the effect of beam spread has been removed. The white cross shows the receiving transducer position.

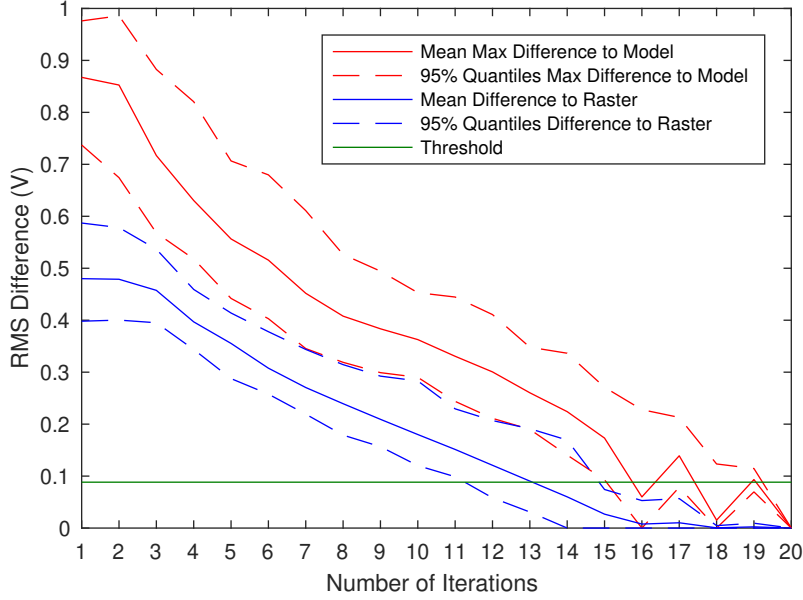


Figure 6.8: How the difference of model to sparse dataset and raster scan to sparse dataset changes as the algorithm progresses. The results here are from 100 runs on the same experimental dataset.

gorithm has been applied to this dataset multiple times to get a clear understanding of how it behaves. The algorithm was applied 100 times to the dataset and the mean and 95 % quantiles can be seen in figure 6.8. The target number of points for local models was set to 9. This was found to perform well on this structure with a high feature density. A threshold was defined by the RMS value of the noise in the experimental signals and this was 0.0883 V. The RMS value of the noise is a suitable value for the threshold because the difference to each local model cannot be better than this. Collecting more points after this threshold is reached is not likely to reduce the model difference further.

It can be seen in figure 6.8 that the mean maximum difference to model and mean difference to the full raster scan decrease in a similar pattern as the results from the simulated dataset. Both values decrease at a similar rate. However these values do not converge to a constant value prior to all data points having been collected. The mean maximum difference to model decreases to the threshold value at a similar point to where some of the runs have finished and the mean value is becoming more erratic due to the small number of runs which get to this high a number of iterations. The algorithm would therefore only have stopped in a small number of runs. The values do not converge because of the higher feature density in this sample and that it is sampled less densely.

This is a demonstration of where the algorithm will not reduce the number of points to be collected and a full raster scan is required, which is what would have had to be collected without this technique. The results still suggest that the mean maximum difference to model is a suitable metric for a stop criteria.

6.5 Conclusions

To validate guided wave models of AE systems, especially on structures with a high feature density, it may be necessary collect simulated AE signals over a 2D area. This is a very time consuming task for large areas or when sampling at a high spatial resolution. To reduce this time the HilomotDoE algorithm has been applied to determine data collection points. This aims to minimise the number of data points collected compared to raster scans. In this implementation the algorithm collects data points in regions where the first arrival amplitude does not fit plane models well. This is typically the case at features such as stiffeners so more data points are collected here than in parts of the structure which are just plate. This is the desired behaviour because the guided wave propagation is simple to model in the plate regions and the effect at features is of more interest in validating that model. To achieve this compensation for beam spread needs to be applied to the received signals.

The algorithm has been applied to both a simulated dataset with 2 bolted L-section stiffeners and a section of A320 wing skin with stringers. In both cases the maximum RMS difference to the model of the response and the RMS difference between the sparse dataset and the full raster scan decrease in a similar way. This suggests that the maximum RMS difference to the model is a suitable metric to base a stop criterion upon and a threshold stop criterion has been demonstrated on the simulated dataset. The feature density on the A320 wing skin means that a full or nearly full raster scan is required so a stop criterion cannot be tested here. With the threshold stop criterion there is an average reduction in the required data points of 82.7% compared to the full raster scan for the simulated dataset.

This approach to data collection has potential to significantly reduce the amount of data points collected and therefore total experimental time in guided wave measurement. The amount of time saved is dependent on the density of features in the structure. It does this in a way which requires no knowledge of the guided wave behaviour in the structure being measured which is a advantage in both simplicity and that it prevents conformational bias in selection of measurement points. Here this algorithm has been applied for a very specific need but it has potential to reduce the number of data points collected in other NDT applications where measurement time is large and parts of the response

are predictable.

Chapter 7

The Long Term Performance of Guided Wave Systems

It is common for aircraft to have lifetimes exceeding 25 years [4]. Therefore if GWSHM systems are to be used to monitor in service aircraft they must be able to reliably operate for at least this time period. If the system fails or starts to produce a high false call rate then it could cause unacceptable aircraft unavailability which would cause high costs. This could quickly damage trust in use of GWSHM systems. Therefore understanding the long term performance of these systems is imperative for their use in this type of application.

The work in this chapter is pertinent to both AE and active GWSHM methods. The experimental work in this section has been performed using an active GWSHM system but the effects discussed are applicable to both methods, although the effects on overall system performance can differ. Both methods use the same guided wave propagation to detect damage and use very similar transducers and other hardware. An introduction to and description of the difference between the 2 types of system can be found in section 1.3.

The majority of GWSHM experiments and tests occur over a short period of time. Anecdotally their performance degrades over time and this needs to be understood so that any ageing effects can be prevented or compensated for. If this is not done then there is a risk that the information the system delivers is incorrect and this is potentially dangerous. There has been little work on this problem with exception of work by Attarian *et al.* [83]. This looks at how an active GWSHM system bonded to an aluminium plate performs over a period where it is subjected to 150 thermal cycles. It was found that the size

of reflection from a defect which could be reliably detected had approximately doubled over this period due to an increase in the coherent noise in the received signals. It was hypothesised that this degradation in performance was caused by changes in the adhesive bondline between the transducers and the structure. This was indicated to be the case by finite element modelling and experiments on bulk adhesive samples.

This chapter discusses results collected from an active GWSHM system that has been operating for more than 3 years in real environmental conditions. This dataset will therefore demonstrate the changes that occur and the challenges of operating a system of this kind over a long time period. The first part of this chapter will describe different methods of processing the signals received from an active GWSHM system. These predominately exist to compensate for temperature changes. Next the experimental setup will be described and then this will be followed by an analysis of the changes in signal parameters. The performance of different baseline subtraction techniques will be demonstrated. The implications of these results for both active GWSHM and AE systems will then be discussed.

7.1 Baseline subtraction and temperature compensation techniques

A major challenge for the successful operation of active GWSHM systems is that the velocity of guided waves are temperature dependent. This means that the wave propagation in a real structure will change as the structure is subjected to different environmental conditions. The structure may also change over time due to wear and environmental exposure although these changes will occur over much longer time scales than the changes caused by temperature. These effects combine to mean the wave propagation in the structure is never identical. A typical method of interpreting the signals collected using active GWSHM systems is baseline subtraction. Here a signal collected at a time when the structure is known to be good is used as a reference signal and is subtracted from the recently collected signal. The reference signal is referred to as the baseline signal. The theory behind this technique is that if any damage to the structure has occurred it will change the wave propagation and therefore the recently collected signal. When the baseline signal is subtracted from the recently collected signal the theory is that only reflections from the new damage will remain in the residual signal. This will enable the damage to be detected, located and imaged. However due to the environmental factors mentioned above, subtraction is never perfect and the residual can contain waveforms that may appear like damage

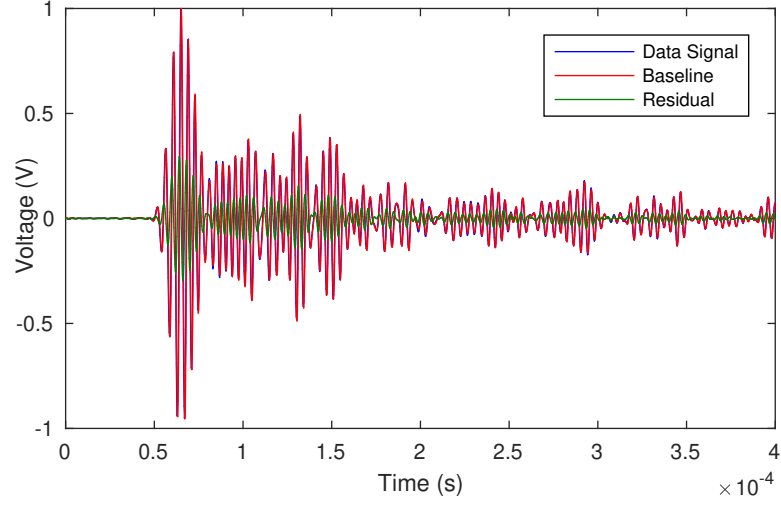


Figure 7.1: An example of baseline subtraction performed with 2 signals from the same transducer pair from the water tank dataset. Neither signal contains reflections from damage.

reflections but are in fact just artefacts of an imperfect subtraction. An example of this is shown in figure 7.1. To counteract the temperature dependent velocity of guided waves, temperature compensation techniques have been developed for active GWSHM systems. These include Optimum Baseline Subtraction (OBS) and the Optimal Stretch Method (OSM) [12, 84].

In OBS multiple baseline measurements are collected over the operational conditions of the structure whilst it is assumed to be undamaged. The operating conditions need to include both the environmental conditions the structure will operate in and the possible loads that can be applied [85]. For each collection, all of the baselines are subtracted individually from the collected signal and the closest matching baseline is used. The closest matching baseline is typically determined by either the maximum or RMS value of the residual. It is anticipated that the baseline that produces the smallest residual value will be the baseline that has the most similar environmental conditions. This is likely to hold true even if damage has occurred, unless it is gross damage, by which time a GWSHM system is unlikely to be necessary to identify the damage.

The OSM is designed to compensate for the change in velocity caused by temperature changes. The signal is stretched or compressed in time compared to the baseline signal until the best matching stretch is found. The baseline is then subtracted from the best stretched signal. The range of temperatures this technique can successfully compensate for has been reported to be between 1 and 5 °C [86]. The performance degrades with increasing signal complexity and

multiple modes where a stretch based on a single velocity is no longer a good assumption. The OSM is often combined with OBS to allow a large range of environmental conditions to be covered with a smaller baseline set.

A challenge in implementing OBS is that, for a real structure, it is very difficult to comprehensively cover all environmental conditions whilst also ensuring the structure is undamaged. A related approach to deal with this challenge, the Continuous Baseline Growth (CBG) algorithm, has been suggested by Putkis *et al.* [87]. This is an online baseline collection method which removes the need to assume the structure is undamaged for a baseline collection period. For each transducer combination, the first signal collected is used as the first baseline in the baseline set. OBS is then applied for the subsequently collected signals and if the residual value is larger than a defined threshold, it is added to the baseline set. The concept is that the residual value will be larger than the threshold if the new signal has been collected at different environmental conditions than the structure has experience before or if damage has occurred. Therefore when the baseline set grows, the results need to be assessed to determine which of these is the case.

7.2 Experimental description

The GWSHM system is attached to a steel water tank which is situated outside of the Fluids Laboratory at the University of Bristol in a relatively sheltered location. A picture of the water tank is shown in figure 7.2. It is constructed of 5 mm steel sheet and is made up of multiple panels which are bolted together. There is a layer of sealant between each panel at the bolted joint. Attached to the tank is an array of 8 PZT disk transducers which are 1 mm thick and 20 mm in diameter. These are all positioned in one panel. They are bonded to the structure using cyanoacrylate adhesive and they are covered with silicon sealant to provide some environmental protection. The positions of the transducers

Transducer	X Position (m)	Y Position (m)
1	0.160	0.141
2	0.282	0.431
3	0.601	0.142
4	0.775	0.455
5	1.022	0.120
6	1.208	0.429
7	1.560	0.160
8	1.722	0.430

Table 7.1: The transducer positions on the water tank measured from the bottom left corner.

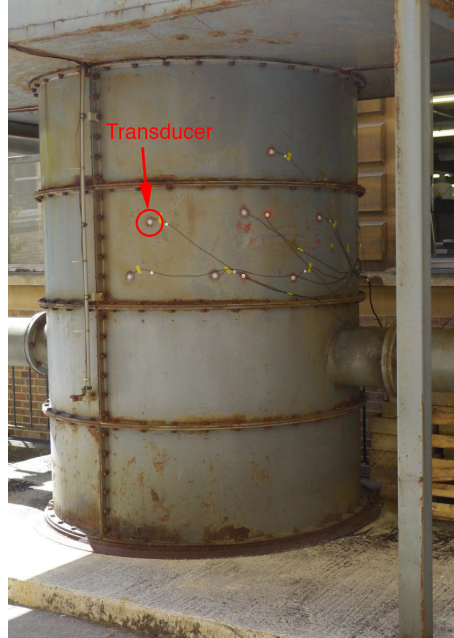


Figure 7.2: A picture of the water tank.

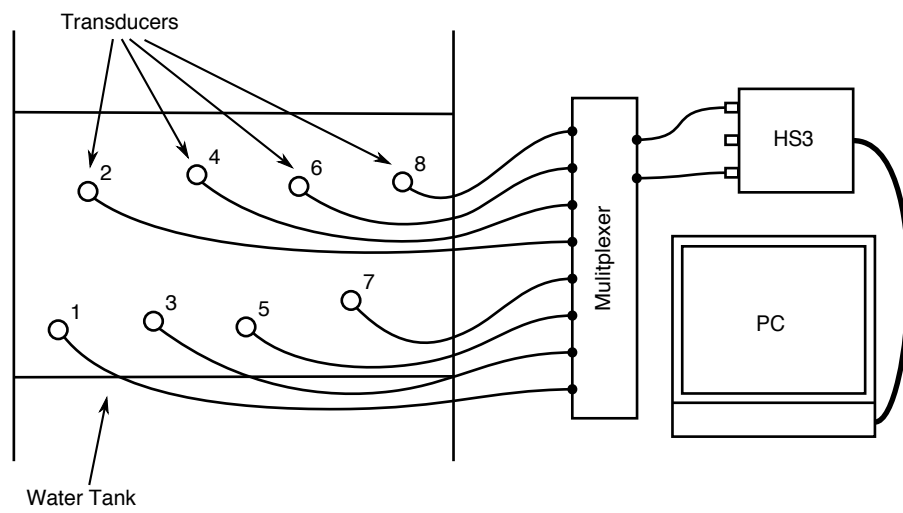


Figure 7.3: A diagram of the experimental setup.

are listed in table 7.1 and they predominately excite the S_0 mode. The data collection equipment consists of a TiePie Engineering Handyscope HS3 which is used as both a function generator and oscilloscope. This is connected to a computer where the data is stored. The output and 1 input of the HS3 is connected to a multiplexer which has been built in house at the University of Bristol. This enables either input or output to be connected to any of the transducers. This setup is shown in figure 7.3.

When a collection occurs each possible combination of transmit and receive transducer is switched to in turn. One transducer is excited and the other receives. The excitation is a chirp signal [77] which is equivalent to a 250 kHz 5 cycle Hanning windowed tone burst averaged 300 times. Using a chirp excitation allows whole collection to occur quickly over a period of a couple of minutes. Collections are initiated every 20 min and the experiment has been running since January 2012. There have been a few gaps where no data was collected due to computer unreliability and building work but the data acquisition equipment and all experimental parameters have remained the same.

7.3 Changes in signal parameters

How the signals change over time will now be studied by finding the first arrival time, maximum amplitude, centre frequency and bandwidth for each signal. It is important to understand these changes because they affect how the whole GWSHM systems perform. The first arrival time is defined as the time when the signal amplitude exceeds a threshold. The maximum amplitude is the maximum amplitude of the whole signal, which in all of the transducer pairs happens to be the first S_0 arrival. The centre frequency and the -20 dB bandwidth are found from the frequency spectrum of the whole signal. This will be done for all collections in the dataset from 4th January 2012 until 17th February 2015 for all unique transducer pairs. This means that there are 54 398 collections and 28 signals per collection. Due to the amount of data points generated in this analysis, the mean and standard deviation of all the signals for each collection will be shown. Additionally a subset of the dataset, a week from 13th to 18th February 2012, will be plotted to show the changes over a daily period.

Figure 7.4 shows how the mean first arrival time for the signals changes. The value used is the arrival time difference which is the arrival time for each collection minus the mean arrival time for that transducer pair. This value is calculated before the mean and standard deviation of all unique transmit and receive pairs is found. Over both time scales it can be seen that the mean value and the standard deviation stays approximately constant. There are occasional large deviations in the mean value up to about 2×10^{-5} s but the mean value

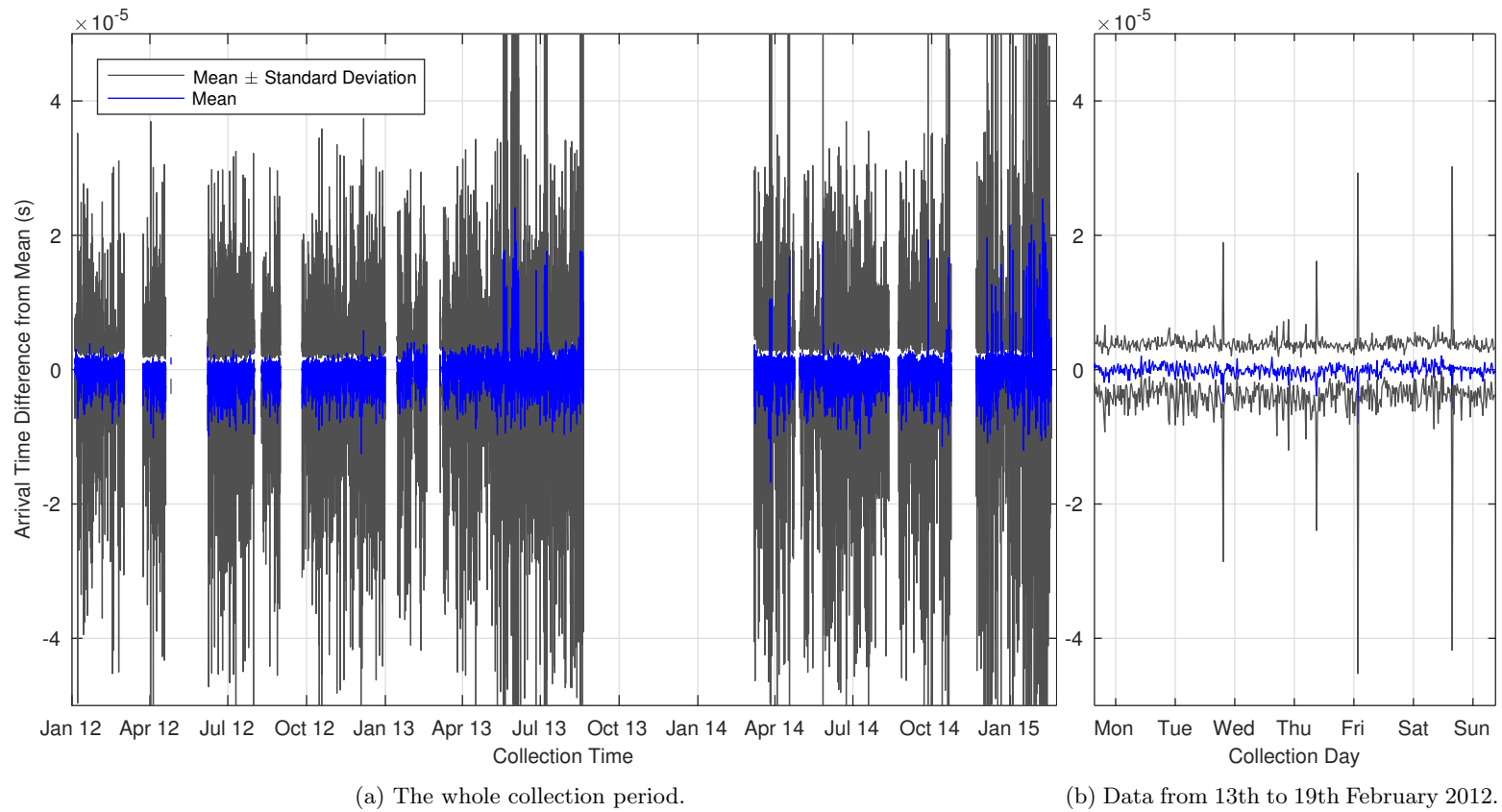


Figure 7.4: The mean and standard deviation of the first arrival time difference for all transducer pairs.

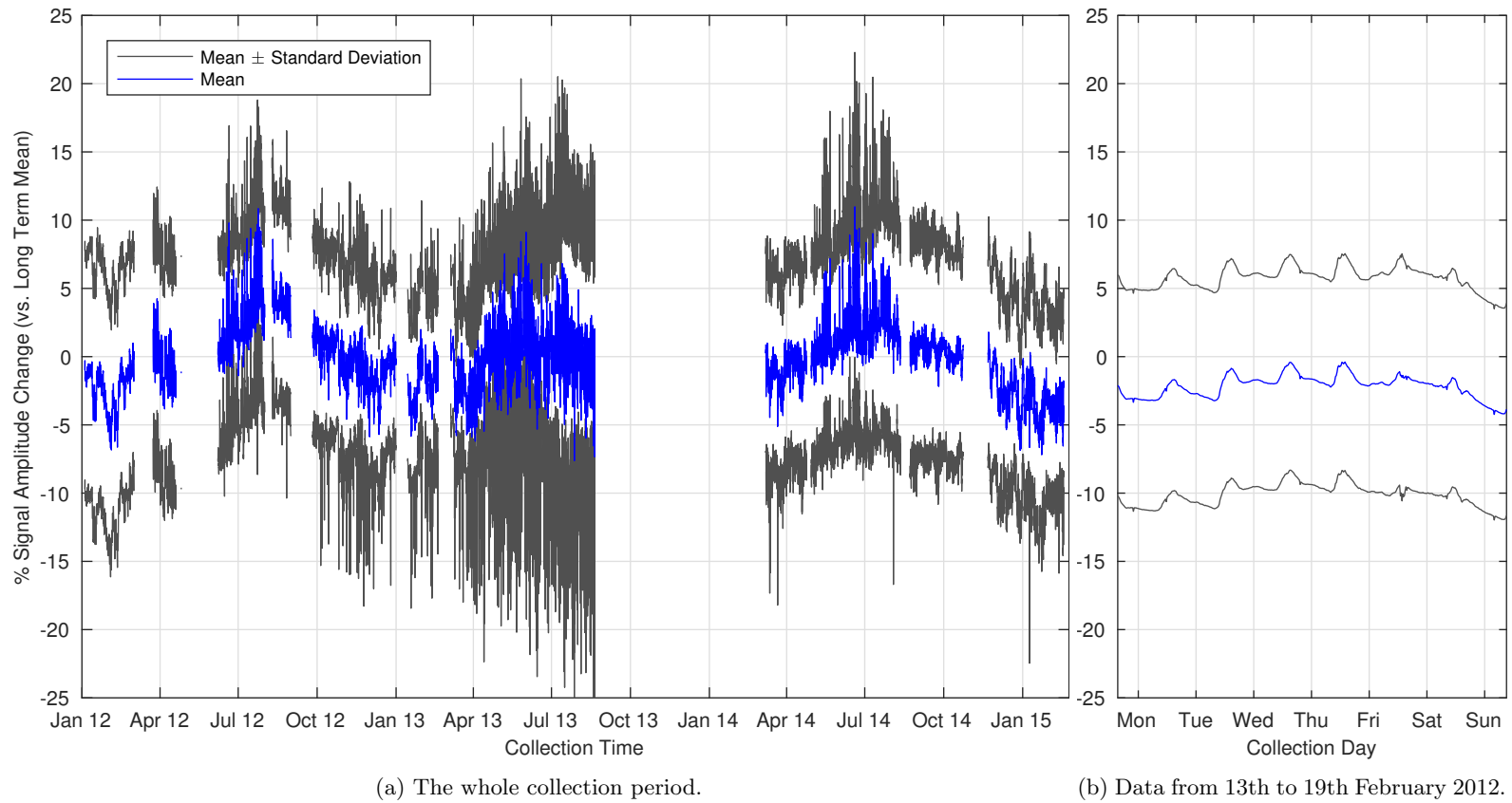
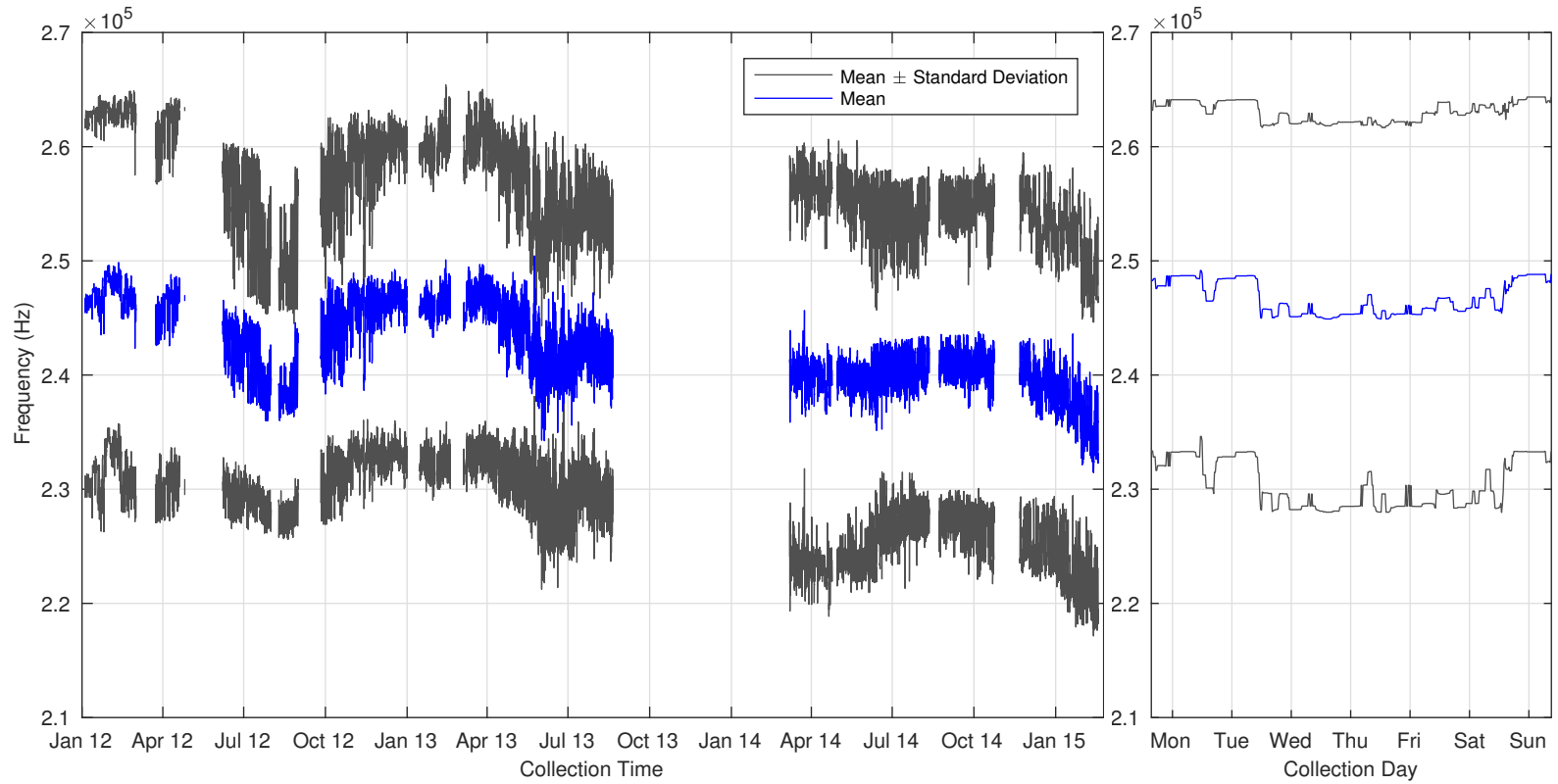


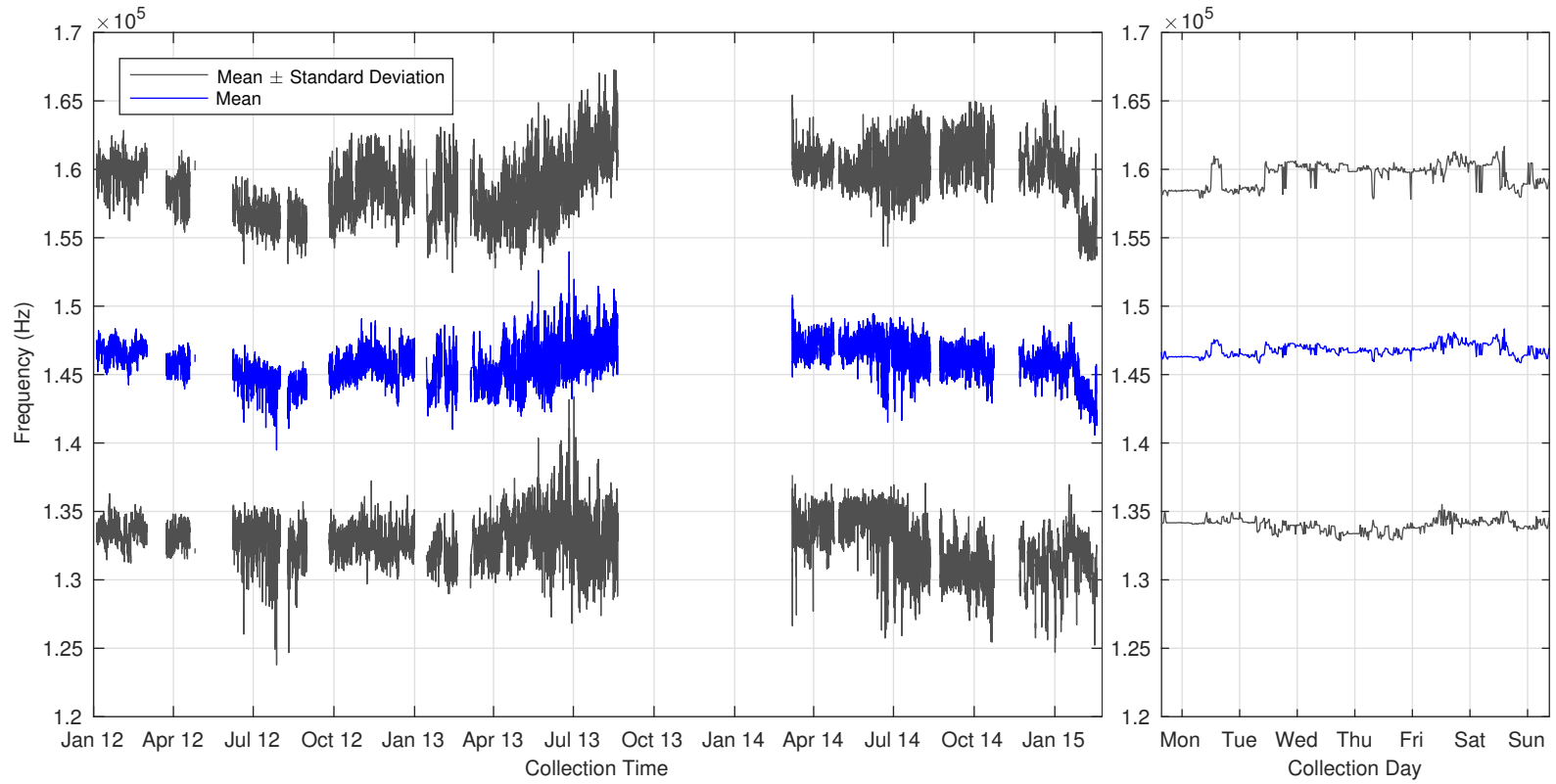
Figure 7.5: The change in mean and standard deviation of the maximum amplitude for all transducer pairs.



(a) The whole collection period.

(b) Data from 13th to 19th February 2012.

Figure 7.6: The mean and standard deviation of the centre frequency for all transducer pairs.



(a) The whole collection period.

(b) Data from 13th to 19th February 2012.

Figure 7.7: The mean and standard deviation of the bandwidth for all transducer pairs.

remains centred at zero for the whole experimental period. This can be seen in figure 7.4b where the deviations in the mean value are significantly smaller than the time period of the excitation which is 4×10^{-6} s and this is the case the majority of the time. This means that across the whole collection period the group velocity has remained constant. That it has remained approximately constant over a daily time period suggests that, at this operating frequency-thickness range, the effect of temperature on group velocity is negligible. For an active GWSHM system this would suggest that the OSM will not be effective on this dataset as the change it attempts to compensate for is not present. For an AE system this would suggest the first arrival times and therefore the ΔT values will not be significantly affected. The ΔT values are the key value for location performance in AE systems so this result suggests that would be consistent over long term data collections.

Unlike the first arrival time, the maximum amplitude of the signal changes on both daily and seasonal time periods. It can be seen in figure 7.5b how the maximum amplitude changes over a day. The amplitude peaks in the afternoon and troughs in the night. This corresponds to how the ambient temperature changes over a day. When it is warmer, the stiffness of the steel and bonding adhesive decreases which means a greater amplitude is excited. A similar effect occurs over a yearly time period and this can be seen in figure 7.5a. The maximum amplitude of the signals occurs around July and it is minimum in February. An effect not present in these results is long term changes. Although it varies with temperature, the maximum amplitude appears to be at a similar value for the same point over different years. This parameter therefore seems not to have aged and the amplitude response of system has remained constant.

Figures 7.6 and 7.7 show the frequency response of the system. It can be seen in figures 7.6b and 7.7b that the centre frequency and bandwidth of the whole signals appears to remain approximately constant over a short time period. Neither parameter shows the kind of consistent response to daily temperature that the maximum amplitude does. However seasonal variations do appear to occur. The centre frequency generally appears to behave in an inverse way to temperature with troughs in July and peaks in February. This shift has a range of approximately 16 kHz. The bandwidth of the signals also shifts with temperature but in this case proportional to temperature. This shift is smaller with a range of approximately 10 kHz. After March 2014 both the bandwidth and centre frequency seem to be less affected by the seasonal shifts. This break was after a period of building work where the data collection equipment had to be moved. It is unclear whether this change is due to the change in position of the equipment or another change. The range of measurements for this period is still within the range of measurements prior to the building work. It is unclear

as to why the frequency response of the system changes on a seasonal time scale but not with daily temperature changes.

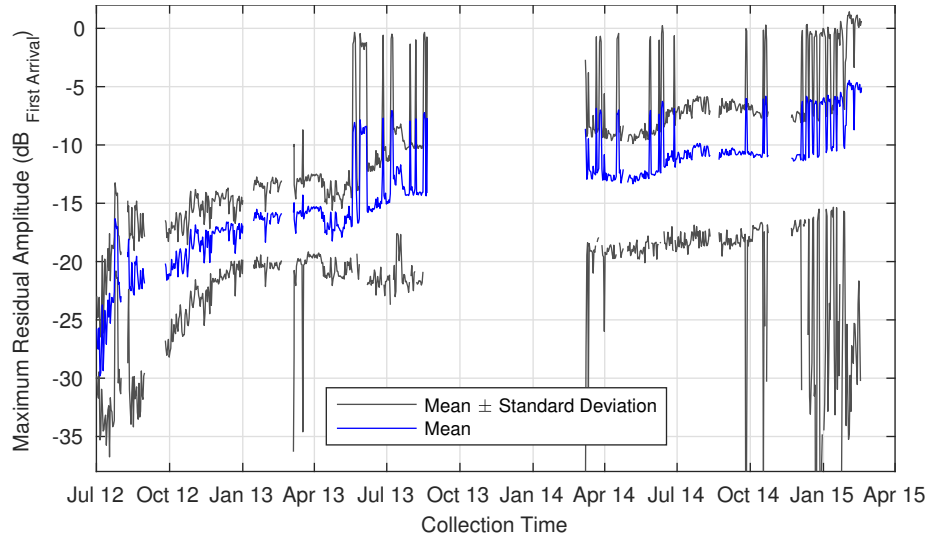
In general, none of the signal parameters measured suggest ageing has occurred. Temperature variations have an effect on the maximum amplitude of the signals, the centre frequency and the bandwidth of the signals. For active GWSHM systems methods to compensate for temperature changes exist so, providing they work correctly, these results suggest that the system should perform well over long time scales because none of the parameters are notably changing. For AE systems the results are also promising. The key parameters for most AE systems are the ΔT times, determined by the arrival times, and the amplitude of the first arrival. The effect of temperature on amplitude may affect the detectability of signals with a low SNR, but because none of the parameters show any sign of long term ageing, it is likely that an AE system would perform consistently in the long term.

7.4 Performance of baseline subtraction techniques

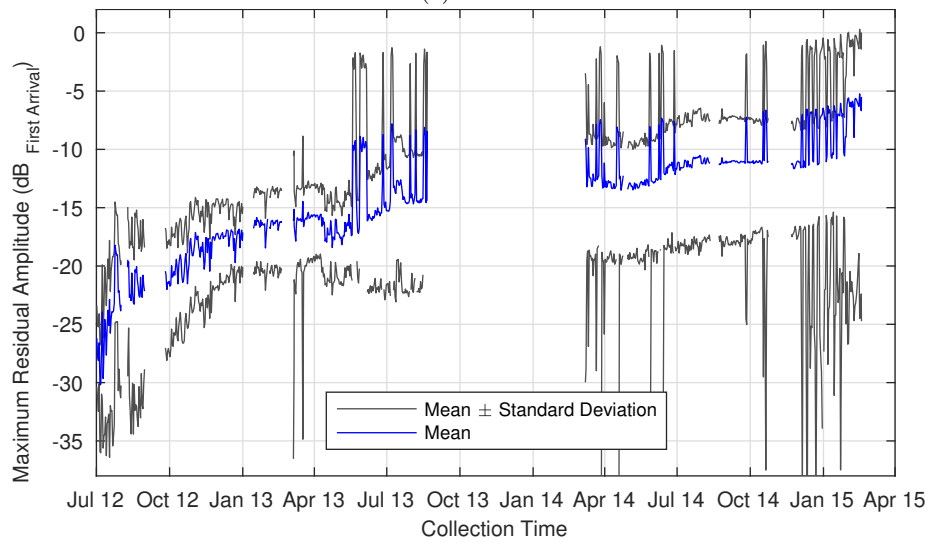
Typical active GWSHM data processing approaches will now be applied to the dataset to test how well an active system would perform over a long period of time. This is to validate the conclusions of the previous section that because none of the individual signal parameters are ageing, an active GWSHM system should perform well over long time periods. This section is of less relevance to an AE system. A subset of the dataset has been used here to keep the data processing time to a manageable level. The closest baseline to midday was used over the entire collection period.

Prior to applying any baseline subtraction algorithm some signal conditioning was applied to both the baseline and data signals. These include:

1. A Tukey window time filter to remove the crosstalk at the beginning of the signal and to zero the end of the signal. This removes unnecessary noise when the signal is Fourier transformed.
2. A frequency filter with a bandwidth of 200 kHz centred on the excitation frequency.
3. Normalizing the signals by their first arrival. This is to compensate for changes in amplitude caused by temperature.
4. Finding the best matching overlap between the data and baseline signal to correct for jitter in the Analogue to Digital Converter (ADC).

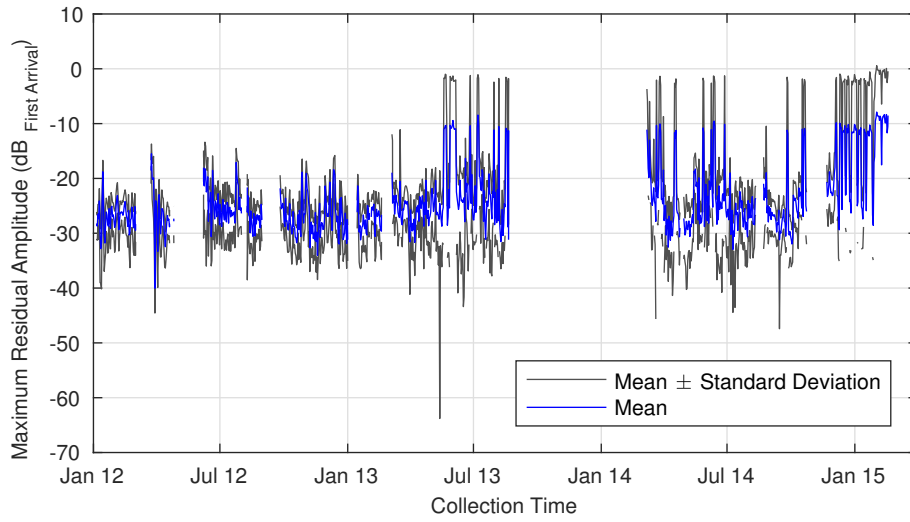


(a) OBS.

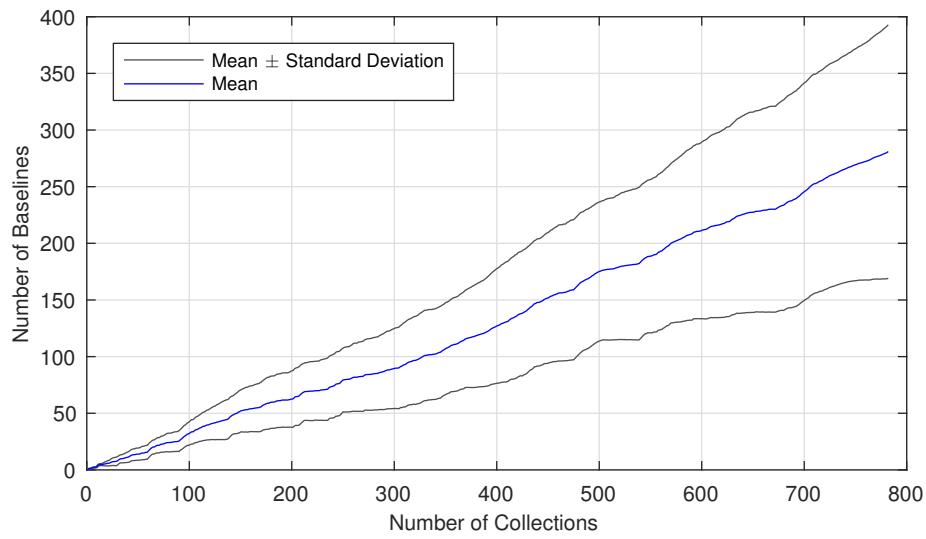


(b) The OSM then OBS.

Figure 7.8: The mean and standard deviation maximum amplitude across all transducer pairs for different processing methods with a defined baseline set.



(a) Maximum residual amplitude.



(b) Baseline set size.

Figure 7.9: How the mean and standard deviation of different parameters change when the CBG algorithm is applied to a subset of the dataset.

7.4.1 Defined baseline set

The first 2 data processing approaches applied were with a defined baseline set. The first 6 months of collections were used as the baseline set because in this time period the water tank should have experienced the majority of United Kingdom ambient conditions. This gives a baseline set of 115 collections and a dataset with 667 collections. It should be noted that there are gaps in the baseline set from the 1st to the 23rd March and the 19th April to the 7th June. Despite this it is likely that signals collected at the complete temperature range are contained within the dataset.

The first data processing approach was to apply OBS on its own with the defined baseline set. For each data signal the maximum value of the residual signal was found post subtraction. To display the results, the mean and standard deviation of the maximum residual values were found across the unique transducer combinations. Because the signals have been normalised, the mean and standard deviation can be calculated across all of the transducer combinations, despite their different path lengths and therefore amplitudes. These values are shown in figure 7.8a. It can be seen that with this approach the mean maximum residual value starts at around -27 dB but this quickly increases. It is smaller than -25 dB for 7 days of collected data and smaller than -20 dB for 23 days. The last time the mean maximum residual is below -20 dB is after 142 days.

The next processing approach was to apply the OSM prior to OBS. This is the most computationally expensive permutation using these two processing methods and they are traditionally applied in the opposite order. It will however give the best possible residual value from this dataset and these two methods. The mean and standard deviation of the maximum residual value for the OSM then OBS is shown in figure 7.8b. The residual performance is very similar to when only OBS was applied. The days at which the residual value is greater than -25 dB and -20 dB are identical. The mean and maximum difference in maximum residual between the two approaches are -0.39 dB and -2.04 dB respectively. That the OSM does not reduce the value of the residual greatly is explained by the results in section 7.3. The first arrival time and therefore the group velocity of the wave has remained approximately constant and therefore the effect the OSM is attempting to compensate for is not present.

Given the results in section 7.3 where the parameters measured show no long term changes, it is surprising how quickly the subtraction performance of the system degrades for both approaches. The maximum value of the residual determines the necessary amplitude of reflection a defect must generate to be detected. Therefore after only a short period of time this system will only be able to detect gross defects and would be of limited use.

7.4.2 Continuous baseline growth algorithm

The CBG algorithm will now be applied to the same subset of the dataset but without the split into baselines and data. This gives a dataset of 782 collections. This approach will show whether the signals continuously change or eventually stabilise to something similar. The CBG threshold, whereupon the signal is added to the baseline set, was set to be -25 dB.

The mean and standard deviation of the maximum residual values of each collection are shown in figure 7.9a. It can be seen that the mean residual value stays around the CBG threshold value for most of the collections. However it does not consistently stay below this value. This shows that the many of the new signals are unlike the baseline signals so are subtracting poorly. This is confirmed by continuous growth of the baseline set which is shown in figure 7.9b.

That the baseline set never ceases to grow means the signals are constantly changing. They are never similar to signals collected earlier in the dataset otherwise they would subtract well and not be added to the baseline set. This means, for this system, it would be impossible to use any time period as a defined baseline set. This would prevent the successful implementation of OBS.

7.4.3 Discussion on baseline subtraction performance

The results of this section are contrary to what was suggested in section 7.3. The baseline subtraction performance degrades over a period of about a week in all cases which means the signals are changing in a way not revealed when just looking at simple signal parameters.

Considering the number of variables present in this experiment, it is difficult to identify the cause or causes of the degradation in system performance. Changes in the adhesive bondline, as suggested by [83], seem likely as this is a component vulnerable to ageing. The water tank is likely to have corroded slightly over the years it has been monitored. However it is thought that this will have occurred over longer time scales than that with which the signals are degrading. With this setup on this structure it is clear that monitoring for damage would not be feasible.

7.5 Conclusions

This chapter has highlighted some of the challenges in operating GWSHM systems over long periods of time. The results presented here are from one long term active GWSHM experiment so care must be taken in extrapolating the results to other systems which will likely have different components and setups.

However the water tank monitored here was subjected to relatively benign environmental conditions. An aircraft for example would be subjected to a much larger temperature range and significantly more brutal external conditions. It is likely that this would be the case in many other GWSHM applications as well. It would be possible to improve upon the experimental setup on the water tank in terms of robustness and environmental protection. Despite these factors, it is likely that behaviours similar to those discovered here would occur in other GWSHM systems operated over a long period. This is because the system collected good quality signals over the whole time range of operation and the changes that cause problems were very subtle, so it would appear the system was robust enough for this application.

When investigating how individual parameters changed over the monitored period maximum signal amplitude, centre frequency and bandwidth all showed some changes in sequence with ambient temperature. First arrival time did not although this may not hold true for other materials or plate thicknesses. None of the parameters showed significant signs of long term changes and therefore system ageing. This is a promising result for AE systems similar to the BALRUE system because these types of system operate using these parameters. It is therefore likely that they will operate consistently over long periods of time, although some consideration of temperature changes in data processing and interpreting results might be worthwhile.

Baseline subtraction based processing methods were applied to a subset of the dataset to test how an active GWSHM system would perform over this time period. Given that individual parameters were not ageing it seemed that the system would perform well but this was not the case. When using OBS or OBS combined with the OSM and a defined baseline set, the maximum amplitude of the residual increased after a short period of time. This means the system would be unable to detect defect reflections after a period of weeks, rendering the system useless. When the CBG algorithm was applied, the baseline set continued to grow across the whole time range. This means at no point in time did the signals return to a state where they were similar to the signals before them. This means that the signals are changing in a way not highlighted by the measured individual parameters.

The cause of these small changes are unknown. Potential candidates for ageing are the transducer bondline, the frequency response of the transducers or the structure itself. It may well be possible to reduce these changes through different GWSHM system design but it is likely that some form of ageing in the structure and the components in the system is inevitable. Whether this can be reduced to a level where baseline subtraction based techniques will work is unknown. Recently other active GWSHM processing techniques have been

developed that look at how components of the signal change. These include Singular Value Decomposition (SVD) [88] and Independent Component Analysis (ICA) [89]. How these techniques would perform with signals from an ageing system is unknown but given the experimental results in [88] are collected over 7 months, this may prove a promising direction for further research. If not another must be found for the successful implementation of active GWSHM to occur.

Chapter 8

Conclusions

The conclusions in this thesis will be split into several different parts. First how the main focus of this thesis has been addressed will be discussed. This is gaining an understanding of how the structure that is being monitored effects the performance of the AE system. This has been achieved through modelling the guided wave propagation. Next the other achievements in this thesis will be discussed. This includes the development of a DoE based data collection approach that aims to reduce the experimental effort in validating guided wave models. It also includes analysis of the results from a long term GWSHM experiment. After this the implications of this work on Airbus AE testing will be explained. Finally, possible further work is suggested for topics outside of those directly relevant to Airbus AE testing.

8.1 Understanding the effect of the structure on acoustic emission system performance

The main aim of this work was to improve understanding of how the structure being monitored will affect the performance of the overall AE system. This need was identified from an analysis of a test performed on a section of the wing of an A380 during a whole aircraft fatigue test. Three main areas that needed improvement were identified in this test; the performance of location algorithms, increasing understanding of the attenuation of AE event signals in the structure and better understanding of the sources of AE events. The area it was chosen to focus upon was to increase understanding of the wave propagation in the structure. With this it may be possible to avoid some of the causes of the poor performance of the AE system in the A380 test if such a test were to be repeated.

To gain a greater understanding of the wave propagation in the structure it was modelled. This modelling used the framework developed by Scholey in [44]. In this framework each component in the system is modelled in the frequency domain using the LTI systems approach. This includes both direct components in an AE system and the wave propagation in the structure. The majority of the effort in this thesis has been focused upon modelling the wave propagation in the structure and defining a suitable AE source.

In this work, the AE source would be a fatigue crack in aluminium. These are a common problem in ageing aluminium aircraft and usually initiate from a geometrical feature such as a hole or thickness change. Previous work by other authors had identified problems characterising AE sources from narrow test samples [62, 50, 44]. These include not being able to identify a clear first arrival due to reflections from the sides of the specimen and not being able to measure the angular properties of the source due to the narrowness of the specimen. Due to these problems, only one suitable paper was found for fatigue cracks in aluminium plate which had been characterised on a wide specimen. From this paper, the absolute displacement of the source on the surface was estimated to give a suitable input to the model. This was compared with the AE signal produced by a PLB. The maximum amplitude of the AE signal from the fatigue crack was estimated to be 3.94 and 1.92 times greater than that measured from a PLB for the A_0 and S_0 modes respectively.

The next step was to compare the source obtained from the literature to results collected from a fatigue test performed on a section of the wing of a A340-600. NDT inspections conducted at points during and at the end of this test reported many damage types including fatigue cracks. The analysis reports on the results of this test, which was conducted in 2003, were positive about the performance of the AE system. There was a good match between the AE results and NDT reports. During this test, calibration PLBs were conducted at damage locations. The data from this test was reprocessed to find the AE to PLB maximum amplitude ratio for these locations. The mean AE to PLB ratio for this test was found to be 10.94. This is significantly greater than the values for either mode obtained from the literature.

Given PLBs are often used to aid the setup of AE systems by simulating an AE event, this is potentially quite a promising result. This is because it suggests the majority of AE events produce amplitudes greater than a PLB. This means if the AE system can detect PLBs at the locations of interest it is likely to also be able to detect AE events from these locations. However the disparity between the AE to PLB amplitude ratios found from the test and the literature raises the concern that the AE events being detected in the test are not from fatigue cracks. They instead may be from other unknown AE sources.

This concept is reinforced by the high percentage of AE events in this dataset that were not located near known damage locations. Whether these concerns are true or false is not possible to determine given the time that has passed since this test. Understanding this should be a priority for Airbus in the future. The results from the A340-600 test do however suggest the AE source identified from the literature is suitable for use in the modelling because it is of conservative amplitude compared to the AE events reported in the test.

It is aimed for AE to provide SHM over large areas of an aircraft. Therefore the modelling methods used in this work must be feasible to apply to over large areas which contain many structural features. Most examples in the literature model significantly smaller areas. For example it would not be practical to create a FE model for large sections of aircraft at the resolution required to model guided wave propagation. In the modelling framework, each geometric feature is accounted for by transmission coefficients. To obtain accurate transmission coefficients structural features must be modelled or experimentally characterised. There are many examples of methods to model features reported in the literature and many of these are experimentally validated.

In this thesis empirical transmission models have been developed from experimental results. The empirical transmission models have been deliberately designed with conservative simplifications. The key parameter for AE system performance is that it can detect AE events and this is mainly determined by the maximum amplitude of the received signals. Therefore it is preferable for a model to predict a lower maximum amplitude than is really the case because this still guarantees detection of the AE event. The opposite case where the model predicts a higher amplitude than will really occur potentially creates false confidence in the detection performance of the system. This led to the development of 3 approaches to create empirical transmission models. Each approach had a different balance between accuracy and conservative amplitude prediction. The approaches included a single value based on the lower 95 % quantile, a conservative line of best fit which considered the angle of incidence and a model that considered both the angle of incidence and the frequency. These model types are listed in order of increasing accuracy and decreasing conservativeness. Empirical transmission models were created using the different approaches for a bonded box section stiffener, a row of holes and a bolted L-section stiffener.

This approach to generating transmission models was chosen because it reduced the effort when compared to implementing the transmission models found in the literature. This assumes experimental validation of other modelling approaches would have to be conducted when using them. Reducing the effort and resources required to model the wave propagation in the structure increases the chance of modelling being used in industry. Another aim of the conservat-

ive choice of transmission model was to enable multiple similar features to be grouped under one transmission model. This is especially important given the variety of often similar features present in aircraft structures. It would require significant effort to model each individually.

The empirical models of the stiffener features were first tested against experimental results collected on aluminium plates to which were attached identical features to those used to generate the empirical models. The parameter compared between the model and experimental results was the maximum amplitude of the first arrival. This was the first S_0 arrival. On these structures the models performed as expected. The more conservative transmission models gave more conservative predications of amplitude and the more accurate transmission models were more accurate. The empirical modelling approach which satisfied the requirements for conservative amplitude prediction with the highest accuracy was the conservative fit approach. The bolted L-section transmission model was then tested against results collected from a section of A320 wing skin. This contained 4 features that were similar in shape to the bolted L-section but not identical to it. When comparing the maximum amplitude between the modelled signals and the experimental results, the models predicted significantly smaller amplitude values. However the more conservative transmission models still satisfied the conservative amplitude requirements. Therefore this demonstrates how features can be grouped together with conservative transmission models. This is while still producing amplitude predictions that will ensure detection despite their limited accuracy. However to do this with more confidence requires significantly more examples.

With an AE source and transmission models defined, some examples of how the overall system model can be used were demonstrated. This included showing which transducers could detect AE events at different positions for structures containing different features. The effect of transducer positioning and location algorithm choice on AE event location error was demonstrated. This showed in which situations the location algorithms performed poorly and how to mitigate this poor performance. An example was also shown using the A_0 mode as the primary mode of operation and showed the additional considerations required when using this mode.

In each of the modelling examples, the AE source was simulated at many thousands of different locations. That this was possible to implement shows the advantage of using a modelling approach with low computational requirements. This makes this technique possible to use during future development of AE systems. The conservative simplifications inherent in the transmission models need to be understood because they limit the accuracy of the modelled signals. However results from this kind of modelling could, for example, be used

in assessing a new location algorithm. If an AE system was needed to monitor a new structural test, then this modelling approach, possibly with additional transmission models for other geometrical features, could be used to determine the transducer positioning to guarantee detection. Therefore, despite the limitations in accuracy, the modelling approach is still useful and can be applied with levels of resources suitable for the development of AE systems. If greater accuracy were required, for example in qualifying the technique, then it is likely that significantly more resources and expenditure would be required.

8.2 Other key achievements

8.2.1 A design of experiments data collection approach

To validate the transmission models, experiments were conducted using an EMAT to simulate an AE source. This involved moving the EMAT between many different locations. It quickly became apparent that this would be very time consuming if measurements were taken over a large 2D area with a high-resolution grid of locations. This was not done to validate the transmission models in this thesis but hypothetically could be necessary to validate modelling on very complex structures or in qualifying AE systems.

To make this possible, a concept for a data collection approach was developed. This was based upon the HilomotDoE algorithm which is an algorithm based upon DoE principles with an active learning step. The aim of applying this technique was to reduce the number of points to be collected compared to a raster scan, thereby reducing the total experiment time. This was to be done without decreasing the amount of information obtained about the guided wave propagation within the structure.

Guided wave propagation is very predictable in plates with no features. If beam spread is compensated for, the maximum amplitude of the wave will remain approximately constant for materials with low attenuation. At geometrical features the wave is scattered and therefore the amplitude will change. Therefore it is not necessary to take guided wave measurements at high spacial resolution in the centre of plates to obtain sufficient information about the wave propagation in this region. Near features the opposite is true and a high spacial resolution of measurements is desirable to better understand the wave propagation as it passes over the feature.

The data collection approach developed in this thesis uses iterative steps to determine which of the measurement points should be collected next to give the most information about the structure. This is done by finding points which do not fit local plane models of the measured parameter well. If the parameter is

the maximum first arrival amplitude, then this would be the case in areas where the wave propagates across a feature and decreases suddenly in amplitude. As more data points are collected the local models are refined. This is repeated until a stop criterion is reached. If the stop criterion is set correctly, then the difference between a full raster scan of the area and an interpolation of the points collected by the algorithm should be very small.

The algorithm was tested on simulated data and here it performed well. The same was shown for early experimental results. The reduction in the number of collection points was proportional to the complexity of the structure. Further validation of the approach is required but results so far are promising. The DoE data collection approach has the potential to reduce the time required to validate modelling of the wave propagation for AE systems or AE systems themselves. It could also potentially be applied to other NDT applications where part of the response is predictable and adaptable resolution in data measurement points is appropriate.

8.2.2 Long term system performance

There have not been many examples reported in the literature of GWSHM systems successfully operating over long periods of time. If GWSHM is to be applied to in service aircraft then the systems need to operate very reliably over periods of 25 years or more. This is likely to also be the case for other industrial applications of GWSHM.

In this thesis the results from an active GWSHM system that has been operated for nearly 3 years have been shown. This is a short period of time in comparison to the target application but is significantly longer than most laboratory experiments. The system performance has been analysed and conclusions have been drawn for both AE and active GWSHM systems.

The structure monitored was an outdoor steel water tank. Signals were collected for the wave propagation between pairs of transducers and from these signals individual parameters were found and analysed. It was found that maximum signal amplitude, centre frequency and bandwidth all showed some changes with ambient temperature. Ambient temperature varies on both daily and annual cycles. The first arrival time remained constant across the data collection period. For all parameters, no longer term trends over multiple years were apparent. This suggested that as long as the temperature effects were accounted for, GWSHM systems should perform well over long periods of time.

To test this for active GWSHM systems baseline subtraction techniques were applied to a subset of the dataset. These techniques were OBS and the OSM. For any combination of the techniques the amplitude of the residual quickly

increased over a period of weeks to a level where only gross damage would be detected. This suggested other more subtle changes were occurring to the received signals that were not apparent in the individual signal parameters. The CBG algorithm was also applied to the subset of the dataset. This showed that at no point during the collection period did the received signals return to a state similar to that which they were before.

Most AE systems operate using simple signal parameters such as the first arrival time and the maximum amplitude of the first arrival. The results shown in this section therefore indicate, as long as temperature effects are considered, AE systems should be able to perform well over long time periods. The results here are not however promising for active GWSHM systems using baseline subtraction techniques. These are only the results for one experiment and therefore may not hold true for different equipment. Despite this some ageing effects are probably inevitable in GWSHM equipment and the structure itself. Whether these can be reduced to the point where baseline subtraction techniques can be applied is an open question. If not other signal processing techniques are required for the successful operation of active GWSHM.

8.3 Recommendations for Airbus

This section contains a list of practical recommendations to improve AE testing at Airbus. For most of these recommendations it is hoped that these will be possible to implement without significant investment of resources. Where this is not believed to be the case it will be stated.

- The discrepancy in AE to PLB amplitude ratios found between the literature and the results found from the A340-600 test raises questions about what is the AE source predominately detected in the structural test. Are the AE signals detected from fatigue crack damage or other unknown AE sources? This doubt is compounded by the proportion of AE events which are not matched to damage locations confirmed by NDT. It should be noted here that this may be due to the limitations of applying a 2D location algorithm to a 3D structure.

To further investigate this it is recommended that PLBs are performed close to damage locations after as many structural tests as possible. A matching procedure, as demonstrated in chapter 2, should then be performed so that the AE to PLB ratio can be found for each damage location and damage type. A database of the results should then be created so that the relative amplitudes of different types of damage in different materials and thicknesses can be recorded and understood. This could be used

to aid the design of future tests because the amplitude of the likely AE sources would be better understood. This is also likely to be the only method to characterise the whole range of situations fatigue cracks can occur. Fatigue crack tend to initiate from geometrical features which will influence the wave propagation from the source. It would not be feasible to perform laboratory tests to measure the emitted AE for every scenario, geometrical feature and location that could generate a crack in an aircraft. There would be a further benefit in performing this work. The results both from the literature and the A340-600 test suggest PLBs generate smaller amplitudes than AE events in real structures. If this can be confirmed then this would give great confidence in using PLBs in the calibration of and to test AE setups. This is because they would be confirmed as a conservative in amplitude AE source.

- The benefits of using the modelling approach described in this thesis to better understand AE system performance have been discussed earlier in the conclusions. However to implement this further would require significant investment of resources. The first step would be to increase the library of transmission models for different features. This would enable conservative modelling of the wave propagation in more than just a section of wing skin. If this work was conducted it would also be of interest to colleagues working on active GWSHM systems.
- For significant tests such as the A340-600 EF2 test and the A380 EF2 test it would be worth using a deliberately high transducer density. To simulate a more realistic setup, transducers could be excluded from the recorded results in post processing. This would ensure a high rate of detection for the AE events in the structure and aid understanding of what AE events are not recorded by a more realistic and less dense transducer arrangement.
- The A_0 mode is sometimes used as the main operating mode in Airbus AE tests. As was demonstrated in section 5.5, the S_0 mode can trigger transducers when the AE source is close to those transducers. This negatively affects the location performance because the triggering mode is assumed to be A_0 . This should therefore be considered when interpreting AE location data when using the A_0 mode. Better performance may be obtained by raising the threshold to reduce the likelihood of S_0 triggering.
- Section 5.4 shows the benefits of using the numerical Point Method over the analytical Paget algorithm. The Point Method produces smaller values of location error, always gives a solution and information about the extent of the structure can be included in this algorithm. The disadvantage of

Point Method is it has greater computational demands than the Paget algorithm. Therefore it is suggested it is applied in post processing of the data. The Paget algorithm should continue to be used for real time applications.

If the resources could be made available for it, it would be worth implementing the Point Method for 3D structures constructed from plates. This would enable much better location performance when the AE sources were generated on a different plane to which the transducers are attached. This was the case for many AE sources in the A380 test where the BALRUE system performed poorly.

- Both of the location algorithms tested in section 5.4 have combinations of ΔT values which can produce multiple valid solutions for the location of the source. This can be mitigated by using 4 transducers and only locating within the area surrounded by transducers. The last requirement will not always be possible. Where it is not, the existence of multiple valid locations needs to be considered during the interpretation of the location results. It would be worth including both potential locations in location plots with a flag to identify those points where there might be multiple solutions. This would require a redefinition of false call rates. It would be better to say an AE event has been located but it may be located at one of two positions than there is a false call rate of 50 %.
- In section 2.4.2 work was done to estimate the events that were not recorded due to the phenomenological filters in the BALRUE system. These estimates suggested the number of missing events was low. However it would be worth confirming this experimentally. It may be better practice to apply this filter in post processing so that its precise effect is made clearer.

8.4 Future work

There are two points of future work that are applicable outside of Airbus AE testing. The first of these is developing further the DoE based data collection approach which was based on the HilomotDoE algorithm. This was described in chapter 6. Currently within this approach there are several user defined parameters which significantly affect the behaviour of the algorithm. These are the threshold for the stop criterion and the number of points per local model. Ideally neither of these values would need user input or the approach to defining them would be clearer. Currently the stop criterion threshold has been defined

from signal information known by the user and the number of points per local has been defined by trial and error. It would be worth investigating alternative stop criteria that do not require a threshold value. One possibility would be to base the stop criterion on the convergence in value of the maximum difference to the model. The number of points per local model could possibly be defined by a minimum area. The user could determine this area by inspecting the features on the structure and sizing it compared to those. In addition to improving the determination of these values, the algorithm needs to be applied to more structures and scenarios to validate its use further.

The second area for future work is the need for more long term experiments to be conducted with GWSHM systems. The results presented in chapter 7 suggest there will be difficulty in applying active GWSHM systems that use baseline subtraction over long periods of time. These conclusions have been drawn from the results of one long term experiment. To test these conclusions further it will be necessary for many more long term experiments to be performed. Research groups with interest in this area should perform such experiments so that they can test both existing methods and the new methods they are developing in more realistic scenarios. This is necessary work to be conducted if GWSHM systems are to be adopted for industrial and commercial use.

Appendix A

Acoustic Emission Source Calculations from the A340-600 EF2 Test

Event	Mean Amplitude (V)						AE/PLB Ratio				No. Unique Matches	Estimated No. Small Events				No. PLBs	Damage Description	Damage Codes	
	PLB			AE			1st Hit	2nd Hit	3rd Hit	Mean		1st Hit	2nd Hit	3rd Hit	Mean				
	1st Hit	2nd Hit	3rd Hit	1st Hit	2nd Hit	3rd Hit													
A01	-	-	-	-	-	-	-	-	-	-	0	-	-	-	0.00	6	Fretting Damage on front spar		
A02	0.016736	0.004927	0.000269	0.012779	0.009525	0.002797	0.764	1.933	10.399	4.365	67	0.28	8.39	13.67	7.45	7		Fretting	
A04	-	-	-	-	-	-	-	-	-	-	0	-	-	-	0.00	9			
B02	0.000461	0.000546	0.000166	0.013844	0.010202	0.008913	30.045	18.699	53.798	34.181	153	25.09	18.11	7.32	16.84	7			
B03	0.000748	0.000355	0.000308	0.018668	0.012710	0.007836	24.952	35.807	25.435	28.732	1883	178.21	69.17	45.23	97.54	15	Crack	D530	
B05	0.002260	0.001118	0.009698	0.009012	0.008291	0.006185	3.988	7.414	0.638	4.013	2749	1113.97	192.51	107.60	471.36	11		D481	
C01	0.004189	0.002018	0.011827	0.010759	0.008776	0.005342	2.569	4.349	0.452	2.456	4794	864.44	324.20	124.52	437.72	8	Rotating bolt	D481	

Event	Mean Amplitude (V)						AE/PLB Ratio				No. Unique Matches	Estimated No. Small Events				No. PLBs	Damage Description	Damage Codes
	PLB			AE			1st Hit	2nd Hit	3rd Hit	Mean		1st Hit	2nd Hit	3rd Hit	Mean			
	1st Hit	2nd Hit	3rd Hit	1st Hit	2nd Hit	3rd Hit												
C02	0.002525	0.001757	0.001379	0.017156	0.012116	0.006556	6.796	6.898	4.756	6.150	1910	109.04	37.96	55.48	67.50	7	Rotating bolt	D55
C03	0.002608	0.005834	0.001112	0.015128	0.008310	0.007288	5.800	1.424	6.555	4.593	1151	199.58	137.01	76.23	137.61	6	Rotating bolt	D480, D431, D688, D432, D470
C04	0.002863	0.000990	0.008906	0.014493	0.007731	0.006287	5.063	7.810	0.706	4.526	1469	329.26	140.81	90.67	186.91	8	Rotating bolt	D431
C05	0.004677	0.001413	0.011027	0.033365	0.006034	0.008310	7.134	4.272	0.754	4.053	906	8.98	49.71	10.77	23.15	8	Rotating bolt	D688
C06	-	-	-	-	-	-	-	-	-	-	0	-	-	-	0.00	1	Rotating bolt	D432
C07	0.001987	0.000817	0.003114	0.010509	0.006045	0.005126	5.289	7.399	1.646	4.778	529	20.32	149.33	29.04	66.23	2	Rotating bolt	D470
C08	0.003836	0.002284	0.001209	0.012201	0.010254	0.005972	3.181	4.490	4.939	4.203	1966	785.30	103.51	193.48	360.76	11	Rotating bolt	D689
C12	-	-	-	-	-	-	-	-	-	-	0	-	-	-	0.00	9		D226
C13	0.005883	0.002223	0.003486	0.012324	0.009054	0.008130	2.095	4.073	2.332	2.833	163	49.83	11.02	8.32	23.06	5	Rivet damage	D341, D340
C14	0.002050	0.001777	0.001818	0.010352	0.009142	0.008050	5.049	5.145	4.428	4.874	934	301.08	71.15	76.72	149.65	7	Rotating bolt	D690
C15	0.003456	0.000945	0.000402	0.009473	0.007929	0.002000	2.741	8.394	4.976	5.370	31	8.54	8.64	9.75	8.97	8		D714
C19	0.004575	0.002900	0.000440	0.020279	0.007694	0.003600	4.433	2.653	8.186	5.091	374	3.00	0.57	3.35	2.30	4		D143, D144, D716, D717, D718
C20	0.001845	0.005261	0.000829	0.012434	0.006528	0.004222	6.741	1.241	5.095	4.359	145	34.42	35.86	3.05	24.44	7		D141, D142, D415
C21	0.001402	0.000809	0.002210	0.012748	0.008940	0.011682	9.090	11.055	5.286	8.477	291	56.11	8.30	1.83	22.08	6		D490
C22	0.001565	0.002019	0.000536	0.016202	0.011068	0.005172	10.354	5.482	9.641	8.492	163	8.42	3.02	5.10	5.52	7		D145, D491
C23	0.001311	0.001157	0.000903	0.008681	0.006966	0.006896	6.624	6.023	7.637	6.761	726	122.88	52.38	96.14	90.47	9		D283, D363
C24	0.002369	0.002043	0.000699	0.008796	0.009234	0.006368	3.712	4.520	9.104	5.779	170	15.66	5.88	28.02	16.52	7	Crack	D364
C25	0.001224	0.004524	0.000491	0.012538	0.007136	0.004274	10.240	1.578	8.703	6.840	274	71.80	36.58	44.22	50.87	6		D365, D366, D492

Event	Mean Amplitude (V)						AE/PLB Ratio				No. Unique Matches	Estimated No. Small Events				No. PLBs	Damage Description	Damage Codes
	PLB			AE			1st Hit	2nd Hit	3rd Hit	Mean		1st Hit	2nd Hit	3rd Hit	Mean			
	1st Hit	2nd Hit	3rd Hit	1st Hit	2nd Hit	3rd Hit												
C26	0.001448	0.001277	0.000942	0.011031	0.004830	0.007787	7.617	3.783	8.271	6.557	657	74.68	82.17	9.80	55.55	14		D367, D368, D369, D414, D715
C27	0.003464	0.000978	0.000692	0.012851	0.007945	0.006301	3.710	8.126	9.112	6.983	1685	179.65	136.01	106.15	140.60	7	Rotating bolt	D48
C28	-	-	-	-	-	-	-	-	-	-	0	-	-	-	0.00	5		D311
C29	0.001646	0.000509	0.002236	0.010007	0.004736	0.004009	6.081	9.304	1.793	5.726	1568	97.40	433.57	89.74	206.90	8		D434
D01	0.000421	0.000268	0.000364	0.007616	0.003351	0.004263	18.107	12.528	11.712	14.115	9606	2343.44	327.08	21.70	897.41	7	Rivet damage	D230, D265, D338
D02	0.000820	0.000339	0.000556	0.009388	0.004354	0.005282	11.450	12.827	9.503	11.260	8828	1559.14	255.61	21.78	612.18	9	Crack	D527
D03	0.000463	0.000256	0.000513	0.008903	0.004825	0.007968	19.235	18.869	15.540	17.881	4995	1208.75	418.59	28.19	551.84	5		D198
D04	0.000197	0.000333	0.000115	0.025394	0.009057	0.006694	129.099	27.228	58.313	71.547	484	21.00	14.01	14.01	16.34	5		D401, D474
D06B	-	-	-	-	-	-	-	-	-	-	0	-	-	-	0.00	6		D655
D07	-	-	-	-	-	-	-	-	-	-	0	-	-	-	0.00	3		D656
D08A	0.000201	0.000119	0.000129	0.004318	0.002312	0.003362	21.521	19.479	26.138	22.379	69	39.79	14.51	14.15	22.82	4		D549
D10	0.000914	0.000785	0.000251	0.011328	0.006578	0.005631	12.396	8.383	22.448	14.409	307	34.84	57.12	45.39	45.78	5		D488
D11	-	-	-	-	-	-	-	-	-	-	0	-	-	-	0.00	21	Crack	D370, D371, D372, D373, D682, D683
D12	-	-	-	-	-	-	-	-	-	-	0	-	-	-	0.00	14	Crack	D199
D14	0.017100	0.005788	0.000997	0.009849	0.008529	0.004389	0.576	1.473	4.403	2.151	2462	963.26	20.59	281.79	421.88	21	Crack	D446
D15	0.020245	0.014011	0.001241	0.013316	0.009162	0.006185	0.658	0.654	4.984	2.099	2622	158.87	13.53	40.98	71.13	12	Crack	D680
D16	0.005750	0.002203	0.000935	0.013927	0.007515	0.005964	2.422	3.411	6.380	4.071	3329	259.81	74.44	149.05	161.10	16		D902
D17	-	-	-	-	-	-	-	-	-	-	0	-	-	-	0.00	12	Rivet damage	D344
D18A	-	-	-	-	-	-	-	-	-	-	0	-	-	-	0.00	6		
D18B	-	-	-	-	-	-	-	-	-	-	0	-	-	-	0.00	4		
D18C	-	-	-	-	-	-	-	-	-	-	0	-	-	-	0.00	8		
D18D	0.000351	0.000207	0.000204	0.009887	0.003620	0.004393	28.188	17.529	21.518	22.411	67	1.68	5.64	0.29	2.54	1		
D18E	0.000603	0.000394	0.000495	0.011042	0.003206	0.004355	18.325	8.147	8.790	11.754	51	0.70	0.34	0.02	0.35	1		
D19	0.002359	0.000696	0.000541	0.017502	0.010623	0.007470	7.420	15.263	13.818	12.167	9807	1537.08	558.24	236.04	777.12	50	Damaged bolts	D50
D20	0.000941	0.000998	0.000150	0.009012	0.007362	0.005307	9.573	7.380	35.318	17.424	2790	1305.86	150.67	343.14	599.89	26	Damaged bolts	D54

Appendix B

Publications List

The following publications have emanated from the work summarised in this thesis. The chapters relevant to each publication have been listed below each item.

- M. R. Courtier, A. J. Croxford and K. Atherton. “The Long Term Performance of a Guided Wave SHM System on a Steel Tank”. In: *Structural Health Monitoring 2015, Proceedings of the 10th International Workshop on* (2015)
Chapter 7
- M. R. Courtier, A. J. Croxford and K. Atherton. “The long term performance of a guided wave SHM system on a steel tank”. In: *Proceedings of NDT 2015*. 2015
Chapter 7
- M. R. Courtier, A. J. Croxford and K. Atherton. “Guided wave propagation modelling to aid understanding of acoustic emission system performance on complex aerospace structures”. In: *8th European Workshop On Structural Health Monitoring (EWSHM 2016)*. 2016
Chapters 3, 4 and 5
- M. R. Courtier, A. J. Croxford and K. Atherton. “An iterative design of experiments based data collection approach for ultrasonic guided waves”. In: *AIP Conference Proceedings*. Vol. 1806. 1. AIP Publishing. 2017, p. 030012
Chapter 6

Bibliography

- [1] U. G. Goranson. “Fatigue issues in aircraft maintenance and repairs”. In: *International Journal of Fatigue* 19.93 (1997), pp. 3–21.
- [2] J. Schijve. “Fatigue damage in aircraft structures, not wanted, but tolerated?”. In: *International journal of fatigue* 31.6 (2009), pp. 998–1011.
- [3] P. Cawley. “Non-destructive testing—current capabilities and future directions”. In: *Proceedings of the Institution of Mechanical Engineers, Part L: Journal of Materials: Design and Applications* 215.4 (2001), pp. 213–223.
- [4] C. Boller. “Ways and options for aircraft structural health management”. In: *Smart materials and structures* 10.3 (2001), p. 432.
- [5] K. Worden et al. “The fundamental axioms of structural health monitoring”. In: *Proceedings of the Royal Society of London A: Mathematical, Physical and Engineering Sciences*. Vol. 463. 2082. The Royal Society. 2007, pp. 1639–1664.
- [6] H. Speckmann and R. Henrich. “Structural health monitoring (SHM)—overview on technologies under development”. In: *Proc. of the World Conference on NDT, Montreal-Canada*. 2004.
- [7] C. Boller. “Next generation structural health monitoring and its integration into aircraft design”. In: *International Journal of Systems Science* 31.11 (2000), pp. 1333–1349.
- [8] P. Swindell, J. Doyle and D. Roach. “Integration of structural health monitoring solutions onto commercial aircraft via the Federal Aviation Administration structural health monitoring research program”. In: *AIP Conference Proceedings*. Vol. 1806. 1. AIP Publishing. 2017, p. 070001.
- [9] H. Speckmann and R. Henrich. “Structural health monitoring: A contribution to the intelligent aircraft structure”. In: *9th European Conference on Non-Destructive Testing*. 2006.

- [10] J. L. Rose. *Ultrasonic waves in solid media*. Cambridge University Press, 1999.
- [11] H. Lamb. “On waves in an elastic plate”. In: *Proceedings of the Royal Society of London A: Mathematical, Physical and Engineering Sciences*. Vol. 93. 648. The Royal Society. 1917, pp. 114–128.
- [12] A. J. Croxford et al. “Strategies for guided-wave structural health monitoring”. In: *Proceedings of the Royal Society of London A: Mathematical, Physical and Engineering Sciences*. Vol. 463. 2087. The Royal Society. 2007, pp. 2961–2981.
- [13] S. S. Kessler and E. B. Flynn. “Hybrid passive/active impact detection & localization for aerospace structures”. In: *Proc. 9th Int. Workshop on Structural Health Monitoring*. 2013.
- [14] C. K. Lee et al. “Acoustic emission during fatigue crack growth in aluminium plates”. In: *9th European Conference on Nondestructive Testing 2006. Berlin: DGZfP*. 2006.
- [15] C. K. Lee et al. “Acoustic emission from pitting corrosion in stressed stainless steel plate”. In: *Corrosion Engineering, Science and Technology* 43.1 (2008), pp. 54–63.
- [16] P. J. De Groot, P. A. M. Wijnen and R. B. F. Janssen. “Real-time frequency determination of acoustic emission for different fracture mechanisms in carbon/epoxy composites”. In: *Composites Science and Technology* 55.4 (1995), pp. 405–412.
- [17] J. J. Scholey et al. “Quantitative experimental measurements of matrix cracking and delamination using acoustic emission”. In: *Composites Part A: Applied Science and Manufacturing* 41.5 (2010), pp. 612–623.
- [18] P. D. Wilcox. “A rapid signal processing technique to remove the effect of dispersion from guided wave signals”. In: *Ultrasonics, Ferroelectrics and Frequency Control, IEEE Transactions on* 50.4 (2003), pp. 419–427.
- [19] G. Konstantinidis, B. W. Drinkwater and P. D. Wilcox. “The temperature stability of guided wave structural health monitoring systems”. In: *Smart Materials and Structures* 15.4 (2006), p. 967.
- [20] R. L. Weaver and O. I. Lobkis. “Temperature dependence of diffuse field phase”. In: *Ultrasonics* 38.1 (2000), pp. 491–494.
- [21] F. Chen and P. D. Wilcox. “The effect of load on guided wave propagation”. In: *Ultrasonics* 47.1 (2007), pp. 111–122.

- [22] J. E. Michaels, T. E. Michaels and R. S. Martin. “Analysis of global ultrasonic sensor data from a full scale wing panel test”. In: *Review of Progress in QNDE A* 28 (2009), pp. 950–957.
- [23] J. E. Michaels et al. “Impact of applied loads on guided wave structural health monitoring”. In: *AIP Conference Proceedings-American Institute of Physics*. Vol. 1335. 1. 2011, p. 1515.
- [24] T. M. Proctor Jr. “An improved piezoelectric acoustic emission transducer”. In: *The Journal of the Acoustical Society of America* 71.5 (1982), pp. 1163–1168.
- [25] URL: <http://www.physicalacoustics.com/sensors/> (visited on 13/01/2018).
- [26] P. D. Wilcox, M. J. S. Lowe and P. Cawley. “The excitation and detection of lamb waves with planar coil electromagnetic acoustic transducers”. In: *IEEE Transactions on ultrasonics, ferroelectrics, and frequency control* 52.12 (2005), pp. 2370–2383.
- [27] P. D. Wilcox. “Omni-directional guided wave transducer arrays for the rapid inspection of large areas of plate structures”. In: *IEEE transactions on ultrasonics, ferroelectrics, and frequency control* 50.6 (2003), pp. 699–709.
- [28] P. B. Nagy, F. Simonetti and G. Instanes. “Corrosion and erosion monitoring in plates and pipes using constant group velocity Lamb wave inspection”. In: *Ultrasonics* 54.7 (2014), pp. 1832–1841.
- [29] I. Read, P. Foote and S. Murray. “Optical fibre acoustic emission sensor for damage detection in carbon fibre composite structures”. In: *Measurement Science and Technology* 13.1 (2001), N5.
- [30] I. Perez, H.-L. Cui and E. Udd. *Acoustic emission detection using fiber Bragg gratings*. Tech. rep. Naval Air Warfare Center Aircraft Division, 2001.
- [31] G. Wild and S. Hinckley. “Acousto-ultrasonic optical fiber sensors: overview and state-of-the-art”. In: *IEEE Sensors Journal* 8.7 (2008), pp. 1184–1193.
- [32] S. M. Ziola and M. R. Gorman. “Source location in thin plates using cross-correlation”. In: *The Journal of the Acoustical Society of America* 90.5 (1991), pp. 2551–2556.
- [33] J. H. Kurz, C. U. Grosse and H.-W. Reinhardt. “Strategies for reliable automatic onset time picking of acoustic emissions and of ultrasound signals in concrete”. In: *Ultrasonics* 43.7 (2005), pp. 538–546.

- [34] J. Ward, A. J. Croxford and C. A. Paget. “Passive impact localisation for the structural health monitoring of new airframe materials”. In: *Journal of Physics: Conference Series*. Vol. 457. 1. IOP Publishing. 2013, p. 012010.
- [35] A. Tobias. “Acoustic-emission source location in two dimensions by an array of three sensors”. In: *Non-destructive testing* 9.1 (1976), pp. 9–12.
- [36] C. A. Paget, K. Atherton and E. O’Brien. “Triangulation algorithm for damage location in aeronautical composite structures”. In: *Proceedings of the 8th International Workshop on Structural Health Monitoring*. 2003, pp. 363–370.
- [37] J. J. Scholey et al. “A generic technique for acoustic emission source location”. In: *Journal of Acoustic Emission* 27 (2009), pp. 291–298.
- [38] M. G. Baxter et al. “Delta T source location for acoustic emission”. In: *Mechanical systems and signal processing* 21.3 (2007), pp. 1512–1520.
- [39] M. J. Eaton, R. Pullin and K. M. Holford. “Acoustic emission source location in composite materials using Delta T Mapping”. In: *Composites Part A: Applied Science and Manufacturing* 43.6 (2012), pp. 856–863.
- [40] H. Matt and F. L. di Scalea. “Macro-fiber composite piezoelectric rosettes for acoustic source location in complex structures”. In: *The 14th International Symposium on: Smart Structures and Materials & Nondestructive Evaluation and Health Monitoring*. International Society for Optics and Photonics. 2007, 65290Q–65290Q.
- [41] H. K. C. Nucera S. White and F. L. D. Scalea. “Piezoelectric rosettes for acoustic source location in composite structures: Results from blunt impact tests”. In: *Structural Health Monitoring 2013, Proceedings of the 9th International Workshop on*. Vol. 2. 2013.
- [42] F. Ciampa and M. Meo. “A new algorithm for acoustic emission localization and flexural group velocity determination in anisotropic structures”. In: *Composites Part A: Applied Science and Manufacturing* 41.12 (2010), pp. 1777–1786.
- [43] D. G. Aggelis et al. “Acoustic structural health monitoring of composite materials: Damage identification and evaluation in cross ply laminates using acoustic emission and ultrasonics”. In: *Composites Science and Technology* 72.10 (2012), pp. 1127–1133.
- [44] J. J. Scholey. “The development of a quantitative framework for acoustic emission testing”. PhD thesis. University of Bristol, 2008.
- [45] C. A. Paget. *BALRUE system result validation on A340-600 RHS wing portion*. Tech. rep. Airbus UK Ltd, 2005.

- [46] P. Faulkner. *Configuration and Control Software: Vigilant Acoustic Emission Monitoring System*. 1st ed. Ultra Electronics. 2005.
- [47] J. Sodoma. *A380EF BALRUE Data Analysis*. Internal Airbus Presentation. 2007.
- [48] O. Putkis, R. P. Dalton and A. J. Croxford. “The anisotropic propagation of ultrasonic guided waves in composite materials and implications for practical applications”. In: *Ultrasonics* 65 (2016), pp. 390–399.
- [49] M. A. Hamstad, A. O’Gallagher and J. Gary. “Effects of lateral plate dimensions on acoustic emission signals from dipole sources”. In: *Journal of Acoustic Emission* 19 (2001), pp. 258–274.
- [50] M. R. Gorman. “Some connections between AE testing of large structures and small samples”. In: *Nondestructive Testing and Evaluation* 14.1-2 (1998), pp. 89–104.
- [51] D. Gagar and P. Foote. “Generic Methodology for Validating Acoustic Emission Structural Health Monitoring Installations”. In: *Structural Health Monitoring 2015* (2015).
- [52] C. B. Scruby, G. R. Baldwin and K. A. Stacey. “Characterisation of fatigue crack extension by quantitative acoustic emission”. In: *International Journal of Fracture* 28.4 (1985), pp. 201–222.
- [53] D. J. Buttle and C. B. Scruby. “Acoustic emission monitoring of a fatigue crack in 50D steel in a sea-water environment”. In: *NDT international* 22.2 (1989), pp. 81–96.
- [54] A. N. Ceranoglu and Y.-H. Pao. “Propagation of Elastic Pulses and Acoustic Emission in a Plate - Part 1: Theory, Part 2: Epicentral responses and Part 3: General Responses”. In: *Journal of Applied Mechanics* 48.1 (1981), pp. 125–147.
- [55] R. L. Weaver and Y.-H. Pao. “Axisymmetric elastic waves excited by a point source in a plate”. In: *Journal of Applied Mechanics* 49.4 (1982), pp. 821–836.
- [56] C. B. Scruby. “An introduction to acoustic emission”. In: *Journal of Physics E: Scientific Instruments* 20.8 (1987), p. 946.
- [57] C. A. Paget. *Acoustic emission analysis from the A340-600 EF2 RHS wing portion between May 2002 and July 2003*. Tech. rep. Airbus UK Ltd, 2005.

- [58] D. G. Aggelis, E. Z. Kordatos and T. E. Matikas. “Acoustic emission for fatigue damage characterization in metal plates”. In: *Mechanics Research Communications* 38.2 (2011), pp. 106–110.
- [59] S. Grondel et al. “Fatigue crack monitoring of riveted aluminium strap joints by Lamb wave analysis and acoustic emission measurement techniques”. In: *Ndt & E International* 35.3 (2002), pp. 137–146.
- [60] I. M. Daniel et al. “Acoustic emission monitoring of fatigue damage in metals”. In: *Review of Progress in Quantitative Nondestructive Evaluation*. Springer, 1997, pp. 451–458.
- [61] J. Yu et al. “Prediction of fatigue crack growth in steel bridge components using acoustic emission”. In: *Journal of Constructional Steel Research* 67.8 (2011), pp. 1254–1260.
- [62] M. A. Hamstad. “A review: acoustic emission, a tool for composite-materials studies”. In: *Experimental Mechanics* 26.1 (1986), pp. 7–13.
- [63] P.-C. Ostiguy et al. “Selection of Structural Features for the Systematic Study of Guided Wave Propagation and Interaction with Damage”. In: *Proceedings of the 10th International Workshop on Structural Health Monitoring 2015: System Reliability for Verification and Implementation*. 2015.
- [64] V. Pagneux and A. Maurel. “Lamb wave propagation in elastic waveguides with variable thickness”. In: *Proceedings of the Royal Society A: Mathematical, Physical and Engineering Science* 462.2068 (2006), pp. 1315–1339.
- [65] Y. Cho. “Estimation of ultrasonic guided wave mode conversion in a plate with thickness variation”. In: *Ultrasonics, Ferroelectrics and Frequency Control, IEEE Transactions on* 47.3 (2000), pp. 591–603.
- [66] S. I. Rokhlin. “Lamb wave interaction with lap-shear adhesive joints: Theory and experiment”. In: *The Journal of the Acoustical Society of America* 89.6 (1991), pp. 2758–2765.
- [67] F. L. di Scalea, P. Rizzo and A. Marzani. “Propagation of ultrasonic guided waves in lap-shear adhesive joints: Case of incident a₀ Lamb wave”. In: *The Journal of the Acoustical Society of America* 115.1 (2004), pp. 146–156.
- [68] M. J. S. Lowe, R. E. Challis and C. W. Chan. “The transmission of Lamb waves across adhesively bonded lap joints”. In: *The Journal of the Acoustical Society of America* 107.3 (2000), pp. 1333–1345.

- [69] W.-J. Song et al. “Ultrasonic guided wave scattering in a plate overlap”. In: *Ultrasonics, Ferroelectrics and Frequency Control, IEEE Transactions on* 52.5 (2005), pp. 892–903.
- [70] R. P. Dalton, P. Cawley and M. J. S. Lowe. “The potential of guided waves for monitoring large areas of metallic aircraft fuselage structure”. In: *Journal of Nondestructive Evaluation* 20.1 (2001), pp. 29–46.
- [71] R. P. Dalton, P. Cawley and M. J. Lowe. “Propagation of acoustic emission signals in metallic fuselage structure”. In: *Science, Measurement and Technology, IEE Proceedings-*. Vol. 148. 4. IET. 2001, pp. 169–177.
- [72] Y. Liu et al. “Structural health monitoring and damage detection in composite panels with multiple stiffeners”. In: *Proceedings of 52nd AIAA/ASME/ASCE/AHS/ASC Structures, Structural Dynamics, and Materials Conference*. 2011.
- [73] V. Agostini et al. “Simulation of Lamb wave propagation for the characterization of complex structures”. In: *Ultrasonics, Ferroelectrics and Frequency Control, IEEE Transactions on* 50.4 (2003), pp. 441–448.
- [74] S. E. Olson et al. “Interaction of lamb waves with structural features of an aircraft fuselage”. In: *Proceedings of the 5th Edition of the European Workshop on Structural Health Monitoring*. 2010.
- [75] E. B. Flynn et al. “Enhanced detection through low-order stochastic modeling for guided-wave structural health monitoring”. In: *Structural Health Monitoring* (2011), p. 1475921711414232.
- [76] J. J. Scholey and P. D. Wilcox. *Acoustic Emission for the Localization of Damaged Regions in Structures as Part of the NDE Process*. Tech. rep. RCNDE Targeted Research Project, 2007.
- [77] J. E. Michaels et al. “Chirp excitation of ultrasonic guided waves”. In: *Ultrasonics* 53.1 (2013), pp. 265–270.
- [78] C. A. Paget and M. A. Rehman. “Multimodal location algorithm for Lamb waves propagating through anisotropic materials”. In: *SPIE Smart Structures and Materials+ Nondestructive Evaluation and Health Monitoring*. International Society for Optics and Photonics. 2017, pp. 1016806–1016806.
- [79] B. Hartmann et al. “Hierarchical local model trees for design of experiments in the framework of ultrasonic structural health monitoring”. In: *2011 IEEE International Conference on Control Applications (CCA)*. IEEE. 2011, pp. 1163–1170.
- [80] O. Nelles. *Nonlinear System Identification: From Classical Approaches to Neural Networks and Fuzzy Models*. Springer, 2001.

- [81] O. Nelles. “Axes-oblique partitioning strategies for local model networks”. In: *2006 IEEE Conference on Computer Aided Control System Design, 2006 IEEE International Conference on Control Applications, 2006 IEEE International Symposium on Intelligent Control*. IEEE. 2006, pp. 2378–2383.
- [82] S. Ernst. “Hinging hyperplane trees for approximation and identification”. In: *Decision and Control, 1998. Proceedings of the 37th IEEE Conference on*. Vol. 2. IEEE. 1998, pp. 1266–1271.
- [83] V. A. Attarian, F. B. Cegla and P. Cawley. “Long-term stability of guided wave structural health monitoring using distributed adhesively bonded piezoelectric transducers”. In: *Structural Health Monitoring* 13.3 (2014), pp. 265–280.
- [84] Y. Lu and J. E. Michaels. “A methodology for structural health monitoring with diffuse ultrasonic waves in the presence of temperature variations”. In: *Ultrasonics* 43.9 (2005), pp. 717–731.
- [85] J. E. Michaels. “Sparse array imaging with guided waves under variable environmental conditions”. In: *Structural health monitoring (SHM) in aerospace structures* (2016), pp. 255–284.
- [86] T. Clarke, F. Simonetti and P. Cawley. “Guided wave health monitoring of complex structures by sparse array systems: Influence of temperature changes on performance”. In: *Journal of Sound and Vibration* 329.12 (2010), pp. 2306–2322.
- [87] O. Putkis and A. J. Croxford. “Continuous baseline growth and monitoring for guided wave SHM”. In: *Smart Materials and Structures* 22.5 (2013), p. 055029.
- [88] C. Liu et al. “Robust ultrasonic damage detection under complex environmental conditions using singular value decomposition”. In: *Ultrasonics* 58 (2015), pp. 75–86.
- [89] J. Dobson and P. Cawley. “Independent component analysis for improved defect detection in guided wave monitoring”. In: *Proceedings of the IEEE* 104.8 (2016), pp. 1620–1631.

Acronyms

2D 2 Dimensional.

3D 3 Dimensional.

ADC Analogue to Digital Converter.

AE Acoustic Emission.

BALRUE British Aerospace Lloyd's Register Ultra Electronics.

CBG Continuous Baseline Growth.

DoE Design of Experiments.

EMAT Electro-Magnetic Acoustic Transducer.

FE Finite Element.

GWSHM Guided Wave Structural Health Monitoring.

HilomotDoE *Hierarchical local model tree for Design of Experiments.*

ICA Independent Component Analysis.

LISA Local Interaction Simulation Approach.

LTI Linear Time-shift Invariant.

NDT Non-Destructive Testing.

OBS Optimum Baseline Subtraction.

OSM Optimal Stretch Method.

PLB Pencil Lead Break.

PZT Lead Zirconate Titanate.

RHS Right Hand Side.

RMS Root Mean Squared.

SHM Structural Health Monitoring.

SNR Signal to Noise Ratio.

SVD Singular Value Decomposition.